INAUGURAL-DISSERTATION

zur

Erlangung der Doktorwürde

der

Naturwissenschaftlich-Mathematischen
Gesamtfakultät

der

Ruprecht-Karls-Universität
Heidelberg

vorgelegt von
Dipl.-Phys. Béla Alexander Majorovits
aus Heidelberg

Tag der mündlichen Prüfung: 20. Dezember 2000

High Purity Germanium Detektoren für die
Suche nach seltenen Ereignissen:
Untergrundreduktion und Zukunftsaussichten mit
dem GENIUS Projekt

Dissertation
submitted to the Combined Faculties of Natural
Sciences and for Mathematics
of the Rupertus Carola University of
Heidelberg, Germany
for the degree of
Doctor of Natural Sciences

High Purity Germanium detectors for the search
of rare events: Background discrimination and
future prospects with the GENIUS project

presented by
Diplom-Physicist Béla Alexander Majorovits
born in Heidelberg

Heidelberg, 20th of December 2000

Referees: Prof. Dr. Hans Volker Klapdor-Kleingrothaus
Prof. Dr. Dirk Schwalm

Abstract

Das Thema dieser Arbeit ist die Suche nach Dunkler Materie und neutrinolosem Doppelbetazerfall mit High Purity Germanium Detektoren. In der modernen Pysik ist es zur Zeit eines der Hauptanliegen die Natur der Dunklen Materie und die Beschaffenheit von Neutrinos zu erkunden. Das Heidelberg-Moskau-Experiment liefert zur Zeit das beste Limit auf neutrinolosen Doppelbetazerfall, der weitreichende Informationen über die Natur von Neutrinos liefern kann. Eine neue Methode zur Datenanalyse, basierend auf neuronalen Netzwerken wurde im Rahmen dieser Arbeit entwickelt. Das Limit konnte im Vergleich zur bisherigen Methode verbessert werden. Das HDMS-Experiment wurde konzipiert um nach Dunkler Materie in Form von WIMPs zu suchen. Der endgültige Aufbau wurde installiert. Das erste resultierende Untergrundspektrum wird hier besprochen. Es werden mehrere Proposals für einen Test-Aufbau für das GENIUS Projekt vorgeschlagen. Ihre erreichbare Sensitivität auf WIMPs wird diskutiert. Das BARGEIN Projekt wird eingeführt und es wird gezeigt, daß dieses Experiment mit minimalem Aufwand die DAMA Evidenz für WIMPs über das WIMP-Kern Rückstoßspektrum testen könnte. Schliesslich wird vorgeschlagen, das BARGEIN Proposal zur Genius TF zu vergrössern, um an Hand dieses Projekts sowohl Signal, als auch Signatur von WIMPs in Form der jährlichen Modulation nachzuweisen. Die Vorbereitungen für den Aufbau der GENIUS TF sind bereits im Gange.

This thesis concentrates on the search for WIMP dark matter and neutrinoless double beta decay using High Purity Germanium detectors. In modern physics two of the main goals are to find out about the nature of dark matter and to answer the question on the neutrino mass. The Heidelberg–Moscow $\beta\beta$ experiment presently provides the best limits for neutrinoless double beta decay which provides important information on the nature of neutrinos. A new data analysis method based on neural networks has been developed in the course of this work. A new lower limit on the half life of neutrinoless double beta decay could be derived. The HDMS experiment is designed to look for WIMP dark matter. It has been installed in its final setup and the first spectrum obtained is discussed here. Several proposals for test setups for the GENIUS experiment are introduced and their projected sensitivities on WIMP dark matter search are discussed. The BARGEIN project is proposed and it is discussed that this experiment could with minimal effort test the DAMA evidence using the signal by means of the WIMP-nuclear recoil spectrum. It is finally proposed to use the BARGEIN proposal in an enlarged setup, the Genius TF, to prove the feasibility of the GENIUS experiment and to fully test the DAMA evidence by means of signal and signature, the annual modulation effect. The preparations for the installation of the Genius TF did already begin.

Contents

Chapter 1

Introduction

It is known since more than sixty years that our universe consists of more matter than visible with conventional telescopes [Kap22, Zwi33]. Despite the fact that this problem has been neglected in the physics community for four decades, the hunt for the solution of this dark matter problem has lately gained much attention again.

It is well established by now that up to 99% of the matter/energy in the universe is dark, if Newtonian laws are not abandoned. The composition of this dark fraction of the total density is still a mystery. However, the history and the geometry of the universe sensitively depend on the composition of these components. Therefore it is of great importance to do further research in this field.

Several recent observations seem to clarify our picture about the composition of our world. Supernova Ia observations suggest that we are living in a universe with a non-vanishing cosmological constant [Per98, Gar98], contributing with a great amount of dark energy to the overall density. This observation confirms earlier conclusions on Λ from the age of galaxies [Kla86]. The latest observations of anisotropies in the Cosmic Microwave Background (CMB) indicate an energy density of the universe (dark matter and dark energy) which is very close to the critical density [Lan00, Han00].

It is lately commonly accepted that dark matter consists of at least three components: Baryonic and non-baryonic dark matter and dark energy [Tur00].

Theoretical considerations predict independently from astronomical observations the existence of yet undetected non-baryonic particles. Among them is the Lightest Supersymmetric Particle. Its existence follows from the supersymmetric extension of the Standard Model of particle physics. If Supersymmetry (SUSY) exists (without R-parity violation), the lightest supersymmetric particle (LSP) as a neutralino would make up large parts of dark matter. The LSP as a Weakly Interacting Massive Particles (WIMP) is among the favorite particle dark matter candidates.

There is first positive evidence for the existence of WIMP dark matter from the DAMA experiment [Ber00b, Bel00]. The importance of this result can not be underestimated thus it is now of utmost interest to independently test this positive evidence. On the other hand, should this evidence not be confirmed, as suggested by latest results of the CDMS collaboration [Abu00], there must follow a large step forward in experimental sensitivity concerning WIMP dark
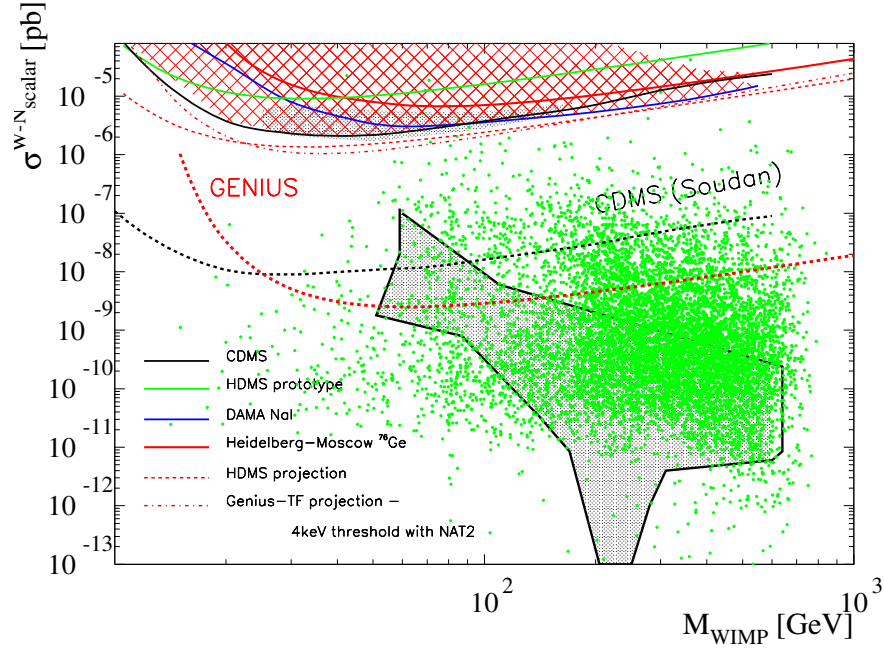
Figure 1.1: Exclusion plot of the scalar WIMP-nucleon elastic scattering cross section as a function of the WIMP mass. Plotted are excluded areas from the presently most sensitive direct detection experiments (hatched area, DAMA [Ber98], CDMS [Abu00], Heidelberg-Moscow [Hei98], HDMS prototype[Maj00c]) and some projections for experiments running or being presently under construction (HDMS [Bau00], Genius TF [Kla00d, Maj00d]). The extrapolated sensitivities of future experiments (GENIUS [Kla99a], CDMS at Soudan [Abu00]) are also shown. The scatter plot corresponds to predictions from theoretical considerations of the MSSM [Bed00b]. The small shaded area represents the 2σ evidence region from the DAMA experiment [Ber96]. The large shaded area corresponds to calculations in the mSUGRA-inspired framework of the MSSM, with universality relations for the parameters at GUT scale [Ell00] (Figure taken from [Bed00b]).

matter search. Theoretical predictions of possible WIMP candidates indicate that the cross section of these particles is by orders of magnitudes smaller than presently observable (see figure 1.1).

Also in the neutrino sector there have lately been some very exciting results confirming that neutrinos have to have a non-vanishing rest mass [Suz00, Fuk98, Sob00]. Neutrinos are still discussed as one possible component of non-baryonic dark matter, contributing by up to 12% to the overall density [Pri00, Teg00]. The question of the neutrino mass is not yet answered. Neutrino oscillation experiments which brought the confirmation of a non-vanishing neutrino mass can not provide any information on the absolute mass scale and are therefore not answering the question on how much neutrinos contribute to the energy density of the universe. Different approaches are in order to provide this answer. Neutrinoless double beta decay is presently one of the most favored mechanisms to reconstruct the neutrino mass spectrum [Kla00c]. The presently most sensitive experiment, the Heidelberg-Moscow experiment can already now make important statements on some neutrino mass models [Kla00b, Hei99]. Also in this field a large step forward in sensitivity is due.

Many experimental efforts are presently underway to complete our knowledge about the composition of the world.

Two of the very promising approaches towards the clarification are the direct search for WIMP dark matter and the search for neutrinoless double beta decay. The focus of this thesis is on these two approaches: direct WIMP dark matter detection and the search for neutrinoless double beta decay.

This work is divided into three parts:

Introduction to the topics of dark matter search and the search for neutrinoless double beta decay with High Purity Germanium (HPGe) detectors.

The experiments: Status of the Heidelberg–Moscow $\beta\beta$ experiment and the HDMS experiment running in the Gran Sasso underground laboratory and the discussion of the work which has been done for this thesis to improve the sensitivities of these experiments.

Future possibilities: Investigation of the future possibilities concerning the search for rare events with HPGe detectors including proposals which have been worked out and investigated in the course of this thesis to make a first step towards the realization of the GENIUS experiment.

A basic introduction to the dark matter problem is given in chapter 2 and to neutrinoless double beta decay and its potential concerning Beyond the Standard Model Physics in chapter 3. It is then discussed in chapter 4 how rare events like the WIMP-nuclear recoil or neutrinoless double beta decay can in principle be detected using High Purity (HPGe) Germanium detectors.

The present situation of the Heidelberg–Moscow $\beta\beta$ experiment [Kla87, Kla97, Kla00b, Kla00e, Die00] which is specially designed to search for the neutrinoless double beta decay is discussed in chapter 5.

One of the main goals of this thesis was to further increase the sensitivity of the experiment. For this reason a new data analysis has been developed. Already since 1995 a further background discrimination is being applied, making use of pulse shape recording [Hei97]. However, this analysis was based on a one parameter cut. A new method making use of neural networks was developed in the course of this work and successfully tested. The efficiency of the background recognition could be improved. This is discussed in detail in chapter 6.

Chapter 7 deals with the new data analysis code which was written in the course of this thesis in order to apply the new background rejection method efficiently. It has some advantages with respect to the old code thus further reducing the already very low background index of the Heidelberg–Moscow $\beta\beta$ experiment. The extracted limits on neutrinoless double beta decay could be improved with respect to the old method. The new approach and analysis procedure is compared to the results from the old pulse shape analysis and is discussed in detail.

For the first time all the $0\nu\beta\beta$ candidate events from the collected data of the Heidelberg–Moscow $\beta\beta$ experiment are presented. All pulse shapes of possible neutrinoless double beta decay candidates are shown and the important parameters are listed in the end of chapter 7.

Chapter 8 is devoted to the Heidelberg Dark Matter Search (HDMS) experiment. This experiment uses a special configuration of germanium detectors to effectively reject background events in the low energy region. A prototype

setup was running for 15 months in the Gran Sasso underground laboratory. The resulting energy spectrum is discussed shortly and for the first time exclusion limits on the WIMP-nucleon cross section were derived from the obtained data in this work.

The final setup of this experiment started data taking in August 2000. The changes made with respect to the prototype setup are discussed and as a result the first energy spectrum obtained from the background measurements in the Gran Sasso underground laboratory is shown and analyzed.

The last part of the thesis deals with the future development in the field of the search for rare events with High Purity Germanium (HPGe) detectors, like WIMP-nuclear recoil and neutrinoless double beta decay.

For the GENIUS project which has been proposed in 1997 [Kla98a] new results concerning possible background sources in form of cosmogenic tritium production in the detectors during production are outlined. As a result of this work it is furthermore shown that the GENIUS experiment can be setup at any underground laboratory with a shielding overburden > 2000 meter water equivalent (mwe).

In chapter 10 finally some proposals are discussed which have been worked out in the course of this thesis. These proposals could serve as a first step towards the realization of the GENIUS experiment:

The GENINO setup uses the same conceptual design as the full scale GENIUS experiment. The concept of this proposal is to decrease the size of the experiment by replacing some of the liquid nitrogen shielding strength by a lead shield. The sensitivity for such a setup was studied in detail by performing simulations of the relevant background components.

Another proposal which has been introduced and investigated in the course of this work, the BARGEIN proposal, makes use of the new detector technique of HPGe detectors operated directly in liquid nitrogen. This technique was investigated for its usefulness in connection with a conventional shield using copper or lead against external radiation. It is shown that with such an experiment the background index of the Heidelberg–Moscow $\beta\beta$ experiment could be improved. It is suggested to use two detectors which are stored in the Gran Sasso underground laboratory since 1992 for this setup: This has the advantage that most of the cosmogenically produced isotopes which are limiting the sensitivity had sufficient time to decay. Hardly any additional material would be needed thus significantly reducing cost and time needed for the installation. This setup could serve as a first check of the long term stability of the new detector technique and simultaneously provide relevant data on WIMP dark matter search.

As an extension of the BARGEIN proposal the GENIUS Test Facility (TF) has been worked out. The idea is to use the concept of the BARGEIN setup, but enlarge its size in order to house enough detector mass. In this way the claimed DAMA WIMP dark matter evidence could be directly tested through both the WIMP-nuclear recoil spectrum signal and the annual modulation signature. The future prospects for this setup which has been approved in its first stage is shortly outlined.

The GENIUS project and the Genius TF are next to the DAMA experiment the only proposed experimental approaches which will be sensitive to the WIMP-nucleus recoil signal and the annual modulation signature simulatneously awaited from the positive DAMA WIMP evidence [Bel00, Kla98d, Ram98b].

Chapter 2

The Dark Matter Problem(s)

2.1 Basics from Cosmology

For a better understanding of the Dark Matter problem, it is neccessary to have a basic knowledge of cosmology since the existence of Dark Matter does influence the history of our universe considerably. Hints for a threefold Dark Matter problem are lately getting very strong. For the discussion of the three missing components it is inevitable to know some of the theoretical background. This is not the place to give a basic introduction to cosmology. For a general description see for example [Kla99b, Ber95, Kol90]. However, some basic equations are described in the following section.

2.1.1 The Standard Model of Cosmology

The Standard Cosmological model is based on the so called cosmological principal:

- Homogeneity on the largest scales and

- Isotropy of the universe.

These two assumptions lead to the Robertson-Walker metric (see [Rob35, Wal36]) written in terms of co-moving coordinates r, θ and ϕ:

$$ds^2 = \mathrm{R}(\tau)^2 \left[\frac{\mathrm{d}r^2}{(1 - \mathrm{k}r^2)} + \mathrm{r}^2(\mathrm{d}\theta^2) + \sin\theta^2 \mathrm{d}\phi^2) \right] - \mathrm{c}^2 \mathrm{d}\tau^2, \qquad (2.1)$$

where k can have the values ± 1 or 0 and $R(\tau)$ is an arbitrary scale factor,denoting the 'size' of the universe at time τ. The distance between two observers with fixed co-moving coordinates scales with this scale factor $R(\tau)$.

From symmetries of the Robertson Walker metric and the cosmological principle it is possible to give constraints on the energy stress tensor T^μ_ν. The simplest realization for T^μ_ν is [Kol90]:

$$T^\mu_\nu = diag(\rho, -p, -p, -p), \qquad (2.2)$$

where $\rho(\tau)$ is the time dependent energy density and p(τ) the time dependent pressure for an ideal fluid. From energy conservation one gets:

$$d(\rho R^3) = -pd(R^3). \tag{2.3}$$

Taking the equation of state:

$$p = w\rho \tag{2.4}$$

(with ρ being time independent) one gets a relation between scale factor and energy density [Kol90]:

$$R^3 d\rho = -\rho(1 + w)d(R^3) \quad \rightarrow \quad \rho \propto R^{-3(1+w)}. \tag{2.5}$$

Examples in the history of the universe are:

- Radiation dominated universe: p=1/3ρ $\rightarrow \rho \propto R^{-4}$

- Matter dominated universe: p=0 $\rightarrow \rho \propto R^{-3}$

In the early stage of its history the universe was radiation dominated, in its late stage (as now, e.g.) it was matter dominated. In case of a non-vanishing cosmological constant the universe might become dominated by Λ.

The dynamical equations for the description of the time evolution of the scale factor R(τ) follow from Einstein's field equations [Kol90]:

$$R_{\mu\nu} - \frac{1}{2}g_{\mu\nu}\mathcal{R} = 8\pi G T_{\mu\nu} - g_{\mu\nu}\Lambda, \tag{2.6}$$

with $R_{\mu\nu}$ the Ricci Tensor, $\mathcal{R} = R_{\mu\nu}g^{\mu\nu}$ the Ricci scalar , $T_{\mu\nu}$ the energy stress tensor and Λ the so called cosmological constant.

The 0-0 component of these equations is called Friedmann-equation:

$$\frac{\dot{R}^2}{R^2} + \frac{k}{R^2} = \frac{8\pi G}{3}\rho, \tag{2.7}$$

where $\rho = \rho_m + \rho_\Lambda = \rho_m + \frac{\Lambda}{8\pi G}$. Once the Hubble parameter is defined as $H = \dot{R}/R$, the Friedmann equation can be written as

$$\frac{k}{H^2 R^2} = \frac{\rho}{(3H^2)/(8\pi G)} + \frac{\Lambda}{3H^2} - 1 = \Omega - 1, \tag{2.8}$$

where Ω is the ratio of the density to the critical density ρ_c of the universe:

$$\rho_c = \frac{3H^2}{8\pi G} = 1.879 \times 10^{-29}\text{h}^2\text{gcm}^{-3}, \quad \Omega = \Omega_m + \Omega_\Lambda = \frac{\rho}{\rho_c}. \tag{2.9}$$

This gives a relation between curvature k of the metric and the density parameter Ω; thus knowing Ω, the geometry of the universe is known:

$\Omega > 1$: k = 1, closed universe

$\Omega = 1$: k = 0, flat universe

$\Omega < 1$: k = -1, closed universe

Note however that in case of a non-vanishing cosmological constant the term closed universe refers only to the geometry, not to the history of the universe since in that case the universe would expand forever. It should also be stated, that this would mean a negative pressure in the equation of state (2.4) ($w < 0$).

The present favored values for the cosmological parameters are [Pri00]:

- The Hubble constant: $H_0 = (65\pm8)$ km/(s Mpc),

- age of the universe: $t_0 = 13$ Gyr,

- total energy density of the universe: $\Omega = 1.1 \pm 0.3$,

- mass density: $\Omega_m = 0.4 \pm 0.2$,

- baryonic mass density $\Omega_B h^2 = 0.019 \pm 0.002$,

- contribution of cosmological constant to energy density: $\Omega_\Lambda \sim 0.7$.

2.2 Astronomical and Cosmological evidence for Dark Matter

It was always one of the main goals in observing astronomy to find out about the total energy density of the universe. As discussed above, this parameter substantially influences the evolution and the geometry of the universe. The problem of Dark Matter is still one of the biggest remaining mysteries in modern physics. It was in the year 1922 that Kapteyn for the first time suggested (due to kinematic reasons) that there is more matter in our galaxy than we see [Kap22]. In 1933 Fritz Zwicky observed that the dispersion velocities of galaxies are too high to be gravitationally bound to the galaxy cluster if there is no additional matter ensuring a large enough gravitational potential and first suggested Dark Matter to explain the mass deficit [Zwi33]. For forty years the Dark Matter problem had been forgotten, when finally Freeman found that the rotational curves of the galaxies he studied (M33, NGC300) did not follow the expected shape inferred from the visible mass [Fre70].

Following Kepler's law one expects from the visible matter outside the bulge of the galaxy a decrease of the rotation velocity v_{rot} around the galactic center with increasing distance $v_{rot} \propto 1/\sqrt{r}$.

The observations suggest that the rotation curves remain flat as far out as they can be observed. If one does not abandon Newtonian laws, it is neccessary to assume an extended massive halo around the galaxies in order to explain the shape of the rotation curves. Further investigation of more than 1000 spiral galaxies by Salucci and Persic have well established this general behavior leading to the universal rotation curve [Per95].

However, the Dark Matter problem stretches over all observable length scales, starting from spheroidical dwarf galaxies all the way to large scale structure and structure formation as well as the Cosmic Microwave Background (CMB). The fraction of Dark Matter seems to become bigger for larger structures:

Dwarf galaxies : The dispersion velocities of the components of these galaxies suggest that the virial theorem can only be fulfilled (similar to Zwicky's

observation of galaxy clusters), if the gravitational potential is considerably larger as calculated from the visible stars [Bur97].

Rotation curves of spiral galaxies: The rotation curves of spiral galaxies have a flat shape out to their observable edges (see above, [Fre70]). A massive extended halo around the galactic bulge and disk containing dark matter has to be assumed in order to explain this phenomenon.

Elliptical galaxies : Similar to the spheroidical dwarf galaxies in elliptical galaxies the dispersion velocities of the components are too high to be bound to the gravitational potential of the observable stars. More mass than observed to obtain a gravitational potential strong enough to bind the components together. [Loe99]

Velocities in galaxy clusters : Also in clusters of galaxies the measured dispersion velocities are too high in order to explain gravitational binding of its components (see above and [Zwi33, Bor97]). The overall mass of the galaxy clusters has to be many times the observed to obtain a sufficient gravitational potential [Bor97].

X-rays from inter-galactic gas in galaxy clusters: From the observed X-rays of galaxy clusters it is possible to derive the temperature of the inter-galactic gas. However, the deduced temperatures are too high as for the inter-galactic gas to be gravitationally bound to the visible mass only [Böh97]. In order for this gas not to escape the cluster, additional mass is neccessary.

Gravitational lensing : Through the gravitational lensing of distant galaxies behind clusters, it is possible to infer the mass of the cluster (see for example [Tys95]). Consistently to other methods of obtaining the dark matter ratio of clusters, a mass of many times more than observed is deduced [Kai00].

Structure formation : If the largest observable scales in the universe are compared to predictions from simulations, it becomes evident that the observable mass is not sufficient to form structures on large scales as observed. Additional mass of up to a factor of 100 more than visible is needed to explain structure formation[Hu98, Jen98].

Evidence for Dark Matter from astronomical observations alone is already overwhelming. However, from cosmological considerations there is further evidence for Dark Matter.

Big Bang Nucleosynthesis (BBN)

Following the standard hot big bang cosmology, the universe must have been extremely hot and dense in its first moments. At these temperatures and densities fusion of Hydrogen to Deuterium and to Lithium could take place. It is easy to calculate the abundance of the produced elements as a function of the baryonic mass density Ω_B (see e.g. [Kol90]). If the measured abundances of Deuterium from very old Hydrogen clouds or from the Ly-α forest [Bur00] are compared to the calculated ones, a value of $\Omega_B \sim 0.05$ results in a very good

agreement. Also for all other produced isotopes this value for Ω_B can reproduce the measured abundances within the one sigma confidence interval.

However, this result introduces a twofold Dark Matter problem: The amount of visible baryonic mass only contributes with $\Omega_{vis} \sim 0.005$, being approximately one order of magnitude less than demanded from Big Bang Nucleosynthesis. On the other hand, from kinematic, as well as from CMB observations an overall mass density of $\Omega_m \sim 0.4$ is observed. Thus we know that a great part of the baryonic mass is dark, however baryonic dark matter can not be responsible alone for the dark matter problem, there has to be an additional non-baryonic component of the missing mass.

The Cosmic Microwave Background and Inflation

A further problem appears, if the most recent observations of the CMB power spectrum are considered.

In the beginning our universe was radiation dominated (see above). After approximately 100.000 years the cosmos was cold and the energy density low enough for electrons and protons to build Hydrogen atoms without being immediately reionized again. The universe became transparent for light. The photons which have since not scattered make up the Cosmic Microwave Background (CMB) as the relict of the early universe, thus giving us a 'snapshot' of the universe at that time. The existence of the CMB was predicted already in the year 1948 by R. Alpher, R. Herman and G. Gamow and for the first time observed by Penzias and Wilson in 1965 [Pen65].

The inflationary theory is an attempt to solve the horizon problem. It states that in a time span of $\sim 10^{-32}$ seconds the universe must have expanded by a factor of $\sim 10^{43}$ [Kol90] thus driving formerly causually connected regions so far apart, that after inflation had occured, these regions were out of causual contact. This allows to explain, why the CMB is perfectly isotropic on the whole horizon, although opposite regions could not have been in causual contact at the time of re combination (horizon problem), assuming a cosmological model without inflation. In addition Inflation makes the prediction of a universe with critical density: $\Omega_0 = 1$.

A further statement of inflation is that quantum fluctuations should have been blown up during this epoch, thus planting the first seeds for large scale structure. The evolution of the first structures, regardless of their history, from the end of the inflationary epoch until recombination (the time when the universe became transparent for light) strongly depends on the value of the energy density Ω_0.

Thus the anisotropy in the CMB can give a direct measurement of the total energy density of the universe.

Recent measurements of these anisotropies of the Boomerang and MAXIMA experiments [Lan00, Han00] suggest that the overall energy density is very close to unity.

Thus a third Dark Matter problem is introduced: there is a discrepancy between the kinematically demanded matter density $\Omega_m \sim 0.4$ and the total energy density needed to explain the CMB power spectrum $\Omega_0 \sim 1.0$.

This difference could be explained by a non-vanishing cosmological constant Λ, making up to the so called Dark Energy constituent.

Dark Energy and SN Ia observations

The existence of a homogeneously distributed Dark Energy component should be observable in the history of the universe. Since Dark Energy leads to a negative component in the equation of state ($w < 0$ in equation (2.4)), a non-vanishing Λ term leads to an accelerated expansion of the universe.

Recent high-z SNIa observations suggest that there is indeed such an acceleration of our universe [Per98, Gar98], thus a non-vanishing cosmological constant Λ is inferred.

Already earlier there has been some evidence on the existence of this Λ term from considerations of the age of the universe [Kla86].

2.3   Candidates for Dark Matter

Most of the efforts to solve the problem of the missing mass assume that it is an invisible matter component leading to the phenomenon described earlier.

However, there is suggestions which try to explain the Dark Matter problem without having to assume invisible mass components.

MOND (MOdified Newton Dynamics), for instance, can explain the rotation curves of spiral galaxies, by modification of Newtonian laws [Mil98]. The ansatz of this theory is to introduce an additional acceleration term a_0 which is only observable in the limit of a vanishing gravitational acceleration. Although MOND can not explain all the Dark Matter evidences, this possibility could not yet be excluded. Nevertheless in the following it will be assumed that the Dark Matter problem requires some kind of invisible mass.

The candidates for Dark Matter can be divided into two categories: baryonic and non-baryonic. As already stated above, it seems probable that both categories will have to contribute to the solution.

Baryonic Dark Matter

The most important candidate for baryonic Dark Matter are MACHOs (Massive Astrophysical Compact Halo Objects) [Pac86, Tur93]. Those objects could be Jupiter like objects [Haw00], brown or beige dwarfs [Car00], white dwarfs, primordial black holes [Jed00] or clouds of non-baryonic dark matter [Zak00].

Since the brightness of these objects is too low as for them to be detected with conventional telescopes, their detection has to happen through an alternative approach: gravitational lensing.

If the line of sight of a background star passes a massive object, light rays will be bent by the gravitational influence of the dark mass, resulting in two images of the same star. If the alignment is perfect, the result is an Einstein ring. Typically, for imperfect alignment, the star appears as two arches. For events in our own galaxy the typical angular separation is $\sim 10^{-3}$ arcsec, way too small to be resolved even with the Hubble Space telescope. Nevertheless, the event can be detected since the multiple image of the the background star results in an increased flux.

The idea of searching for MACHOs in the galactic halo through gravitational microlensing arose in 1986. Paczinsky suggested that observing the Large Magellanic Cloud (LMC) could lead to detection of these objects [Pac86]. The LMC is an ideal object for the search of MACHOs since its distance of 50 kpc - 60 kpc

is big enough to provide a good path length through the presumably dark halo. Furthermore the LMC provides enough background stars which is a very important prerequisite since the optical depth for microlensing is rather small (about one in a million stars could be microlensed per year).

Observations of the MACHO [Leh00] and EROS [Las00] collaborations seem to indicate that $\sim$20% of the missing galactic mass could be provided by MA-CHOs with a typical mass of 0.5 M$_\odot$ [Alc98].

However, many uncertainties enter the calculations, for example galaxy modeling, including uncertainties about our own halo.

In addition lately there has been strong arguments against the most probable MACHO candidate, white dwarfs [Gra00].

Further candidates for baryonic dark matter are e.g. neutral hydrogen clouds [Pfe97] or massive quark objects [Fre98]. These candidates will not be discussed here.

Non-Baryonic Dark Matter

The group of non-baryonic dark matter can be divided into two subclasses: hot and cold dark matter (HDM and CDM).

Hot dark matter contains those candidates which had relativistic speed at time of their decoupling from thermodynamic equilibrium. Cold dark matter was already thermalized at its decoupling.

The distinction between hot and cold dark matter is especially important for structure formation. If the dark matter particles were slow, the first structures to be formed were on small scales leading galaxy formation. These later built clusters and superclusters (bottom-up scenario). Fast particles would first build large structures which later would be divided into substructures (top-down scenario). Large scale structure simulations and the observation of very old galaxies clearly seem to favor a bottom up scenario [Tur00]. These results seem to indicate that cold dark matter is neccessary to explain large scale structure, however, a significant part of hot dark matter could still be present.

The most prominent candidate for hot dark matter is the neutrino. Especially since the results from the Super Kamiokande experiment in Japan [Fuk98] this candidate has gained new actuality as a dark matter component. However, massive neutrinos will not suffice to make up all of the missing non-baryonic mass.

Most of the non-baryonic dark matter candidates are elementary particles which could not yet be detected due to their very low scattering cross sections. The favored candidates for CDM are Axions and Weakly Interacting Massive Particles (WIMPs).

Both these particles are predicted from particle physics, independently from the dark matter problem.

Axions are discussed as the possible solution to the strong CP-problem of QCD. Calculations from Quantum Field Theory predict that the strong interaction should in principle break CP-symmetry. However, this CP violation is not observed. To solve the problem, a further symmetry, the Peccei-Quinn symmetry is introduced [Pec89] which is broken, thus demanding the existence of a massive particle, the axion. The main constraints for the mass of this particle result from astrophysical considerations. The possible mass of the axion ranges around 10^{-5}eV. For a review on this topic see [Pec89].

The detection of axions could happen through resonant conversion into two photons in a strong magnetic field [Sik97]. Present axion search experiments are getting in the sensitivity range for masses which are not excluded from astrophysical constraints.

2.3.1 The Neutralino as a WIMP candidate

This thesis deals partly with the possibility to detect WIMPs through the technique of direct detection. Therefore in the following there will be an overview of the most important basic theoretical considerations of the WIMP as a neutralino.

If the possibility is considered that another yet undetected stable particle exists (it will be denoted with χ in the following), it can substantially contribute to the present mass budget.

In the early universe, at temperatures higher than $M_\chi c^2$ the χ abundance was in equilibrium, given by annihilation and production of the particle $\chi\bar{\chi} \rightarrow l\bar{l}$ and $l\bar{l} \rightarrow \chi\bar{\chi}$ ($l\bar{l}$ are quark antiquark or lepton atnilepton pairs). When the temperature of the universe dropped below the critical temperature $T_{crit} = \frac{1}{k} \times M_\chi c^2$, only the annihilation process $\chi\bar{\chi} \rightarrow l\bar{l}$ could still take place. The abundance of the particle decreased exponentially, until the expansion of the universe stopped this process. The particle decoupled from thermodynamic equilibrium and its abundance is since stable [Jun96].

It is possible to estimate the contribution to the total mass density of such a partial [Jun96]:

$$\Omega_\chi h^2 = \frac{3 \cdot 10^{-27} cm^3 s^{-1}}{<\sigma_A v>},\tag{2.10}$$

where h is the Hubble constant in units of 100 km s^{-1}Mpc^{-1} and $\langle\sigma_A v\rangle >$ the annihilation cross section. It should be noted that the result does not depend on the mass M$_\chi$ of the particle , except for logarithmic corrections.

If a particle has a cross section in the order of the weak interaction, the annihilation cross section can be estimated:

$$<\sigma_A v> \sim \alpha^2 (100 \text{ GeV})^{-2} \sim 10^{-25} cm^3 s^{-1}.\tag{2.11}$$

Here α is approximately 1/100. If this value is plugged into equation (2.10), the resulting density $\Omega_\chi h^2$ becomes exactly of the order of the amount of missing dark matter.

This means that if another stable, weakly interacting particle exists, this is the missing candidate which can at least partly solve the Dark Matter problem.

The nature of χ is so far undetermined, all properties so far stated are general for all particles with weak interaction cross sections.

The best motivated candidate for such a particle is the neutralino as the Lightest Supersymmetric Particle (LSP). Within Supersymmetric (SUSY) models there is more possibilities for such an LSP, the most common being a superposition of the supersymmetric partners of the photon γ and the Z boson and of two neutral Higgs bosons:

$$\chi = N_{10}^* \tilde{\gamma} + N_{20}^* \tilde{Z} + N_{30}^* \tilde{H}_1^0 + N_{40}^* \tilde{H}_2^0 \tag{2.12}$$

WIMP parameter predictions from the MSSM

WIMPs are generally predicted from Supersymmetric models. If the lightest supersymmetric particle is a neutralino (no electrical charge), it would make an ideal candidate for the solution of the dark matter problem. Typical expected Neutralino masses lie in the mass range from 10 GeV to some TeV and their scattering cross sections are on the order of 10^{-12} - 10^{-6}pb.

Once the sensitivity of an experiment is known, it is of interest to study theoretical predictions for WIMP parameters, especially mass and cross section, in order to evaluate the discovery potential of the experiment. In the case of direct detection experiments, the extracted information from the spectrum is constraints on the M_{WIMP}-σ_0 parameter space.

Theoretical predictions for possible neutralino parameters follow from the supergravity (SUGRA) inspired Minimal Supersymmetric Standard Model (MSSM). In general SUSY models contain many free parameters (more than 60). The assumption of unification of all parameters at the GUT scale reduces the amount of free parameters to four plus one sign. This parameter space is then scanned with the help of a Monte Carlo code: a scenario is chosen randomly and it is then checked, whether this parameter combination fulfills all the experimental constraints and assumptions made by the author. If this is the case, the needed parameters are calculated, here the mass of the neutralino and its scattering cross section. For a detailed description of this method see e.g. [Bed94, Bed97, Arn00b, Eds00]

There also exists an analytical approach to deduce allowed scenarios. These are discussed in [Nat94, Nat97, Nat98].

Chapter 3

The Double Beta Decay

Double Beta decay is the rarest process observed in nature. Typical half lifes of isotopes decaying through Double beta decay are on the order of 10^{20} years. Thus, the probability for a Double Beta emitter which was produced in the early stages of our universe, to have decayed until today through double beta decay is about 10^{-10}. This comparison makes clear how rare this process is. To observe it extreme circumstances are neccessary.

One of the decay modes which is discussed in the following, the neutrinoless double beta decay, can provide important information on Beyond Standard Model Physics. If it is observed, this would confirm that neutrinos are massive. Important constraints on the neutrino mass spectrum can already be made now through the non-observation of this decay mode.

Neutrinoless double beta decay is furthermore the only known mechanism which can distinguish between Majorana (particle is equal to its anti-particle) and Dirac neutrinos (particle and anti-particle are different).

3.1   Introduction to $\beta\beta$ decay

It was Maria Goeppert-Mayer, who discussed the Double Beta decay for the first time in 1925 [Goe35]. Through emission of two electrons and two electron anti-neutrinos, a nucleus A(Z,N) decays into the energetically more favorable state A(Z+2,N-2). During the decay two neutrons are transformed into two protons. In principle the $\beta^+\beta^+$ decay is also allowed for some nuclei, but it is so rare and difficult to observe that we will only focus on the 'standard' $\beta^-\beta^-$ decay here.

This process is only observable, if the normal beta decay is energetically forbidden or suppressed due to large angular momentum differences between initial and final states (like for ^{48}Ca).

From the discussion of Weizsäckers semi empirical mass formula [Wei35] it becomes clear that the energetic conditions for the possibility of the $\beta\beta$-decay are only given, if the nucleus is of even-even type (even number of neutrons and even number of protons). For a more detailed discussion see [Kla95]. All in all there exist 36 potential Double Beta emitters
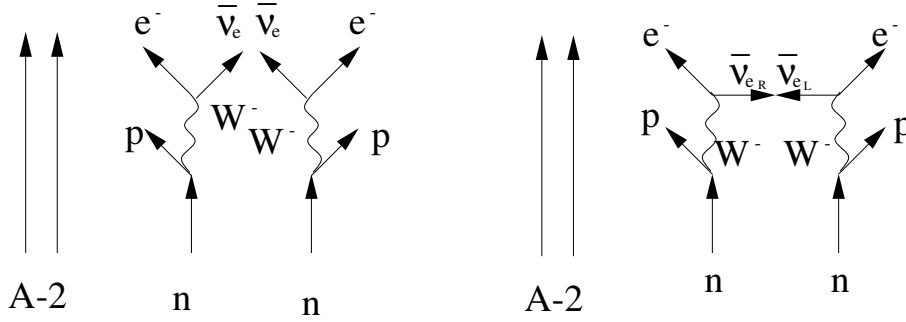
Figure 3.1: Feynman graphs of $2\nu\beta\beta$ and $0\nu\beta\beta$ decays.

3.2 Decay modes of the $\beta\beta$ decay

The $\beta\beta$ decay has several possible decay modes:

$2\nu\beta\beta$ **decay :**

$$A(Z,N) \rightarrow A(Z+2, N-2) + 2e^- + 2\bar{\nu}_e \qquad (3.1)$$

$0\nu\beta\beta$**-Zerfall :**

$$A(Z,N) \rightarrow A(Z+2, N-2) + 2e^- \qquad (3.2)$$

$0\nu\chi\beta\beta$ **decay :**

$$A(Z,N) \rightarrow A(Z+2, N-2) + 2e^- + \chi \qquad (3.3)$$

$0\nu\chi\chi\beta\beta$ **decay :**

$$A(Z,N) \rightarrow A(Z+2, N-2) + 2e^- + 2\chi \qquad (3.4)$$

The last two decay modes contain the mission of Majoron particles χ. In the following the $2\nu\beta\beta$ and the $0\nu\beta\beta$ will be shortly discussed. For a discussion of Majoron accompanied decay channels see f.g. [Chi80, Bur94, Hir96].

3.2.1 The neutrino accompanied $\beta\beta$ decay $(2\nu\beta\beta)$

In the neutrino accompanied double beta decay two neutrons decay into two protons and two electrons under the emission of two electron anti-neutrinos (see figure 3.1). This process is allowed in the Standard Model of particle physics since all conservation laws are fulfilled.

The half life of an isotope decaying through this channel can be calculated applying two subsequent Gamow-Teller transitions [Wu91]:

$$T_{1/2} = \left(F^{2\nu} \cdot \left| M_{GT}^{2\nu} \right|^2 \right)^{-1} \qquad (3.5)$$

$M_{GT}^{2\nu}$ = Gamow - Teller Matrix element
$F^{2\nu}$ = Phase space integral .

The observed spectrum of this decay is continuous since it is a many-body decay, with the two neutrinos leaving the detector. The endpoint of the spectrum lies at the Q-value of the decay. In table 3.1 the measured half lifes of some

of the double-beta candidates are listed together with the predicted half lifes
from theoretical calculations (using the Quasi particel Random Phase Approxi-
mation QRPA [Sta90]). In all cases listed in table 3.1 the predicted value for the
half life does not differ substantially from the measured one. This gives support
to the used method, thus legitimating the use of QRPA for the calculation of
matrix elements involved in the $0\nu\beta\beta$ decay.

Isotope	$T_{1/2}^{2\nu\beta\beta}$ (QRPA) [y]	$T_{1/2}^{2\nu}$ (Experiment) [y]	Reference
^{76}Ge	$2.99 \cdot 10^{21}$	$(1.77 \pm 0.01\,(stat)^{+0.13}_{-0.11}(syst)) \cdot 10^{21}$	[Gue97]
^{82}Se	$1.09 \cdot 10^{20}$	$(0.83 \pm 0.10(stat) \pm 0.07(syst)) \cdot 10^{20}$	[Arn98]
^{96}Zr	$1.08 \cdot 10^{19}$	$(3.9 \pm 0.9) \cdot 10^{19}$	[Kaw93]
^{100}Mo	$1.13 \cdot 10^{18}$	$(1.15^{+0.3}_{0.2}) \cdot 10^{19}$	[Eji96]
^{116}Cd	$6.31 \cdot 10^{19}$	$(2.6^{+0.9}_{0.5}) \cdot 10^{19}$	[Eji95]
^{128}Te	$2.63 \cdot 10^{24}$	$(7.7 \pm 0.4) \cdot 10^{24}$	[Ber93]
^{130}Te	$1.84 \cdot 10^{21}$	$(2.7 \pm 0.1) \cdot 10^{21}$	[Ber93]
^{150}Nd	$7.37 \cdot 10^{18}$	$(1.88^{+0.69}_{0.39} \pm 0.19) \cdot 10^{19}$	[Art95]

Table 3.1: Measured values of $2\nu\beta\beta$ decay for some of the double beta candidates (taken
from [Die99]). Also shown are theoretical predictions for the half lifes using QRPA [Sta90].

3.2.2   The neutrinoless double beta decay $(0\nu\beta\beta)$

Much more interesting than the neutrino accompanied double beta decay is the
neutrinoless double beta decay since it is forbidden in the Standard Model of
particle physics. Thus if this decay could be observed, this would be a clear sign
of physics beyond the Standard Model. This decay mode violates lepton number
conservation by two units, $\Delta L = 2$. The emitted anti-neutrinos are absorbed
immediately through the second emitted neutrino (see figure 3.1) which implies
that once this process is observed, the neutrino has to be of Majorana type.
Since also the helicity of the neutrino has to change during this process, it also
implies that neutrinos would have to be massive. Thus the neutrinoless double
beta decay can only occur if:

- neutrinos are Majorana particles and

- the neutrino is a massive particle since a helicity flip has to occur during
  the decay process.

Neutrinoless double beta decay is presently the only known way to distin-
guish between Dirac- and Majorana neutrinos. In principle there is a rare Kaon-
decay

$$K^+ \rightarrow \pi^+ \nu\bar{\nu} = \sum_m (K^+ \rightarrow \pi\nu_m\bar{\nu}_m) \tag{3.6}$$

which allows to distinguish between Dirac- and Majorana neutrinos using the
form of its energy spectrum. However, this decay is so rare that it could not
even be detected yet [Kay89, Bur99].

Isotope	$T_{1/2}^{0\nu}$ [yr]	C.L. [%]	$\langle m_\nu \rangle$ [eV]	
^{48}Ca	$\geq 9.5 \times 10^{21}$	76 [Ke91]	≤ 13	[Sta90]
^{76}Ge	$\geq 1.9 \times 10^{25}$	90 [Die00]	≤ 0.35	[Sta90], 0.98 [Cau96], 0.91 [Eng88],
				0.33 [Tom91], 0.7 eV [Sim97]
^{82}Se	$\geq 9.5 \times 10^{21}$	90 [Arn98]	≤ 7.9	[Sta90], 15.7 [Cau96], 24 [Eng88], 8 [Tom91]
	$\geq 2.7 \times 10^{22}$	68 [Ell92]	≤ 4.7	[Sta90], 9.4 [Cau96], 14.4 [Eng88], 4.75 [Tom91]
^{100}Mo	$\geq 5.2 \times 10^{22}$	68 [Kud98]	≤ 4.9	[Sta90], 4.34 [Eng88], 2.2 [Tom91], 2.2 [Sim97]
^{116}Cd	$\geq 3.2 \times 10^{22}$	90 [Dan99]	≤ 3.9	[Sta90]
^{130}Te	$\geq 5.6 \times 10^{22}$	90 [All98]	≤ 2.9	[Sta90], 3.43 [Eng88], 3.1 [Tom91], 2.88 [Sim97]
^{136}Xe	$\geq 4.4 \times 10^{23}$	90 [Lue98]	≤ 2.2	[Sta90], 5.2 [Cau96], 2.7 [Eng88], 1.8 [Tom91]
^{150}Nd	$\geq 1.22 \times 10^{21}$	90 [DeS97]	≤ 5.2	[Sta90]

Table 3.2: Limits on the half-lifes of the $0\nu\beta\beta$ decay and on the effective Majorana neutrino mass for different matrix element calculations for the best existing experiments with half-life limits $> 10^{21}$ yr (taken rom [Hei99]).

The half life of $0\nu\beta\beta$ decay can be calculated through the following relation[1] [Mut89]:

$$T_{1/2} = \left[F^{0\nu} \cdot \left(M_{GT}^{0\nu} - M_F^{0\nu} \right)^2 \left(\frac{\langle m_\nu \rangle}{m_e} \right) \right]^{-1}. \tag{3.7}$$

Here $F^{0\nu}$ is the Phase space integral, $M_{0\nu_{GT}}$ and $M_{0\nu_F}$ are Gamow-Teller- and Fermi- matrix elements, respectively, $\langle m_\nu \rangle$ is the effective Majorana neutrino mass and m_e the mass of electron.

The observable of $0\nu\beta\beta$, the effective Majorana neutrino mass is given by:

$$\langle m_\nu \rangle = \left| \sum_j |U_{ej}|^2 e^{i\phi_j} m_j \right| \tag{3.8}$$

where the U_{ej} are the entries of the mixing matrix known from neutrino oscillation and $e^{i\phi_j}$ are complex phases, allowing for cancelation in the effective Majorana neutrino mass.

Thus, if the half life of $0\nu\beta\beta$- decay is known, the effective Majorana neutrino mass can be derived.

In the $0\nu\beta\beta$ decay only two electrons are emitted. If both can be observed with their full energy inside one detector, the signature of this decay is a sharp peak at the summed energy of the two electrons corresponding to the Q-value of the process for the $0\nu\beta\beta$ decay (See figure 3.2).

In table 3.2 the current limits on $0\nu\beta\beta$ for some of the candidates are given.

3.3 The physics potential of $0\nu\beta\beta$ decay experiments

If neutrinoless Double Beta decay will be observed, this will have important implications for physics. It can provide information on many different fields of research, including:

---

[1] Neglecting a possible right-handed component of a weak leptonic current .
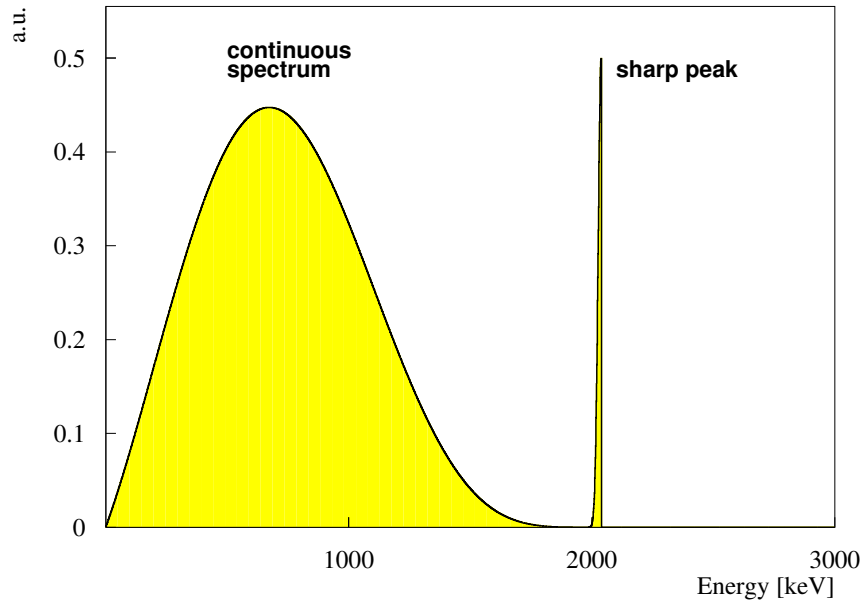
Figure 3.2: Expected signature of neutrino accompanied double beta decay (continuous spectrum) and neutrinoless double beta decay (sharp peak at Q-value).

Neutrino mass: Through the $0\nu\beta\beta$ observable, the absolute mass scale of neutrinos could be pinned down (see below, [Kla00c]).

Supersymmetry (SUSY): In SUSY it is possible to add R-parity violating terms to the superpotential which violate lepton number, or baryon number conservation. $0\nu\beta\beta$ decay can occur through these mechanisms. Thus, non-observation of $0\nu\beta\beta$ decay provides stringent limits on the R-parity violating terms in the superpotential [Hir95, Päs99b].

Compositeness: If quarks and leptons have substructure, $0\nu\beta\beta$ decay could occur through exchange of a composite heavy Majorana Neutrino. From non-observation of $0\nu\beta\beta$ decay stringent mass bounds for such an excited neutrino can be deduced [Pan99].

Special Relativity and Equivalence Principle: If the equivalence principle is violated different species of matter can have different characteristic maximum attainable speeds. It has been shown that $0\nu\beta\beta$ decay can constrain the amount of violation of equivalence principle [Kla99c].

A detailed discussion of the new physics potential of neutrinoless Double Beta decay in general and of the GENIUS project is given in [Kla99a].

In the following there will be a short summary of neutrinoless Double Beta decay in connection with neutrino oscillation experiments with respect to discrimination of neutrino mass scenarios (following [Kla00c, Päs99a]).

3.3.1 $0\nu\beta\beta$ decay and neutrino oscillations

The observable of $0\nu\beta\beta$ decay, the effective Majorana neutrino mass (see equation equation (3.8)) contains a sum over the different mass eigenstates ν_1, ν_2, ν_3. If the flavor eigenstates ν_e, ν_μ, ν_τ differ from the mass eigenstates, the electron neutrino is a mixture of the different mass eigenstates:

$$\nu_e = \sum_i U_{ei}\nu_{ei}, \qquad i = 1, 2, 3, ... \tag{3.9}$$

where U_{ei} are the entries of the mixing matrix. The mixing matrix transforms flavor- into mass eigenstates, being responsible for neutrino oscillation.

Thus, if a neutrino of the flavor ν_α with Energy E travels a distance L, the probability that it transforms into a neutrino of flavor ν_β is:

$$P(\nu_\alpha \to \nu_\beta) = sin^2(2\theta)sin^2(\Delta m^2 L/2E) \tag{3.10}$$

where $\Delta m^2 = |m_i|^2 - |m_j|^2$ is the mass square difference of the two mass eigenstates and $sin^2(2\theta)$ is the mixing angle between the two neutrino species.

Lately there has been strong observational evidence for neutrino oscillation through various experiments like Super Kamiokande [Fuk98], and the solar neutrino experiments (GALLEX [Ham99],GNO [GNO00], SAGE [Abd00], Homestake [Cle98]). All these experiments report a lack of observed neutrinos, indicating that something is happening on the way of the neutrinos from the source to the detector. The usual interpretation of these results is in terms of neutrino oscillations. If neutrino oscillations are observed, it is possible to extract the observables of neutrino oscillations Δm^2 and $sin^2(2\theta)$. However since it depends only on the mass square difference (see equation (3.10)) of the two neutrino mass eigenstates, no information on the absolute mass scale of neutrinos is gained and therefore the neutrino mass scheme can not be reconstructed.

In a recent work [Kla00c, Päs99a] the connection between the $0\nu\beta\beta$ observable and the neutrino oscillation parameters has been studied in detail. It is evident that the mass scheme realized in nature can only be reconstructed using the complementary information from both, $0\nu\beta\beta$ decay and neutrino oscillation.

Predictions on the effective Majorana neutrino mass depend strongly on the solution of the solar neutrino problem since it determines the distribution of ν_e-flavor in the mass eigenstates. This considerably affects the $0\nu\beta\beta$ observable. So far there are still several allowed solutions for the solar neutrino problem[2] (see f.g. [Gon99]):

Small Mixing angle MSW solution :

$$\Delta m_\odot^2 = (0.4 \div 1) \cdot 10^{-5} eV^2 , \quad sin^2 2\theta_\odot = (0.2 \div 1.2) \cdot 10^{-2} \tag{3.11}$$

Large Mixing angle MSW solution :

$$\Delta m_\odot^2 = (0.1 \div 1.5) \cdot 10^{-4} eV^2 , \quad sin^2 2\theta_\odot = (0.53 \div 1) \tag{3.12}$$

---

[2]There exists other evidence for neutrino oscillation from the LSND experiment [Ath99]. Taking this data into account, the introduction of a sterile neutrino becomes neccessary. This solution is not taken into consideration here.
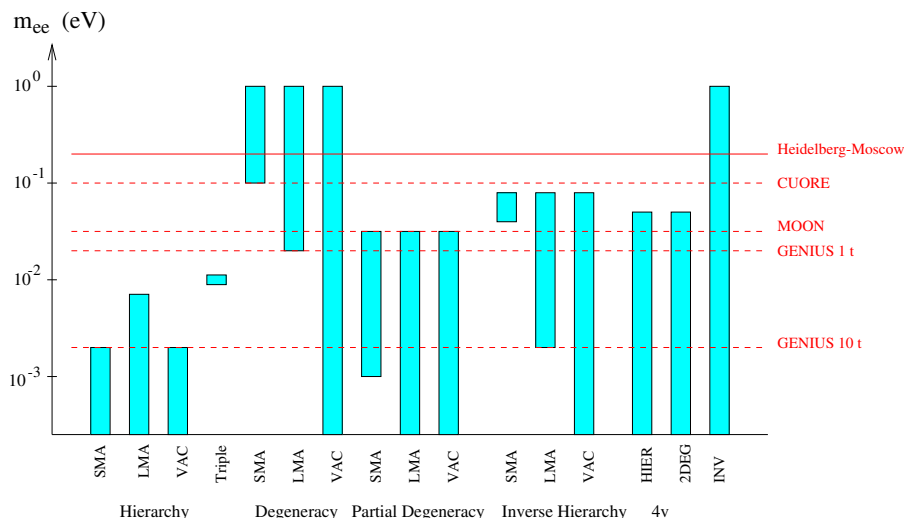
Figure 3.3: Summary of expected values for $\langle m_\nu \rangle$ (here denoted as m_{ee}) in the different schemes (from [Kla00c]). The expectations are compared with the recent neutrino mass limits obtained from the Heidelberg–Moscow [Hei99] experiment as well as the expected sensitivities for the CUORE [Fio98], MOON [Eji99] proposals and the 1 ton and 10 ton proposal of GENIUS [Kla99a]

Low Mass (LOW) MSW solution :

$$\Delta m_\odot^2 = (0.3 \div 2.5) \cdot 10^{-7} \mathrm{eV}^2 \ , \quad \sin^2 2\theta_\odot = (0.8 \div 1) \tag{3.13}$$

Vacuum (VO, just so) solution :

$$\Delta m_\odot^2 < 10^{-9} \mathrm{eV}^2 \ , \quad \sin^2 2\theta_\odot > 0.7 \ . \tag{3.14}$$

Once the solar neutrino problem is solved, further information from $0\nu\beta\beta$ is needed to constrain the different possible scenarios. An overview of the situation is given in figure 3.3. The y-axis represents $\langle m_\nu \rangle$ (denoted as m_{ee} there), the effective Majorana neutrino mass. On the x-axis the different allowed possibilities for mass scenarios are listed. The expected values for $\langle m_\nu \rangle$ are shown as filled bars. In the following the three possible solutions for the solar neutrino problem and their implications for neutrinoless double beta decay are discussed:

Confirmation of small mixing MSW solution:

- Measurement of neutrinoless Double Beta decay with $\langle m_\nu \rangle > 0.1$ eV would establish a degenerate mass scenario with a fixed mass scale.

- For $\langle m_\nu \rangle$ in the range $(5\text{-}8)\times 10^{-2}$ eV inverse hierarchy would be realized

- If $0\nu\beta\beta$ measurements reveal $\langle m_\nu \rangle$ between 2×10^{-3} eV and 3×10^{-2} eV a the mass scheme would be partially degenerate.

- For $\langle m_\nu \rangle < 1\times 10^{-3}$ eV a hierarchical mass scheme would be revealed, however, the absolute mass scale would not be fixed.

Confirmation of large mixing MSW solution:

- Measurement of $\langle m_\nu \rangle > 8 \times 10^{-2}$ eV would imply a degenerate neutrino mass scenario

- For $\langle m_\nu \rangle$ in the range $(5\text{ -}8) \times 10^{-2}$ eV either inverse hierarchy or degeneracy would be realized

- If $\langle m_\nu \rangle$ is between 2×10^{-2} eV and 5×10^{-2} eV the possible solutions are degenerate, partially degenerate or inversely hierarchical.

- In the range $(2\text{-}0.8) \times 10^{-2}$ eV either a partially degenerate or an inversely hierarchical mass spectrum is realized.

- If 2×10^{-3} eV $< \langle m_\nu \rangle < 8 \times 10^{-3}$ eV is the case, the solution is either hierarchical, inversely hierarchical or partially degenerate.

- If the $0\nu\beta\beta$ observable is smaller than 2×10^{-3} eV, either hierarchy or partial degeneracy are realized.

Neutrino oscillations in matter are sensitivie to the difference between direct and inverse hierarchy. Present data from SN 1987A favores direct hierarchy [Min00].

Vacuum (just so) solution:

- If neutrinoless double beta decay is measured with $\langle m_\nu \rangle > 8 \times 10^{-3}$ eV, the neutrino mass scale would be degenerate.

- For $\langle m_\nu \rangle$ lying in the range 0.05 - 0.08 eV the solution is either degenerate or inversely hierarchical.

- If $\langle m_\nu \rangle$ is measured to be 2×10^{-3} eV $< \langle m_\nu \rangle < 5 \times 10^{-3}$ eV, the scenario is either degenerate, partially degenerate or inversely hierarchical.

- For $\langle m_\nu \rangle < 2 \times 10^{-3}$ eV no information can be deduced about the absolute mass scale and the realized mass scenario.

If a four neutrino scenario is realized in nature, the situation is somewhat more complicated. However, $0\nu\beta\beta$ decay can give relevant information on the realized scenario in this case, too. For a discussion of this possibility see [Kla00c].

Chapter 4

Detection of rare events with HPGe detectors

In the previous chapters it was discussed that there exists strong evidence for some yet undetected weakly interacting massive particle population in our galactic halo. The fact that these particles should be around us and that they are weakly interacting, gives us in principle a chance to get hold of them by direct detection in detectors on earth. On the other hand evidence is very strong that neutrinos have a rest mass. If they are also of Majorana type, neutrinoless double beta decay should be observable with proper detectors. Both events, WIMP interactions and neutrinoless double beta, decay have in common that, if they occur, they are extremely rare. Thus special techniques have to be developed in order to make them visible within a reasonable time. One of the main tasks in experiments searching for rare events is the reduction of disturbing background events, which could be mistaken for a real signal.

This chapter first deals with direct detection of WIMPs and neutrinoless double beta decay in general. After that the principle of event detection in HPGe detectors is explained and special methods to reduce background are discussed.

4.1 Detection of Weakly Interacting Massive Particles

In principle there are two ways to find evidence for WIMP dark matter in our galactic halo. If WIMPs are indeed the particles making up cold dark matter, each second there must be hundreds to thousands of these particles crossing each square centimeter of earth. The simplest way to detect these hypothetical particles is direct detection, i.e. the measurement of the interaction between target nuclei and WIMPs traversing the detector.

The second possibility to get evidence for WIMP dark matter is through the detection of cosmic rays resulting from the annihilation of WIMPs in the core of our galaxy, the sun or in the center of the earth. For a review on this detection method see e.g. [Jun96].

In the next section the direct detection mechanism is discussed in some

detail.

4.1.1   Direct Detection of WIMPs

The method of direct detection of WIMP dark matter uses the principle of elastic WIMP scattering off nuclei of the detector material.

If such a recoil event occurs, the energy E_R, which is transmitted from the WIMP onto the target nucleus can in general be detected through a sensitive device. The deposited energy of an elastic scattering event for a non-relativistic particle inside a detector can be calculated using energy and momentum conservation (center of mass system WIMP-Nucleus):

$$E_R = E_0 r (1 - cos\theta) \qquad (4.1)$$

with θ the scattering angle, $E_0 = 1/2 m_{WIMP} v^2$ the energy of the incoming WIMP and $r = 4 m_{WIMP} m_N / (m_{WIMP} + m_N)^2$, where m_N is the mass of the scattered nucleus [Gon96].

If it is assumed that the scattering probability is the same for all $cos\theta$, i.e. isotropic, the recoil energy in the energy interval $0 \leq E_R \leq E_0 r$ is evenly distributed. Thus for the probability distribution of energy loss of the WIMP from one recoil event at the nucleus one can write:

$$P\left(\frac{E_R}{E_0}\right) \propto \frac{1}{r}. \qquad (4.2)$$

Through this equation it can be estimated in what regions typically the recoil energy of the nucleus will be. For WIMPs with masses below a few hundreds GeV the recoil signal would be below 100 keV. The probability distribution will increase with decreasing recoil energy, thus it becomes clear that a direct detection experiment is more sensitive, the lower its energy threshold. For two typical theoretical WIMP spectra see figure 4.1.

The frequency per unit mass of elastic recoils inside the detector with a target nucleus depends on the flux of WIMPs in the galactic halo and the WIMP-Nucleon scattering cross section σ. The count rate R of a detector in events per kg detector mass is given by

$$R = \frac{N_{Avo}}{A} n_0 \sigma \langle v \rangle. \qquad (4.3)$$

Here $n_0 = \rho_0 m_{WIMP}$ is the number density of WIMPs in our solar neighborhood, with ρ_0 being the local halo density and N_{Avo}/A is the number of possible scattering targets (N_{Avo}: Avogadro-number in Mol/kg and A the mass number of the nucleus) and $\langle v \rangle$ is the mean velocity of the WIMPs in the thermalized halo.

The calculations so far have been made for coherent scattering off the nucleus. If however the de Broglie wavelength of the in-falling WIMP becomes smaller than the size of the nucleus for increasing momentum, scattering will not be coherent anymore and material specific form factors have to be taken into consideration.

With equations (4.2) and (4.3) for the differential cross section follows (see [Jun96]):

$$\frac{d\sigma}{dE_R} = \frac{\sigma_0}{E_0} P\left(\frac{E_R}{E_0}\right) F^2(E_R) \tag{4.4}$$

and for the rate equation:

$$dR = N_T n_0 v f(v) \frac{d\sigma_0}{dE_R} dE_R dv. \tag{4.5}$$

Here N_T is the number of scattering targets, σ_0 the cross section for elastic coherent scattering off nuclei with vanishing momentum transfer, $F(E_R)$ the form factor for coherence loss and $f(v)$ the velocity distribution of WIMPs in the halo.

For the differential rate equation finally one gets:

$$\frac{dR}{dE_R} = \frac{2 N_T n_0 \sigma_0}{M_{WIMP} r} F^2(E_R) \int_{v_{min}}^{v_{max}} dv \frac{f(v)}{v} \tag{4.6}$$

with

$$v_{min} = \sqrt{\frac{2 E_{thr}}{r M_{WIMP}}}, \tag{4.7}$$

being the minimal velocity of a WIMP to still deposit a detectable signal above the energy threshold within the detector and the WIMP escape velocity from our galaxy v_{max}.

The total rate equation therefore is:

$$R = \int_{E_{thr}}^{E_{max}} \frac{dR}{dE_R} dE_R. \tag{4.8}$$

For a detailed calculation of the equations see e.g. [Lew96, Ram98a].

If all quantities in the rate equation are known, with equation (4.6) one obtains theoretical WIMP-spectra as shown in figure 4.1

Some of the input parameters still have to be derived: the WIMP mass M_{WIMP} and the scattering cross section σ_0 on the right hand side of the equation are purely theoretical values, on which the direct detection experiment can put constraints. For the WIMP density ρ_0 and the WIMP velocity distribution $f(v)$ astronomical observations can make some statements. These values are shortly described in the following.

One experimental approach is the use of High Purity Germanium (HPGe) detectors, which are described in some detail in chapter 4.3. For a detailed discussion of the influence of the form factor, especially the specific properties for HPGe-detectors see [Ram98a]. The ionization efficiency of nuclear recoil in germanium crystals has been measured and can be expressed through the semi empiric equation

$$E_{rec} = \left(\frac{E_V}{0.14}\right)^{1/1.19}, \tag{4.9}$$

where E_{rec} is the recoil energy of the target nucleus and E_V is the energy transformed into ionization.
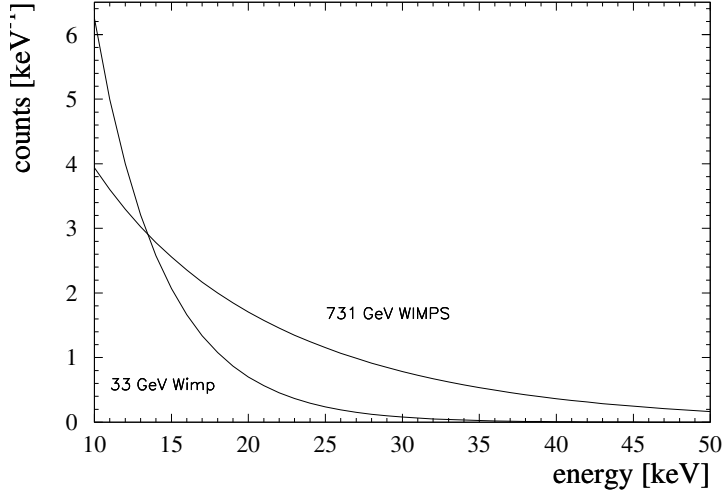
Figure 4.1: Theoretical recoil spectra for a 33 GeV and a 731 GeV WIMP.

The WIMP halo density and the velocity distribution

From observations of rotation curves of galaxies it becomes evident that most probably there is matter in regions far out from the galactic disk. However, also the galactic disk seems to be dominated by dark matter [Fuc00].

Estimates of the Halo density ρ_0 in form of dark matter result in values between 0.25 GeV/cm^3 and 0.7 GeV/cm^3 [Gat95].

To obtain an approximate value for the WIMP density, the most probable baryonic dark matter density in form of MACHOs is subtracted [Ben98]. The resulting value for the 'most probable' WIMP density is 0.4 GeV/cm^3 [Lew96]. The commonly used value in the literature is 0.3 GeV/cm^3.

If the distribution is considered in the galactic rest frame, the velocity of the WIMPs is Maxwell distributed and one gets:

$$f(v)dv = \left(\frac{1}{\pi \bar{v}^2} \right)^{3/2} v^2 exp\left(-\frac{v^2}{\bar{v}^2} \right) dv, \qquad (4.10)$$

where $\bar{v}$ is the dispersion velocity of the WIMPs, which can be calculated for a spherical symmetric isotropic halo through the rotational velocity at infinite distance:

$$\bar{v}^2 = \frac{3}{2} v_{rot}^2 \qquad (4.11)$$

v_{rot} is the rotational velocity of the sun around the galactic center [Lew96, Fre88]. Like this a dispersion velocity of $\bar{v} \sim 270$ km/s is calculated.

Thess data still have to be transformed to the rest frame of earth, which results in a correction of approximately 30 % [Fre88]. Furthermore the Maxwell tail of the distribution is cut off in the analysis since WIMPs with very high velocities will escape our galaxy. See [Ram98a] for a detailed discussion of this correction.

It should be stressed here that the uncertainty in the assumptions about our halo, like the spherical symmetry and the isotropy are very insecure. Lately it has become evident that our knowledge of the actual properties of the halo is very poor. Simulations even suggest that the halo could be clumpy, thus significantly changing the local WIMP density. However, in order to compare limits from different experiments, the representation of the data and the results has to be uniform. In general the above mentioned standard assumptions and parameters are assumed for the evaluation of experimental data.

Analysis method for experimental spectra

After all those terms from equation (4.6), which can be deduced from observations or astrophysical considerations have been discussed, it will be shortly explained, how physical relevant information can be extracted from an experimental spectrum.

If an energy sensitive detector provides a spectrum, the assumption is made that the whole spectrum results from nuclear WIMP recoil off the detector material. This is very conservative since in most experiments many underground components are well identified. Thus the the left hand side of equation (4.6) represents measured spectrum . The right hand side of equation (4.6) now has to be adjusted to the measured spectrum. For this purpose first the astrophysical parameters are fixed (velocity distribution, halo density). Then the unknown WIMP-mass is scanned: For each possible WIMP mass the theoretical spectrum is calculated, with the WIMP-nucleus cross section as the only free parameter. This theoretical spectrum is then fitted to the measured one by doing a least square fit, resulting in a value for σ_0, the cross section.

To be able to compare between different direct detection experiments it is still neccessary to translate the WIMP-nucleus into a WIMP-nucleon cross section. For the scalar, i.e. spin independent case this is not a problem since one can in general assume here that the cross sections are equal for WIMP-neutron and WIMP-proton scattering $\sigma_0^n \sim \sigma_0^p$. For the spin dependent case the calculation is somewhat more involved. Now the obtained total cross section depends on the specific MSSM model chosen to obtain a neutralino, i.e. it is different for different neutralinos. Also for this case it is possible to give limits in a model independent way, by projecting out the neutron and the proton parts of the cross section, thus resulting in two exclusion plots, one for σ_0^n and σ_0^p each [Tov00].

The obtained values are then depicted in a diagram, where typically the WIMP mass is on the x-axis and the WIMP-nucleon cross section on the y-axis. The information on such a diagram is the following: The measured spectrum excludes the existence of WIMPs with given mass M_{WIMP} and a cross section higher than σ_0 with a given confidence level.

4.1.2 The Annual Modulation effect

The direct detection mechanism discussed so far is only suitable for providing exclusion plots in the M_{WIMP}-σ_0 parameter space. As soon as a WIMP signal is present, there is no verification through the direct detection signal, i.e. the recoil spectrum, since the measured spectrum could as well be caused by some

unresolved background component. It is therefore important to have a signature of WIMP dark matter in order to be bale to verify a positive WIMP signal.

One of the signatures of WIMP dark matter is the annual modulation effect [Fre88].

Through the movement of the solar system around the galactic center an asymmetry in the WIMP flux in the solar rest frame is introduced (WIMP wind). For a detector in the earth rest frame the movement of the earth around the sun is superimposed onto the movement of the sun around the galactic core. This leads to a yearly variation of the asymmetry in the WIMP wind, which shows its effect through a modulated velocity distribution of WIMPs. Once a year WIMPs are hitting earth and any possible target (detector) on it with maximal mean kinetic energy ($\sim$ 2nd of June each year).

As seen from equation (4.6) the velocity distribution enters the expected spectral shape, thus a modulation effect of the WIMP nuclear recoil spectrum is expected as a signature of a thermal WIMP halo. The integral count rate will be increased at the maximum (since more WIMPs do actually have enough kinetic energy to deposit more than the threshold energy inside the detector) and the spectral shape will be slightly shifted. The frequency has to be one year with a maximum around the 2nd of June each year.

Since the typical modulation effect of the recoil spectrum is only in the range of a few percent, the problem arises to prove the modulation with high significance in an experiment with low counting rate including background. For a detailed discussion of the demanded properties of an experiment (target mass and background index) to see the annual modulation effect of a WIMP with given properties (M_{WIMP} and σ_0), see [Ram98a, Ram98b, Ceb99].

4.2 Observation of neutrinoless double beta decay

One of the isotopes known as a $\beta\beta$-emitter is ^{76}Ge. The advantage of germanium is that it can be used as source and as detector at the same time. The Q-value of the $\beta\beta$-decay of ^{76}Ge into ^{76}Se is 2038.56 keV [Hyk91].

The expected signal from double beta decay ($2\nu\beta\beta$ as well as $0\nu\beta\beta$) is seen in figure 3.2. Due to the fact that in the neutrino accompanied mode two neutrinos are emitted which carry away some energy from the detector, a continuous spectrum is expected for this decay mode. For the neutrinoless mode a sharp peak is expected at the Q-value of the decay since no neutrinos leave the detector.

In general, the reachable sensitivity for the half life of a $0\nu\beta\beta$ decay germanium experiment can be estimated using the semi empirical formula [Cal86]

$$T_{1/2}^{Sens} = (4.18 \cdot 10^{24} kg^{-1}) \frac{a}{f} \sqrt{\frac{M \cdot t}{\Delta E \cdot B}}, \qquad (4.12)$$

with

a : Degree of enrichment of the crystals with ^{76}Ge

f : statistical factor: 1.35 for 68% C.L. , 3.62 for 95% C.L.

M : active detector mass [kg]

t : Life time of the experiment [y]

B : Background index [Counts/(kg keV y)]

ΔE : Energy resolution in the region of the expected peak.

From equation (3.7) it is possible to derive the sensitivity of the experiment to the effective Majorana neutrino mass:

$$\langle m_\nu \rangle^{Sens} = \frac{1.53 \cdot 10^{12}}{\sqrt{T_{1/2}^{0\nu}}} eV y^{1/2} \qquad (4.13)$$

It is clear that the sensitivity to the half life of $0\nu\beta\beta$ of an experiment can only be improved significantly by enlarging the active mass of the experiment while suppressing the background index considerably in the same time. In figure 4.2 the reachable sensitivities and already obtained limits on half life and effective neutrino mass of future and current experiments on double beta decay are compared. It is evident that experiments based on the detection technique through HIgh Purity Germanium (HPGe) detectors have a higher discovery potential than any other experimental approach. Already now the Heidelberg–Moscow $\beta\beta$ experiment has reached a limit, which lies beyond the reach of most other running or planned experiments (except for the GENIUS project).

It should nevertheless be stated here that it is of great importance to investigate double beta decay using different independent approaches. Should $0\nu\beta\beta$ decay be observed, only an independent measurement could verify this important result.

It is the place here to explain the most important features and the functionality of High-Purity HPGe detectors in general to understand the PSA method to reduce the background used in the Heidelberg–Moscow $\beta\beta$ experiment.

4.3 The detection technique of HPGe detectors

The principle of radiation detection in HPGe detectors is based on the creation of electron hole pairs in semi conductor materials due to deposited energy inside the crystal. The energy width between valence and charge band is about 0.7 eV for germanium. The ionization energy is about 3 eV [Kno89]. Thus ionizing radiation with energies of tens of keV can produce several hundred electron hole pairs.

The energy width is however so small that at room temperature the thermal noise of germanium can excite electron-hole pairs. Therefore germanium has to be cooled below ~ 100 K in order to be sensitive to radiation. This is mostly done by bringing the HPGe crystals in thermal contact with liquid nitrogen (77 K) as a cooling medium.

In order to detect the created electron-hole pairs, the crystal has to be transformed into a diode since otherwise the charge carriers could be immediately compensated [Kno89]. In other words, the contacts for collection of the electrical charges created through ionizing radiation have to be blocking. This is best done by using p-n and n-p semi conductor junctions.
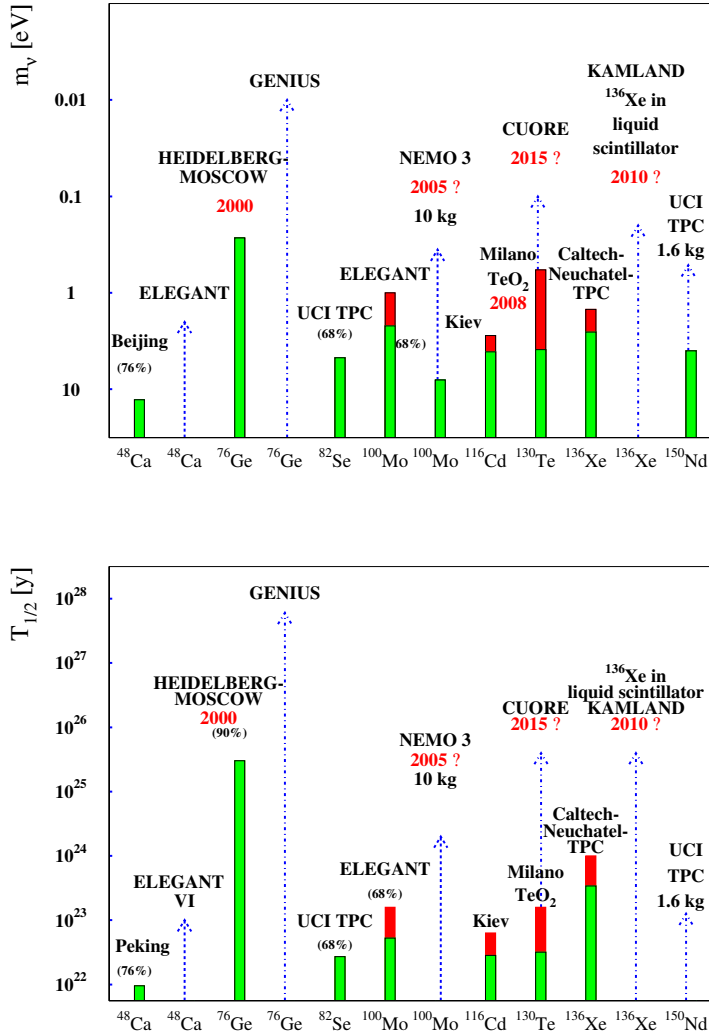
Figure 4.2: Current and future sensitivities of double beta decay experiments on half life (lower panel) and effective Majorana neutrino mass (upper panel). Green bars correspond to already obtained limits, red bars to sensitivities of running experiments. Dashed arrows denote projected sensitivities of experiments presently under construction and dashed-dotted arrows for planned experiments.
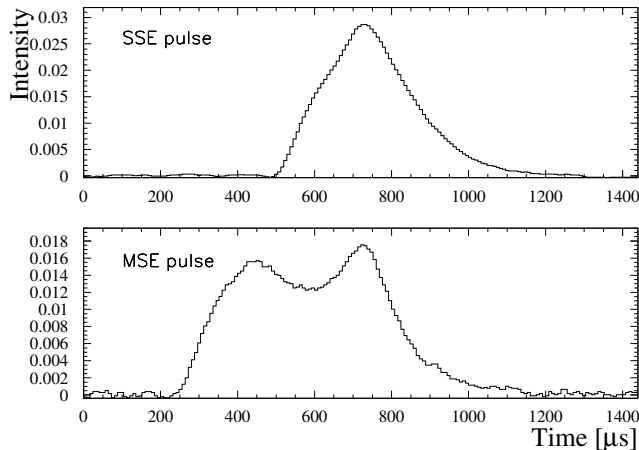
Figure 4.3: Examples for pulse shapes recorded with the Heidelberg–Moscow $\beta\beta$ experiment. In the upper panel an SSE event is seen. Only one maximum can be seen and the pulse is rather narrow. The lower panel displays a typical MSE event. Two maxima can be clearly distinguished and the width of the overall pulse is significantly larger than for the SSE pulse.

In practice this is done through dotation of the surfaces of the germanium material. If during the production of the germanium material atoms with a higher number of valence electrons than germanium (n-impurities) are implanted, the detector is said to be of n-type. In the opposite case the detectors are of p-type. If such a p-type detector is dotated with an n-impurity (acceptor, e.g. Li) on its surface, two zones with different charge distributions are created. The transition between the two zones happens through diffusion of the majority charge carriers. Thus in the region between the two zones the charge carriers will be depleted (p-n or n-p transition regions). The migration of the charge carriers induces a net voltage across the junction. If an ionizing event takes place in such a region, i.e. electron hole pairs are created, the charge carriers will move through the potential difference to the blocking contact, where they can be collected. The typical voltage across such a junction is about 1 V. Such a detector will not have a good performance since the charge carriers will not move rapidly. By applying a voltage in the direction causing the diode to be reverse biased, the majority charge carriers are pushed to the blocking contacts and the potential difference induced by diffusion of the charge carriers can be enhanced. The depletion region can be extended to several centimeters, which is the prerequisite for a good radiation detector. To have a reasonable radiation detector, it is essential that its size is larger than the mean free path of the radiation within the detector material. For a detailed introduction and discussion of semi conductor detector properties see [Kno89].

The terms 'Intrinsic' or 'High Purity' Germanium (HPGe) detectors denote the extremely low concentration of impurities in this material (less than 10^{10} cm^{-3}) [Kno89], which is neccessary to obtain a depletion of the detector material on the centimeter scale. Due to this reason HPGe detectors are perfectly suitable for the use of low level experiments. With such a detector system all kinds of ionizing radiation can be detected.

4.3.1 Digital Pulse shape analysis

The idea of distinguishing different interaction types by analyzing the pulse shapes of the events, i.e. the direct output signal of the detector, is realized for many detector types. This kind of analysis is also applied in the Heidelberg–Moscow $\beta\beta$ experiment for background recognition since 1995 [Hei97].

The idea is to look for differences in the output signal for different energy loss processes of the particles (photons or electrons) inside the detector. Since the main background results from photons, it is important to have a knowledge on the process of energy loss of photons inside materials. They deposit their energy in material through the following three processes:

- Photo-electric effect,

- Compton scattering,

- Pair creation.

The contribution to the energy loss of each effect strongly depends on the energy of the considered γ-particle. In germanium, below an energy of $\sim$250 keV the photo-electric effect dominates the energy loss. The photon is absorbed within one interaction by a germanium atom.

With increasing energy the contribution through Compton scattering with the electrons of the germanium atom increases. The energy of the scattered photon can be easily calculated from energy and momentum conservation:

$$h\nu' = \frac{h\nu}{1 + (h\nu/m_0c^2)(1 - cos\theta)},\qquad(4.14)$$

leading to a maximal energy deposition of

$$E_M = h\nu - E_e|_{\theta=\pi} = \frac{h\nu}{1 + 2h\nu/m_0c^2}.\qquad(4.15)$$

This is seen by the presence of the so called Compton edges in measured spectra.

Above the energy corresponding to twice the rest mass of the electron a photon can undergo pair production. In this case an electron and a positron are created inside the detector material. The electron will lose its energy through ionization and scattering. The positron will annihilate with another electron and emit two photons with 511 keV each, corresponding to the rest mass of the electron.

The distinction of single interaction processes inside HPGe crystals is not possible since in all three cases a cloud of electron hole pairs is created around the point of interaction. These charges drift towards the electrodes of the detector. Since the drift velocity of the electron hole pairs is low, the time resolution of germanium detectors is rather bad. Thus no distinction between the interaction types causing the ionization can be made. However, there is the possibility to distinguish between events in which energy is deposited at a single location within the detector,so called Single Site Events - SSE, and at more locations, through multiple Compton scattering for instance, Multiple Site Events - MSE [Hel96, Pet95].

In a double beta decay process two electrons are emitted. The mean range of electrons within the detector material grows exponentially with increasing energy. For a 1 MeV electron a range of 0.8 mm has been measured for germanium

[Muk76]. Since this is less than the spatial resolution of the germanium detector, these electron interactions appear as SSEs. Therefore all MSEs identified at the expected energy of the double beta decay can be regarded as background events.

In general the pulse shape from a single interaction inside the germanium is composed of the superposition of the currents of the electrons drifting to the n-contact and the holes drifting to the p-contact. MSEs can be regarded as superpositions of single interaction events. The shape of the MSE pulse will depend on the energy ratios of the single events inside the detector and their locations. The clearest signature for a MSE appears, if two events of approximately the same energy occur at different distances from the n- or p-contacts. In that case two maxima with approximately the same intensity are easily separated (see figure 4.3 for an example). In general MSEs will need longer time for all charges to be collected in the contacts since the spatial distribution of the charges is smeared out over a larger area than for SSEs.

From the simulation of calibration sources it is known that at an energy of 2 MeV, around the Q-value of double beta decay of ^{76}Ge an MSE fraction of ~ 0.35 is expected (see figure 6.2). If an efficient method is found to distinguish between MSEs and SSEs, the background can thus be decreased by a factor of approximately three. This in turn brings an effective increase of sensitivity.

Chapter 5

The Heidelberg-Moscow Experiment

The Heidelberg–Moscow $\beta\beta$ experiment is presently the most sensitive experiment looking for neutrinoless double beta decay [Kla87, Kla97, Hei99, Kla00e]. It is using germanium detectors which are embedded into an extreme low level surrounding.

In the final setup of the Heidelberg–Moscow $\beta\beta$ experiment [Gue97] five HPGe detectors made out of crystals enriched to 86-88% with ^{76}Ge are operated in a ultra low level background in the Gran Sasso underground laboratory in Italy since 1995 [Hei95, Kla97]. From non-observation of the neutrinoless double beta decay an upper limit on its half life can be extracted.

5.1 The setup of the Heidelberg–Moscow $\beta\beta$ experiment

Five HPGe detectors, enriched in ^{76}Ge to 86% are mounted in an ultra low level background surrounding. All the detectors were specially designed for their purpose, using only carefully selected low level copper. Four of the detectors are shielded with 40 cm of low level lead. The whole system is sealed inside a steal box which is flushed with gaseous nitrogen, in order to minimize the ^{222}Rn contamination in the direct surrounding of the detectors. The whole setup is surrounded by 20 cm of borated polyethylene plates to avoid the neutron influence on the detectors. On top of the construction a muon veto shield is installed which effectively recognizes any through going muons.

The fifth detector is housed inside a separate box without neutron shield and without muon veto. The inner shielding material here is electrolytic low level copper. The total active mass of the experiment with all detectors is 10.96 kg.

The most important parameters for the single HPGe crystals are listed in table 5.1

The energy signal is obtained with 13 bit MPI ADCs. For each detector a high- and a low energy spectrum is recorded.

The electronics of the Heidelberg–Moscow $\beta\beta$ experiment has been changed in 1995 to allow for recording of the pulse shapes of every single event in the

Detector	ANG1	ANG2	ANG3	ANG4	ANG5
Total mass	0.980 kg	2.906 kg	2.446 kg	2.400 kg	2.781 kg
Active mass	0.920 kg	2.758 kg	2.324 kg	2.295 kg	2.666 kg
saturation voltage		3000 V	3200 V	2900 V	1900 V
working voltage	4000 V	4000 V	4000 V	2500 V	2500 V
FWHM at 1332 keV		1.98 keV	1.91 keV	1.97 keV	2.06 keV
enrichment in ^{76}Ge [%]	85.9±1.3	86.6±2.5	88.3±2.6	86.3±1.3	85.6±1.3

Table 5.1: Technical data of the enriched Germanium detectors (from [Hel96]).

detectors ANG2, ANG3, ANG4 and ANG5 [Hel96, Hei97]. The preamplifier signal which is proportional to the charge collected at the electrodes, is being differentiated through the use of Timing Filter Amplifiers (TFAs). Two DL515 250 MHz Flash-ADC-modules are digitally recording these pulse shapes. Every 4 ns the voltage resulting from the TFAs is read. If a trigger occurs, the pulse shape is recorded. For a detailed description of the electronics of the experiment see [Hel96].

The very high sensitivity of the Heidelberg–Moscow $\beta\beta$ experiment with respect to other experimental approaches (see figure 4.2) bases on the following facts:

- With 10.96 kg active detector mass using enriched ^{76}Ge the source strength of this experiment is very high.

- The experiment is housed in a very clean surrounding, resulting in a very efficient background reduction.

- Detector and source are identical, resulting in a very high detection efficiency close to 100%.

- The use of Pulse Shape Analysis (PSA) leads to a further efficient background reduction.

5.1.1   The pulse shape analysis (PSA) used so far

For the identification of the pulse type in the analysis used so far several parameters were calculated from the pulse itself. As discussed before, the pulse shape will depend on the locations and the ratios of deposited energy of the single interactions inside the detector in one event. In the work done by Petry [Pet95] four parameters called *begin, end, local* and *broad* were derived which are representing some of the typical characteristics of the pulses. Later it was found by Hellmig [Hel96, Hel00] that actually the *broad* parameter alone is enough to distinguish between SSEs and MSEs. This parameter, calculated through the relation

$$broad = \frac{maxP}{|min\left(\frac{d^2P}{dt^2}\right)|} \tag{5.1}$$

is a measure for the width of the pulse, where P is the output signal from the TFA.
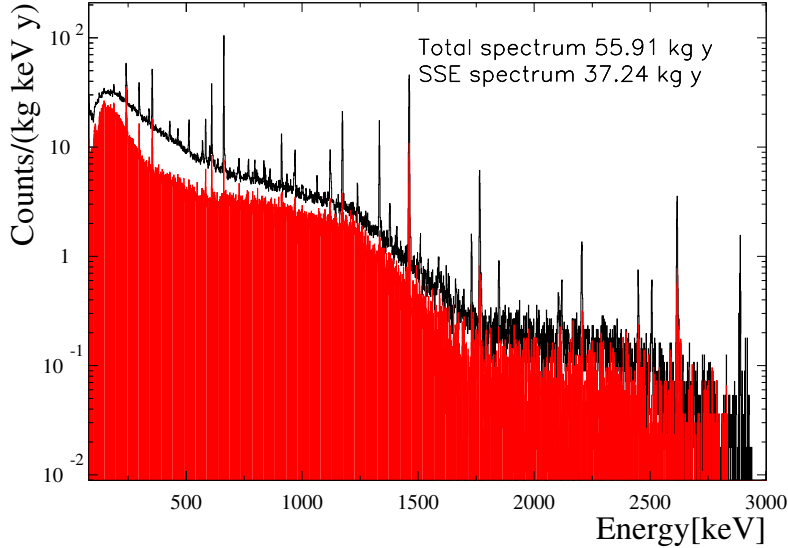
Figure 5.1: Energy spectrum from data gathered with the Heidelberg–Moscow $\beta\beta$ experiment. The open histogram represents the overall data before application of PSA (includes detector ANG1 and measurements before change in the electronics). The filled histogram denotes the energy spectrum after PSA for the measurements with pulse shape recording (ANG2 ,ANG3, ANG4 and ANG5 only). The significance of the measurements are 55.91 kg y for the overall spectrum and 37.24 kg y for the SSE spectrum.

The distinction between MSEs and SSEs is thus very straight forward. In a calibration measurement the typical parameter values are obtained for SSE and MSE pulses. A cut value is then derived for each detector which corresponds to the most effective separation between the pulses [Hel00]. These numbers are listed in table 7.2.

In the data analysis the *broad* parameter is calculated for each pulse and if the result is less than the cut value from the calibration measurement (table 7.2), it is classified as an SSE. This corresponds to a check of the width of each pulse, i.e. if the duration of a pulse is longer than a typical value, the pulse is considered an MSE.

The efficiency of the method is however not 100%. This has to be taken into account. The correction for this efficiency is discussed in detail in chapters 7.3.

5.1.2 Present status of the Heidelberg Moscow Experiment

The sum spectrum of the Heidelberg Moscow experiment containing all data from the latest analysis with a significance of 55.91 kg y is shown in figure 5.1. The background composition is well understood and has been discussed elsewhere [Die99, Hei97]. The identified activities are due to the U/Th decay chains, the decay of ^{40}K and cosmogenic and anthropogenic isotopes. The continuous background is composed of Bremsstrahlung photons and neutron and muon induced reactions. A detailed background model has been established

already in [Mai95], however, some improvements were lately achieved in [Die99]. Also shown in figure 5.1 is the spectrum containing only SSE events as resulting from the analysis described in the following chapters.

The $2\nu\beta\beta$ decay

Once the background model is known, it can be subtracted from the overall sum spectrum. The resulting rest spectrum should be due to the neutrino accompanied double beta decay. Like this a half life of

$$T_{1/2}^{2\nu\beta\beta} = (1.55 \pm 0.01(stat)_{-0.02}^{+0.03}(norm)_{-0.13}^{+0.16}(syst)) \times 10^{21} years \qquad (5.2)$$

was obtained in [Die99, Die00].

The SSE spectrum shown in figure 5.1 contains mostly $2\nu\beta\beta$ events in the energy region above 1000 keV, thus this spectrum roughly follows the spectral shape of the $2\nu\beta\beta$ decay.

Limit on the $0\nu\beta\beta$ decay

From the non-observation of a peak at the Q-value of the double beta decay a limit on the half life of the neutrinoless double beta decay can be derived. The latest limit [Die00] after 35.5 kg y of measurement is

$$T_{1/2}^{0\nu\beta\beta} \geq 1.9 \times 10^{25} \quad yr \quad 90\%C.L. \qquad (5.3)$$

$$T_{1/2}^{0\nu\beta\beta} \geq 3.1 \times 10^{25} \quad yr \quad 68\%C.L. \qquad (5.4)$$

The SSE spectrum was determined applying the old pulse shape discrimination method.

WIMP Dark Matter limits from the Heidelberg Moscow Experiment

One of the detectors, ANG2 was taking data in the low energy region below 100 keV in order to look for WIMP dark matter. A background index of 0.04 counts/(kg keV d) could be maintained. The detector had stable energy threshold of 9 keV.

The resulting exclusion plot in the $M_{WIMP} - \sigma_0$ parameter space (seen in figure 1.1) is presently the best limit using raw data [Hei98].

Chapter 6

Background rejection with Neural Networks

Since 1995 an additional background reduction has been achieved for the Heidelberg–Moscow $\beta\beta$ experiment through the use of Digital Pulseshape Analysis (PSA) (see chapters 4.3.1 and 5.1.1). Due to the fact that the shape of the detected pulse is dependent on the type of interaction a distinction between multiply scattered Compton events and single interaction events (as $0\nu\beta\beta$) is possible (see chapter 4.3.1). A $0\nu\beta\beta$ event would appear as a Single Site Event (SSE) since the mean free path of the two electrons emitted by the decay is smaller than the time resolution of the detector allows to distinguish due to the low drift velocities of the electron-hole pairs. This means that Multiple Site Events (MSE) in the energy region of $0\nu\beta\beta$ can be regarded as background. This allows for an effective reduction of background in the interesting energy region and thus an increase of sensitivity of the experiment.

In order to distinguish between the two interaction types a one-parameter method was developed at that time, based on the fact that the time structure of the pulse shapes in Germanium detectors are mainly dependent on the locations of the various events of a count within the HPGe-crystal. For MSEs one therefore expects a broader pulse in time than for SSEs since the initial locations of the electron-hole pairs are distributed over a larger area of the crystal and the overall detection time therefore increases. With this method a reduction of the background by a factor of three in the area of the expected signal could be reached earlier [Hel96, Hei97].

Nevertheless a large amount of information is neglected with this method since only one parameter serves as the distinguishing criterium. Furthermore the method relies on a statistical correction of the measured SSE pulses since the efficiency of the method is substantially smaller than 100% resulting in a loss of information about the single events. For this reason a new method based on neural networks was developed [Maj99] to use as much information as possible from the recorded pulse shapes and to minimize possible systematic effects being due to the statistical treatment of the obtained data.
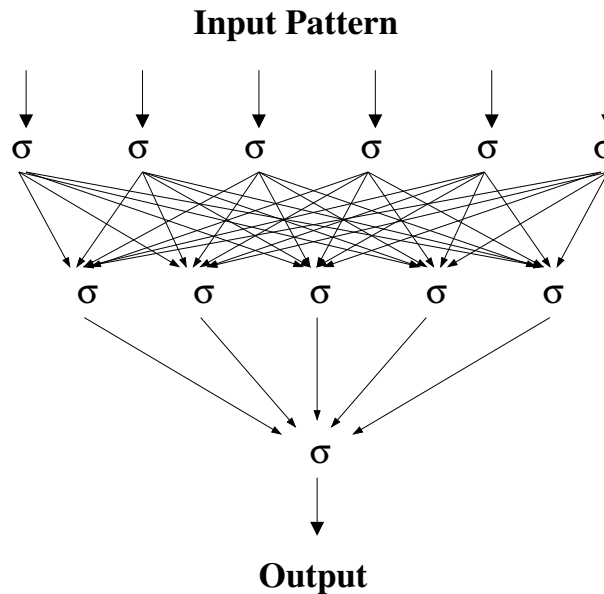
Input Pattern

Figure 6.1: Design of a feed forward Neural Network with three layers: one input layer, one hidden layer and one output layer. The σ at each knot represents the neuron's activation function which is of sigmoid type in our example. The network used for PSA here had 180 input neurons, 90 hidden neurons and 1 output neuron (compare with the 6 input neurons, 5 hidden neurons and 1 outpu neuron of the neural network in this figure).

6.1   Neural Networks

Neural Networks are nowadays used in a wide variety of applications like pattern-, image- and videoimage-recognition. Since in the case of PSA the discrimination technique relies on a sort of pattern recognition it seemed consequent to base a new PSA-technique on this method. In contrast to the old method, where only one parameter, the width of the pulse, i.e. its duration was used as the distinguishing criterium, all the information obtained by the measurement about the time structure of the pulse is fed to the neural networks in order to distinguish between SSE's and MSE's.

Typically a network is divided into processing units, which are further divided into single neurons. Each unit recieves signals from the previous level (i.e. from the neurons in the unit) and computes an output, which is then passed further to the next unit (i.e. to the neurons of the unit). The schematic action of such a feed forward network is depicted in figure 6.1.

A typical neural network consists of three layers: the input layer, the hidden layer and the output layer. It has been shown that such a network suffices to approximate any function with a finite number of discontinuities to arbitrary precision if the activation function of the hidden unit neurons is non-linear [Hor89, Cyb89].

If one has digitized information in an array (in our case it is the time evolution of the measured current behind the preamplifier, i.e. it is one-dimensional), the entries x_j can be passed to the input layer to 'activate' the neurons through

the activation function, typically of the sigmoid form

$$\mathcal{F}(x_j) = y_i(x_j) = \frac{1}{1 + e^{-x_j}}. \tag{6.1}$$

Each neuron then passes its activation value y_i to all the neurons in the hidden layer after multiplying it with a weight factor, so that the input to the neurons in the next layer is given by:

$$x_j^h = \sum_i w_{ij} y_i + \theta_j \tag{6.2}$$

where θ_j is a threshold specific to the layer and w_{ij} is the corresponding weight between the i-th neuron in the input layer and j-th neuron in the hidden layer. Again the output of the neuron is calculated through the activation function given in (1) and passed to the neurons of the next layer. Finally one obtains the output signals from the activation of the output neurons. Often (like in this analysis) the output layer consists of only one neuron returning a value between 0 and 1 thus deciding whether the data passed to the input layer belongs to a signal of type A) or B).

However the network has to be configured in order to be able to distinguish reasonably between two types of input patterns. This is mostly done by a sort of training process. If one has a library of input patterns, these can be passed to the network. After the input pattern has been applied and the output has been calculated, the connections between the neurons are adjusted according to the generalized delta rule:

$$\Delta w_{ij} = \gamma \delta_j y_i, \tag{6.3}$$

where γ is the learning rate, y_j is the activation of the neuron due to the given input pattern and δ_k is an error signal which in our case (sigmoid activation function) is given for the output layer by

$$\delta_o = (d_o - y_o)\mathcal{F}'(x_o) = (d_o - y_o)y_o(1 - y_o) \tag{6.4}$$

and by

$$\delta_h = \mathcal{F}'(x_h) \sum_{o=1}^{N_0} \delta_o w_{ho} = y_h(1 - y_h) \sum_{o=1}^{N_0} \delta_o w_{ho} \tag{6.5}$$

for the hidden layer. Here $\mathcal{F}'$ corresponds to the first derivative of the activation function, d_0 is the expected result of the output neurons and N_o is the number of output neurons. Often, like in this analysis, a momentum term is used in the learning process to avoid oscillations in the training procedure:

$$\Delta w_{jk}(t + 1) = \gamma \delta_k y_j + \alpha \Delta w_{jk}(t), \tag{6.6}$$

where t is the presentation number and α is a constant representing the effect of the momentum term.

After a certain number of these training procedures the network 'learns' the patterns of the types of input information and the output of the network results in a value close to zero for a pattern of type A) and in a value close to one for a pattern of type B).

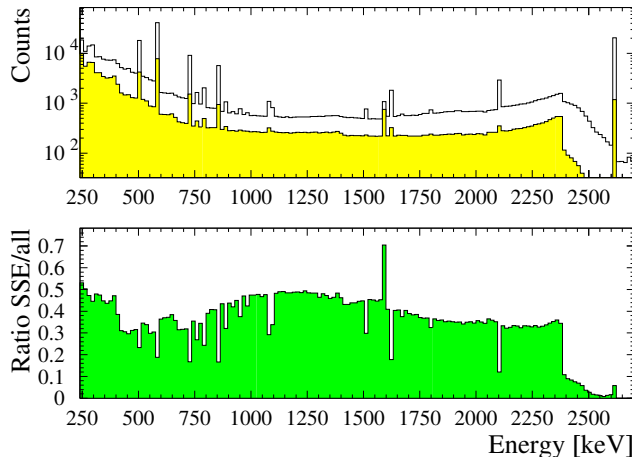For a general introduction to Neural Networks see for example [Krö96].

Figure 6.2: Expected result of PSA from the simulation of the ^{228}Th- calibration spectrum. Upper panel: Simulated spectra of all events (open histogram) and SSE events only (shaded histogram). Lower panel: Simulated ratio of SSE's in the spectrum as a function of energy. In the energy region of $0\nu\beta\beta$ a reduction by a factor of $\sim$2.8 can be expected.

6.2   Digital Puls Shape Analysis with Neural Networks

In order to perform PSA a sufficiently large library of known reference pulses has to be collected for the training process. A reliable source of the two different kinds of pulses is needed for this reason. It is well known that high energetic (E > 500 keV) total absorption peaks consist mainly of Compton scattered events (see. [Rot84]). The amount of MSE's in these peaks in general is not less than 80%. In contrast to this, Double-Escape peaks (pair production followed by the annihilation of the e$^+$ and the escape of both 511 keV γ's) consist of SSE's only since the detected particle in this case is a single electron with energy

$$E_{DE} = (E_0 - 2 \times 511 \ keV), \tag{6.7}$$

whose dissipation length again is smaller than the time resolution of the detector allows to resolve. Only the Compton background from higher energetic peaks in this area contributes to a contamination of MSE's in the peak region of the Double-Escape line. Using a ^{228}Th-calibration source, the Double-Escape line of the total absorption peak at 2614.53 keV with an energy of E$_{DE}$=1592.5 keV can be used for the SSE sample. To avoid systematic effects in the training process, a total absorption peak with a similar energy should be used for the MSE sample. The peak at 1621 keV from the ^{228}Th-daughter nuclide ^{212}Bi seemed appropriate for this purpose.

6.3   Simulation of PSA

To test the efficiency and the reliability of the new method simulations of calibration measurements of the Heidelberg–Moscow $\beta\beta$ experiment were per-
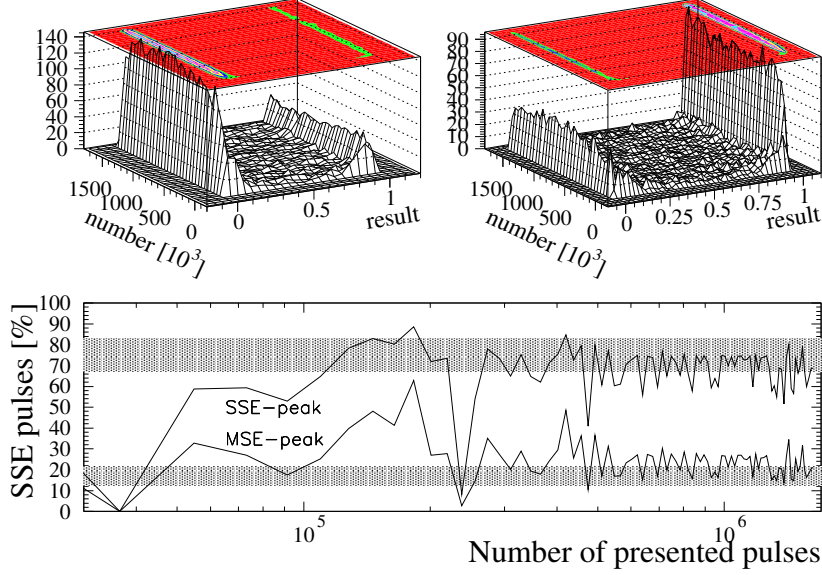
Figure 6.3: Evolution of the network during the training process. The result of the network after feeding it training pulses was monitored during the training process. Upper panel: The Events with the results from the network are shown as a function of the number of presented pulses. Left: Result from SSE-sample (1592 keV) Right: Same for MSE-sample (1621 keV). Lower panel: Fraction of identified SSE's in a given sample of reference pulses as a function of number of presented pulses. The shaded areas correspond to the expectation (one sigma band) obtained from the simulation.

formed. It is especially important to check for a possible energy dependence of the method since the energy of the training pulses (~ 1.6 MeV) does not coincide with the energy region of the expected $0\nu\beta\beta$ signature (2038.5 keV). For this purpose the GEANT3.21 Monte-Carlo code [GEANT] extended for low energetic decays was used. The geometry of the experiment and the library of low energetic decays was programmed and successfully tested in earlier works [Mai95, Die99]. The code was further extended to distinguish between multiple and single interaction events [Gun99]. In figure 6.2 the simulated spectra of a calibration measurement with a ^{228}Th source with the whole setup of the Heidelberg–Moscow $\beta\beta$ experiment and the resulting expected ratio of SSE's in the spectrum are shown. In the energy region of the $0\nu\beta\beta$ between 2000 keV and 2080 keV a reduction factor of $\sim$2.8 is expected through the use of PSA.

6.4 Network results

With every detector of the Heidelberg–Moscow $\beta\beta$ experiment ~ 20.000 events of each kind (1592 keV Double-Escape line and 1621 keV total absorption peak) were recorded. After arranging these pulses in a library, they were used to train the networks. Since the Pulseshapes are dependent on detector parameters like

Figure 6.4: Upper Panel left: Fraction of SSE's in the spectrum obtained using Neural Network (solid line), applying the one-parameter cut (densely dashed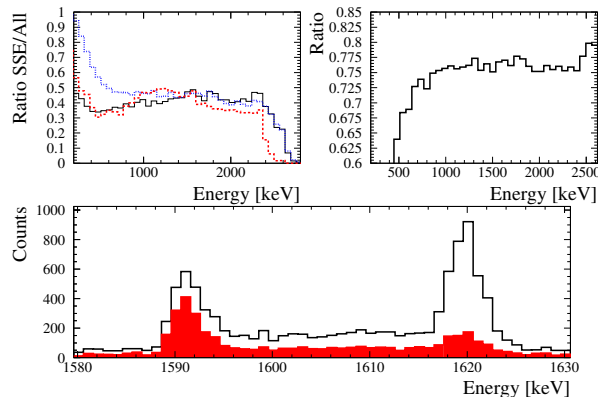 line) and the expectation from the simulation (losely dashed line). Upper panel right: Fraction of pulses identified identically by Neural Network and one-parameter cut. Lower panel: Measured spectrum in the energy region of the reference pulses (data independent of the training sample). The filled histogram corresponds to the identified SSE pulses. The open histogram shows the spectrum of all events.

size and form of the crystal, an own network had to be configured for every detector used in the PSA.

The Neural Networks used in this analysis consisted out of three layers: An input layer out of 180 neurons, a hidden layer with 90 neurons and an output layer with a single neuron.

To check the network also during the training process, the evolution of the network with time, i.e. with the number of presented pulses was monitored. This is shown in figure 6.3 for one of the enriched detectors: In the upper panel the output of the Network for the training peaks of the MSE and SSE lines are depicted separately as a function of time. It is evident that the network stabilizes after ~ 400.000 presented pulses (i.e. each pulse has been passed to the network ~ 10 times) and is able to distinguish between the two types of events. The fact that the network is able to identify the contamination of wrong pulses (from the admixture of SSE's to the MSE sample and of MSE's to the SSE sample) in the separate libraries gives us further confidence in the power of the method. This is shown in the lower panel. Here the fraction of identified SSE Pulses within the two samples of the training pulses is drawn as a function of presented pulses. The shaded areas give the one sigma region for the expectation obtained from simulations (see section 5). Note that the fraction of 'wrong pulses' in the libraries is not an input parameter to the training process. This behaviour is obtained solely by the presentation of the reference pulses, i.e. the Neural Network itself recognizes the contamination without previous knowledge.

From figure 6.3 it is obvious that further training of the network is meaningless after a certain limit, the obtained separation into MSE and SSE is not stabilizing further after ~ 400.000 presented pulses. The separation is fluctuating around its mean value from here on. This is probably due to the fact that a non-negligible amount of wrong pulses is contained in the training samples. In

principle it would be possible to remove a large amount of this contamination since the network identifies wrong pulses within the samples itself. However it seemed too dangerous to use this method for further training since this could give rise to sytematic effects.

Once the training process is finished, it is important to check the obtained results with independent data not used in the training process. One thousand events of each kind for every detector were saved to do this test. The result is seen in figure 6.5. As is evident, also for the independent data the separation works very well (for a quantitative analysis see section 7).
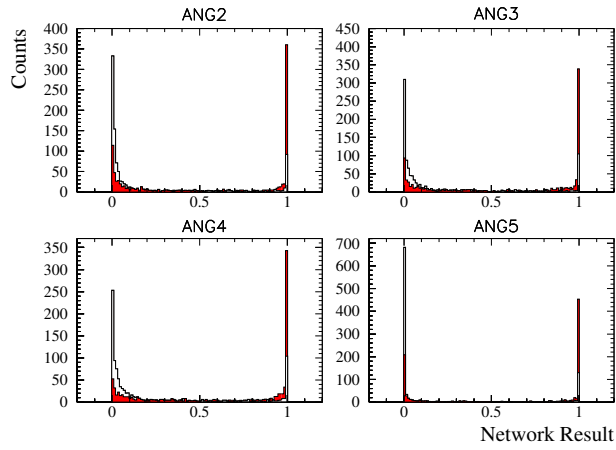
Figure 6.5: Result of the trained networks tested on independent data, i.e. on pulses which were not used for the training process. The blank histograms correspond to results of events from the SSE-library (expected result: 0), the filled histograms to events from the MSE-library (expected result: 1). Note that the network identifies the contamination with wrong pulses in the reference libraries correctly.

In figure 6.5 it is visible that for a non-negligible fraction of the pulses an output y_o between 0.1 and 0.9 is returned from the network, i.e. the pulses are not properly attributed to a definite type. The fraction of these pulses is $\sim$ 20% for all the detectors. This quantity can be identified as the efficiency of the separation. However, since there is further information from the simulation, this fact can be used first to adjust the outcome of the networks to the expectations from the simulation. We define a cut value ζ so that all pulses with $y_o < \zeta$ are identified as SSE. To adjust the network to the expected result ζ is varied and a least square fit for the simulated and measured SSE ratios over the whole energy range above 500 keV is performed. Having found the best fit, this cut is applied to the network result and thus the SSE-spectra are obtained. Note that separation between the two type of events has been obtained this way in figure 6.3. The result with this cut value ζ is then used to calculate the efficiencies e_s and e_m of the correct identification of SSE pulses and MSE pulses.

In the lower panel of figure 6.4 the obtained result for the energy-region around the reference pulses is shown. Most events in the Double-Escape-line are recognized as SSE's. Only a small fraction from the background contributes to a contamination of MSE's. Also the 1621 keV peak is recognized correctly to consist mainly of MSE's.

Detector	Ratio measured	Ratio simulated	Ratio measured	Ratio simulated
	Double-Escape Peak 1592 keV		1621 keV Peak	
ANG2	70.9±2.7	71.7±7.7	28.3±1.7	18.0±4.8
ANG3	72.4±2.7	75.1±7.8	29.2±1.7	17.5±4.7
ANG4	72.2±2.7	74.8±7.3	29.9±1.7	18.5±3.4
ANG5	76.0±2.8	76.4±8.5	28.7±1.7	17.4±4.5

Table 6.1: Fraction of identified SSE events in the peak areas of the Double-Escape 1592 keV line and the total absorption 1621 keV peak and their expectations from the simulation.

6.5 Comparison with the simulation and the old parameter cut

To compare the results of simulation and measurement directly, the measured and expected ratios of SSE's in the spectrum as a function of energy are shown in figure 6.4 together with the result from the old one-parameter method. It is evident that the result from the neural network is satisfactory over the whole energy range above ~ 500 keV. Only below ~ 1000 keV there is a noticable difference between the neural network method and the old method. Here the old cut yields too many SSE pulses. Note that especially in the energy region interesting for $0\nu\beta\beta$ (2000 keV-2080 keV) the agreement of the two techniques is very good.

In Tab. 6.1 the fraction of identified SSE's in the Double-Escape peak is listed for the four detectors together with the expected results from the simulation. As evident, the measured results are in good agreement with the expectation for the Double-Escape peak. The situation for the measured SSE fraction in the 1621 keV peak is slightly different. Since the efficiency e_m for correct identification of MSE's is not 100%, the actual measured SSE fraction within this peak is somewhat higher than the expected fraction from the simulation. Once the real fraction of SSE's in a certain energy region is known through e.g. a simulation, it is easy to calculate the efficiencies of the recognition:

$$e_s = \frac{1}{\gamma_s} + \left(1 - \left(\frac{a}{s}\right)_{SSE}\right) \frac{\frac{1}{\gamma_s} - \frac{1}{\gamma_m}}{\left(\frac{a}{s}\right)_{SSE} - \left(\frac{a}{s}\right)_{MSE}} \tag{6.8}$$

and

$$e_m = 1 - \frac{\frac{1}{\gamma_s} - \frac{1}{\gamma_m}}{\left(\frac{a}{s}\right)_{SSE} - \left(\frac{a}{s}\right)_{MSE}} \tag{6.9}$$

where $\gamma_m = s_{MSE}/S_{MSE}$ is the ratio of real SSE events in the 1621 keV peak to events identified as SSE's by the network within the peak, $\gamma_s = s_{SSE}/S_{SSE}$ is the according fraction for the Double-Escape-peak and $\left(\frac{a}{s}\right)_{MSE}$ and $\left(\frac{a}{s}\right)_{SSE}$ are the simulated ratios of all events to SSE events in the given energy region. The total efficiency e_{tot} of the method is then given by the square root of the product of the two single efficiencies.

The obtained efficiencies for the four networks in the Heidelberg–Moscow $\beta\beta$ experiment are listed in Tab. 6.2.

Obviously an efficient separation of MSE and SSE pulses can be accomplished with Neural Networks. In principle it is possible to correct the result of

Detector	e_s	e_m	e_{tot}
ANG2	0.93±0.27	0.86±0.25	0.90±0.38
ANG3	0.91±0.26	0.84±0.24	0.87±0.37
ANG4	0.91±0.19	0.84±0.17	0.87±0.27
ANG5	0.95±0.27	0.85±0.24	0.90±0.38
Combined	0.93	0.85	0.89

Table 6.2: Efficiencies for correct SSE and MSE identification for the detectors of the Heidel-berg–Moscow $\beta\beta$ experiment by neural network for the single detectors and for the combined method for the sum spectrum of all detectors recording pulse shapes.

the network through the known efficiencies with the relation

$$s = \frac{S - (1 - e_m)A}{(e_s + e_m - 1)}.$$
(6.10)

Here S is the number of SSE's identified by the network, A is the total number of events and s is the real amount of SSE in the sample A. In our case the correction yields a smaller SSE rate s then actually obtained with the neural networks S, since the number of MSE's identified as SSE's is larger than the number of SSE's identified as MSE's.

$$(1 - e_m)(A - s) > (1 - e_s)s.$$
(6.11)

Since the obtained efficiencies are high, the correction would be only of the order of 30% in the case of a large ratio $\frac{a}{s}$, as realized for total absorption peaks. The correction would be of the order of ~10% for the expected ratio in the $0\nu\beta\beta$ energy range.

From the ratio of identified SSE pulses in the energy region between 2000 keV and 2080 keV it is expected that the background in the calibration spectrum can be further reduced by a factor of 2.67±0.05 which is in good agreement with the results obtained from the simulation which yields a reduction factor of 2.78±0.01 and the one parameter-cut, which gives a reduction by a factor of 2.53±0.05 The slightly smaller value in the measurement is the effect of the efficiencies for the recognition. A similar reduction is expected for the Heidel-berg–Moscow $\beta\beta$ experiment.

To finally check the compatibility of the two methods, in the right diagram of figure 6.4 the fraction of pulses from the library which were attributed the same type from both methods as a function of energy are shown. With the efficiencies given above and the efficiencies of the old method a fraction of ~ 70 % is expected to be identified equally. Indeed ~75% of the events are classified equally.

6.6   Measurements with a ^{56}Co source

As mentioned before, the use of one SSE source only, is somewhat dangerous in terms of the possibility to introduce a systematic error. Since the double escape peak of the 2614.5 keV line of ^{228}Th lies at 1592.5 keV, more then 400 keV below the Q-value of double beta decay of ^{76}Ge, some energy dependency for the SSE recognition could be introduced to the method.

Detector	e_s	e_m	e_{tot}
ANG2	0.76±0.15	0.83±0.05	0.80±0.17
ANG3	0.78±0.14	0.86±0.05	0.82±0.15
ANG4	0.77±0.15	0.85±0.05	0.81±0.17
ANG5	0.75±0.15	0.94±0.04	0.84±0.17
Combined	0.77	0.87	0.81

Table 6.3: Efficiencies for correct SSE and MSE identification for the detectors of the Heidelberg–Moscow $\beta\beta$ experiment by neural network trained with two SSE libraries and the combined efficiency for the sum spectrum of the four detectors recording pulse shapes.

To avoid this possibillity a second pulse shape library was created using the double escape line of the 3253.4 keV peak of ^{56}Co at 2231.4 keV. Again ∼20.000 pulses were recorded for each detector and arranged in a library.

The networks were then trained using both SSE libraries, pulses from the ^{56}Co source and from the ^{228}Th source randomly chosen. The MSE library consisted of events from the 1620 keV and the 2614.5 keV peaks, thus ensuring that also here no energy dependence could enter.

Unfortunately the efficiency of the 2.2 MeV double escape peak, i.e. the fraction of SSE inside the three sigma region of the peak, is rather low, only around 55 %, due to the high energetic peaks of the decay of this isotope resulting in a very strong compton continuum superimposed onto the double escape peak. Thus the overall SSE fraction in the total library is reduced to approximately 65 %. However, the resulting trained networks proved to be as stable as the ones trained with the libraries of much higher SSE fraction.

As evident from a comparison of the networks obtained with the different libraries (tables 6.2 and 6.3), the efficiency obtained with the single SSE library seems to be somwhat higher. This is most probably the effect of the higher SSE purity of the library.

In the analysis described in the next chapter both networks were used, the one obtained with the 1592.5 keV double escape peak only and the ones resulting from the training with both libraries. As will bee shown later, the results do not significantly differ. In table 6.3 the efficiencies of the networks obtained with the mixed library are shown.

Chapter 7

Results: Analysis with neural networks

Once the raw data from the measurements with the Heidelberg-Moscow experiment is obtained, it is of great importance to analyze the data with great care in order to extract a limit on neutrinoless double beta decay. So far the analysis has been done using the code developed by Hellmig [Hel96]. Approximately every 6 months the new data from the Heidelberg–Moscow $\beta\beta$ experiment were investigated and added to the data obtained earlier. Thus the analysis was always only done for the new time interval of data taking.

In order to obtain a completely new analysis of the full data set of the Heidelberg–Moscow $\beta\beta$ experiment with pulse form recording, an independent evaluation code has been written. Some improvements with respect to the old code have been made leading to a further background reduction of ~ 10 % in the energy region of the Q-value of double beta decay.

In the following the procedure of the new data analysis code is discussed. Then the obtained spectra from the full data set are evaluated using the two different methods, neural networks and the old parameter cut. For the new method two neural networks resulting from independent training procedures are used. The obtained limits from the three procedures are discussed and finally compared to the old data analysis.

For the first time all the candidate events for $0\nu\beta\beta$ decay with all the relevant data, including the pulse forms are listed in the last section of this chapter.

7.1 Analysis procedure

Since 1995 the full setup of the Heidelberg–Moscow $\beta\beta$ experiment is running at the Gran Sasso underground laboratory. The pulse shape of every event resulting from 4 of the 5 detectors is recorded and analyzed off line.

The analysis procedure for a single run of typically 23 hours works as follows:

First the run is converted from CETIA format to ASCII and relevant data is recorded on a separate file for each run.

Some basic information on the run is written in the header: Start time, end time of the run, the active mass of the detectors used in the run as calculated

47

from the configuration file and the overall lifetime in seconds and in kg d, calculated from the active mass. Note however, that the active mass, as obtained from the configuration file, does often not correspond to the real active mass in the measurement since the configuration file of the data acquisition was not always changed, if one of the detectors was not running for some reason. The analysis of the real active mass of the run is done when summing the valid runs.

In the next step each recorded pulse is analyzed: For the treatment of the pulses, after conversion of the data to ASCII format, the constant baseline of the pulse is subtracted. The (integral) area is calculated, the pulse is then normalized to uniform area and it is passed to the networks of the proper detector for the analysis. The networks return their classification of the pulse as a number between zero and one. Also the *broad* value (see equation (5.1)) and the rise time of the old method [Hel00] is calculated. To have a quantitative measure for the quality of the pulse, the Energy over Integral (EoI) value is calculated by dividing the deposited energy in keV by the area of the pulse calculated before normalization.

The data for each event is written out in ASCII format: the number of the event, the detector identification number in which the event occured, time of the event, the time since the last muon veto signal (if less than $20\mu s$, otherwise zero), the Energy over Integral value, the results of the network obtained from the single SSE library, the result of the network obtained with mixed SSE library, the rise time of the event and finally the *broad* value of the old analysis method.

7.1.1   The Energy over Integral (EoI) value

For proper pulses the EoI value has to be constant for all energies since the energy signal of the ADC is obtained by integrating over the charge collected at the contacts of the detector, which corresponds to the area of the pulse recorded with the TFAs.

In the analysis done so far, the events were not checked for their EoI value. Some runs had been declared invalid, if the mean EoI value of the whole run was differing by more than 3 σ from the standard value. However, this is not sufficient since single pulses sometimes have a corrupt EoI value even though the whole run was normal. In this case the pulse is invalid and can not be used for proper distinction. In the new method all pulses with an EoI value differing by more than 3 σ from the mean value are counted as SSE not being considered as background.

The behavior of the EoI values has been studied in detail for all the four detectors taking pulse shapes. In figure 7.1 the time distribution of this value is shown for all the detectors considering only events with an energy higher than 1500 keV. Here the x-axis corresponds to the run number of the event (which is roughly proportional to the time passed since the first run), the y-axis corresponds to the EoI value. Each event is printed as a dot in the histogram.

The EoI distribution around the mean value becomes much wider if all events (including the low energetic ones) are considered (i.e. the FWHM of the Gaussian distributions shown in figure 7.4 becomes significantly bigger). This is what is expected since with decreasing energy also the area of the pulse is decreasing, thus increasing the absolute error for both, area and energy. As an example for this behavior the EoI values for the detector ANG3 are plotted as a function of energy in figure 7.2.
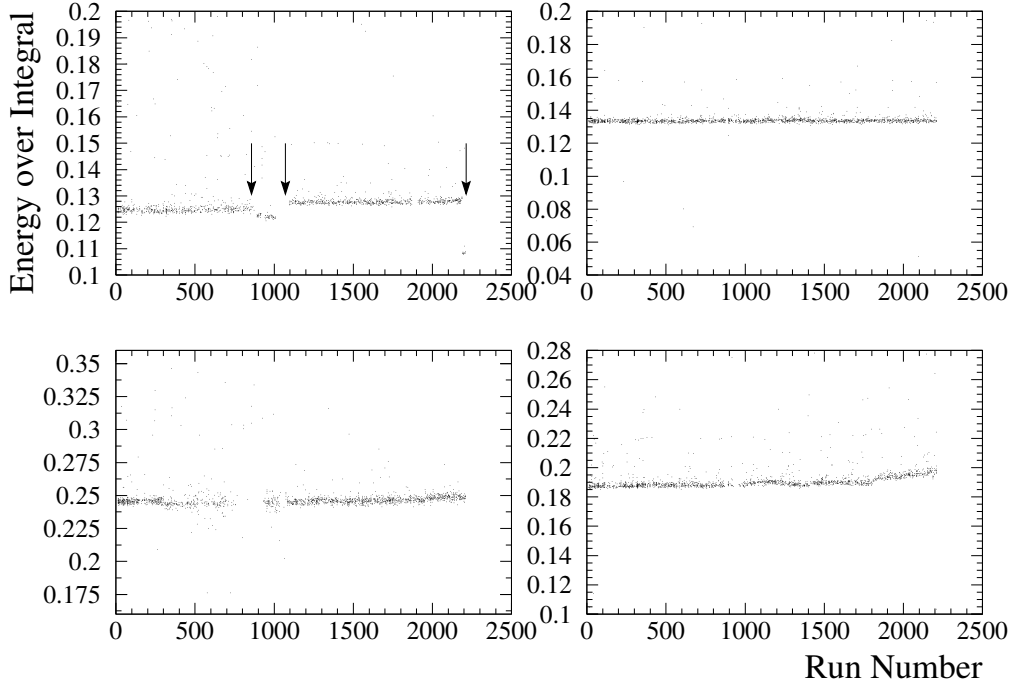
Figure 7.1: Time distribution of the EoI values for the four detectors with pulse shape analysis: Upper left: ANG2, upper right: ANG3, lower left: ANG4, lower right: ANG5. Each dot corresponds to one event with energy larger than 1500 keV. The behavior of the EoI values is discussed in the text for each detector separately.

As visible in figure 7.1, the bulk of the events clusters around a constant value. The distribution of the EoI values has a Gaussian shape as expected (see figure 7.4). However, there are some exceptions where the EoI value distribution seems to have some kinks:

In case of the detector ANG2 three jumps are seen in the histogram around the runs 892, 1100 and 2180. They are marked with arrows in figure 7.1. The first jump was caused by the change of the TFA module for ANG2 in October 1997 leading to a slightly different amplification of the pulses. The two later ones are due to the fact that the energy signal of ANG2 was divided in order to make possible a separate measurement for WIMP dark matter (see chapter 5.1.2). A division of the signal results in a decrease of the current reaching the TFA thus increasing the EoI value. This happened when the electronics of the HDMS detector was used for dark matter measurements with detector ANG2 from run 1100 on. Only in summer 2000 the electronics was changed again: the energy signal was not fed to the TFAs of the HDMS electronics anymore, thus increasing the signal for the Heidelberg–Moscow $\beta\beta$ experiment electronics again. This causes a jump in the EoI value around run 2180.

The detector ANG3 proved to be very stable over the entire time of data taking. The EoI values nicely follow a Gaussian distribution for the high energy sample (see figure 7.4).
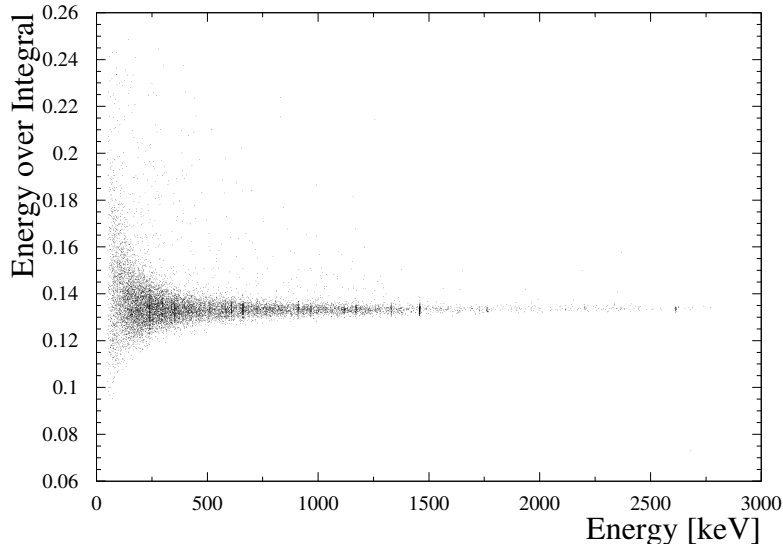
Figure 7.2: Distribution of EoI values as a function of energy of the event for the detector ANG3. Each dot corresponds to one event. As expected, the width of the distribution becomes wider with decreasing energy (see text).

The situation looks slightly different for detector ANG4. For a long time interval (runs 500 - 1100) the EoI values seem to be scattered quite arbitrarily around the mean value. This becomes clear from figure 7.3, where the time behavior of the EoI value is shown for ANG4 taking into account all energies. An investigation of the pulses in these runs showed that most of the events have a normal pulse shape. However, large parts of these runs were declared invalid because the EoI values were far from following a Gaussian distribution.

For the detector ANG5 the time distribution of the EoI value seems to be stable; the value follows a Gaussian distribution around the mean value at all times. However, lately the mean value has increased leading to a slight distortion of the EoI distribution over all times seen in the high energy sample for this detector in figure 7.4.

Despite some changes in the mean values for some of the detectors over time, all pulses can be used for the analysis. Since the pulses are normalized before being presented to the neural network and before calculating the *broad* parameter from equation (5.1), no information about the area of the pulses enters the procedure. The shape of the pulse does not change due to an increase or decrease of the area since the shape is a result of the detector geometry in combination with the integration and differentiation (preamplifier, TFAs) values of the electronics, which are unchanged over the time.

For the analysis of the spectra for $0\nu\beta\beta$ decay all events are checked for their EoI values. For events with EoI values outside a three sigma tolerance region around the mean value SSE parameters are assumed.

The mean value and the tolerance region are obtained by fitting a gauss function to the distribution over the whole time of the measurement. This is
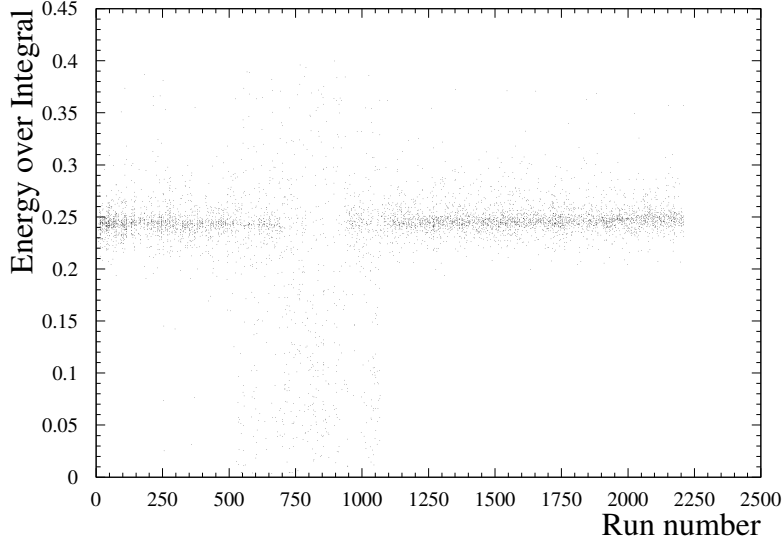
Figure 7.3: Time distribution of EoI value for the detector ANG4. Each dot corresponds to one event. Low energies are also included. For a discussion see the text.

also done for the detector ANG2. For the runs after the second (bigger) jump in the EoI value at run 2180 an extra fit was made, see table 7.1.

The mean EoI values with their one sigma error used for the analysis are listed in table 7.1 for all the detectors.

7.1.2   The used parameters

The parameters used by the separate methods for the distinction of SSE from MSE events are shown in table 7.2. If the obtained value for the event is smaller than the value listed, the event is counted as SSE, not being rejected from the further analysis.

The old cut parameter *broad* is calculated from the pulse shape using the relation (5.1) and denotes a measure for the width of the pulse [Hel96, Hel00].

The mixed network parameter is the result of the neural network trained with a library from two different SSE pulses (see chapter 6), after being fed with the pulse.

The single network parameter is accordingly the result of the neural network trained only by on kind of SSE library.

For the procedure of determining the cut values shown in table 7.2, see [Hel00, Hel96] for the old method and chapter 6.5 for the neural network method.

7.1.3   Creating the sum spectra

After creating the ASCII files for each run the events from the valid runs are summed using the code neural_beta_1.2. After reading the file containing all valid runs, a loop is done over these files.
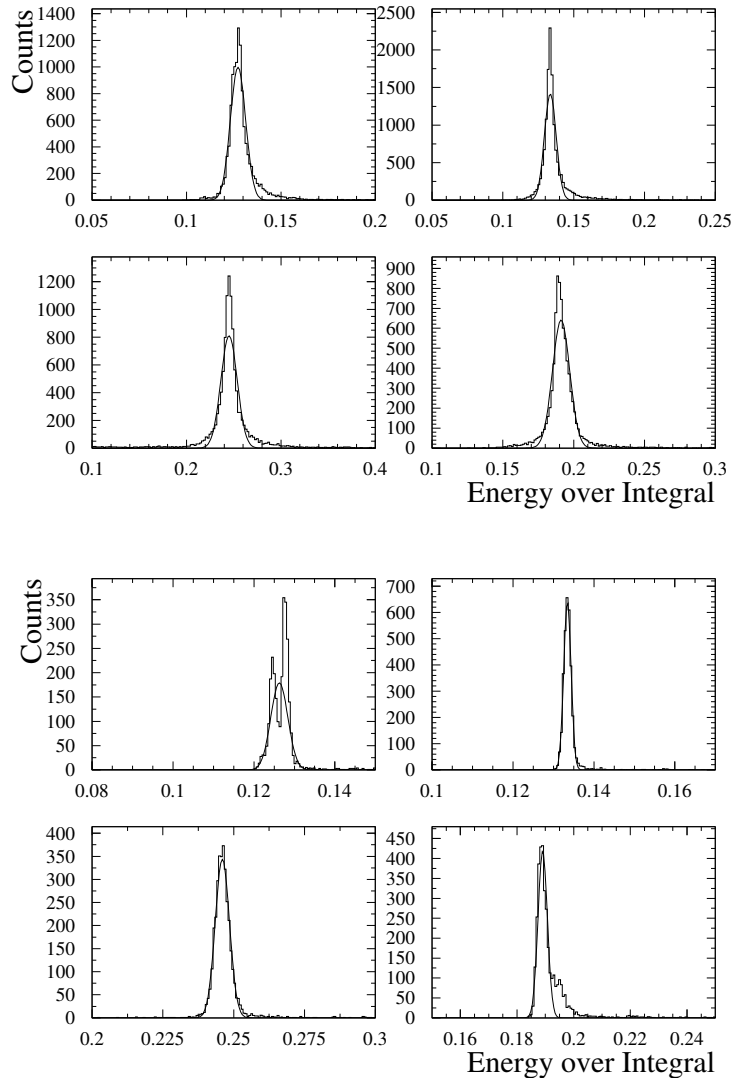
Figure 7.4: Distribution of EoI values around the mean for the four detectors. Upper diagrams: Distribution for all events including low energies. Lower diagrams: EoI values for high energetic events (energy larger than 1500 keV) Clearly visible are the two peaks for detector ANG2 resulting from the change in the electronics (see text). It is visible that for the higher energetic events the width of the Gaussian is smaller. The distributions in the upper diagrams do not follow a perfect gauss function because the width is different for different energies of the pulses. Thus for all energies the final distribution is obtained by summing over gauss functions of different widths.

First the header information is read for each run and the lifetime of the event is calculated from start and end time of the run. The run is discarded if the calculated value does not coincide with the time given in the header (this did not happen for any of the runs).

Detector	Mean EoI all energies	Mean EoI high energy
ANG2 runs 10 - 2180	0.1273±0.0041	0.1263±0.0021
ANG2 runs 2180 - 2210	0.1091±0.0023	0.1081±0.0014
ANG3	0.1335±0.0042	0.1335±0.0009
ANG4	0.2451±0.0087	0.2460±0.0025
ANG5	0.1911±0.0061	0.1891±0.0016

Table 7.1: Mean EoI values for the different detectors, obtained by fitting a Gaussian to the distribution of all EoI values over the entire time interval of data taking. For detector ANG2 a separate fit has been performed for runs later than number 2180 since the mean value had changed considerably (see text).

Detector	Cut parameter old method	cut parameter mixed network	cut parameter single network
ANG2	9.0	0.6	0.4
ANG3	9.2	0.35	0.3
ANG4	4.9	0.15	0.4
ANG5	5.5	0.35	0.5

Table 7.2: Cut value for the old parameter method [Hel96] and the neural networks. All pulses with the broad value or the network output higher than the proper parameter are considered MSE.

The entire data is then read and each event is analysed and checked for its properties separately. It is first checked whether the event results from a valid detector in this run. If this is not the case or if the event is a zero event (zero energy entry), it is skipped. A check is then done whether there has been a coincident signal in the muon veto or inside another detector. If this is the case, the event is added to the muon veto spectrum or to the coincidence spectrum, respectively, and the event is treated as background, i.e. it is omitted from the further analysis.

If the EoI value lies outside the above mentioned three sigma tolerance region (see table 7.1), the PSA parameters (network results and parameter *broad*) are set to zero as for the event to be treated as SSE in the following.

After these checks, the event is added to the overall spectrum. If the proper parameter is below the cut value listed in table 7.2 the event is also added to the SSE spectrum of the proper method.

After summation of the events from all valid runs, the spectrum is corrected for its efficiency if the option is set in the argument of invocation of the code.

To correct for efficiency equation (6.10) is used. The spectra resulting from the four detectors are first summed before the correction is made. This has to be done since the correction method is only valid, if the statistics of the spectrum is sufficiently high [Hel96, Hel00]. For certain ratios of total events to events classified as SSE by the method, it is possible that the corrected value is negative. This is unphysical, thus in this case the value remains unchanged.

The following energy spectra are finally recorded:

- Sum spectrum of all events from all detectors including ANG1.

- Sum spectrum of all detectors recording pulse shapes: ANG2, ANG3, ANG4 and ANG5.
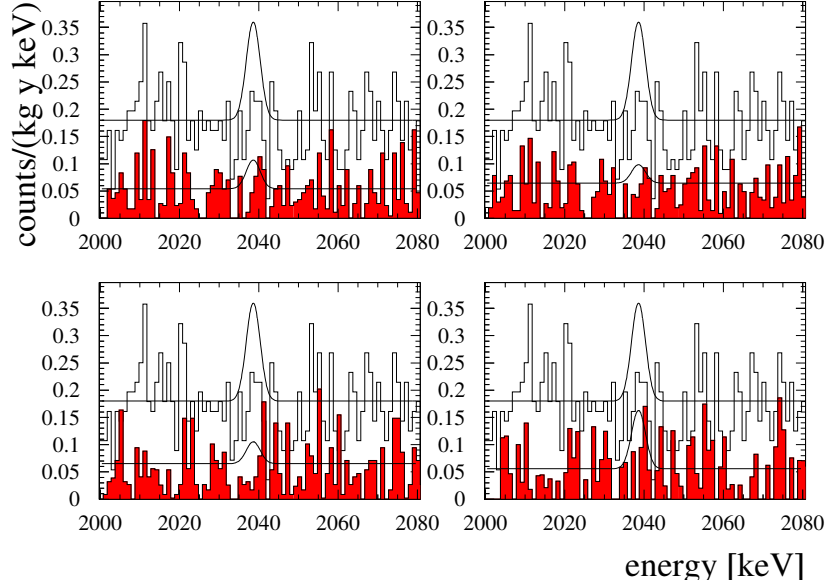
Figure 7.5: Spectra in the energy region of the Q-value of the $0\nu\beta\beta$ decay. The full spectrum including MSE events (open histogram) has a significance of 55.91 kg y. The SSE spectra (shaded histogrmas) have a significance of 37.24 kg y for the new data evaluation procedure and 37.59 kg y for the old evaluation. Plotted are also the excluded signals (90 %C.L.). The spectra have been corrected for the efficiency of the method. Upper panel: Left: Analysis with network from mixed SSE libraries, Right: network from single SSE library. Lower panel: Left: Result from old parameter cut, new data evaluation. Right: result from old parameter cut, old data evaluation.

- SSE spectrum resulting from neural network analysis using the mixed SSE library.

- SSE spectrum resulting from neural network analysis using the single SSE library.

- SSE spectrum resulting from the old parameter cut.

- Muon coincidence spectrum.

- Spectrum of coincident events in two or more detectors.

These spectra (the SSE spectra are recorded with and without correction for the efficiency of the method) are used to obtain the limit on $0\nu\beta\beta$ decay.

The life time of the SSE data from the new analysis is 37.24 kg d, which is slightly less than the 37.59 kg d of the old evaluation. This is due to the fact that ANG4 has been qualified invalid in many runs due to its EoI behavior. The significance of the overall data containing detector ANG1 which is not taking pulse shapes and the data from the experiment before reconstruction of the data acquisition to enable pulse shape recording is 55.91 kg d.
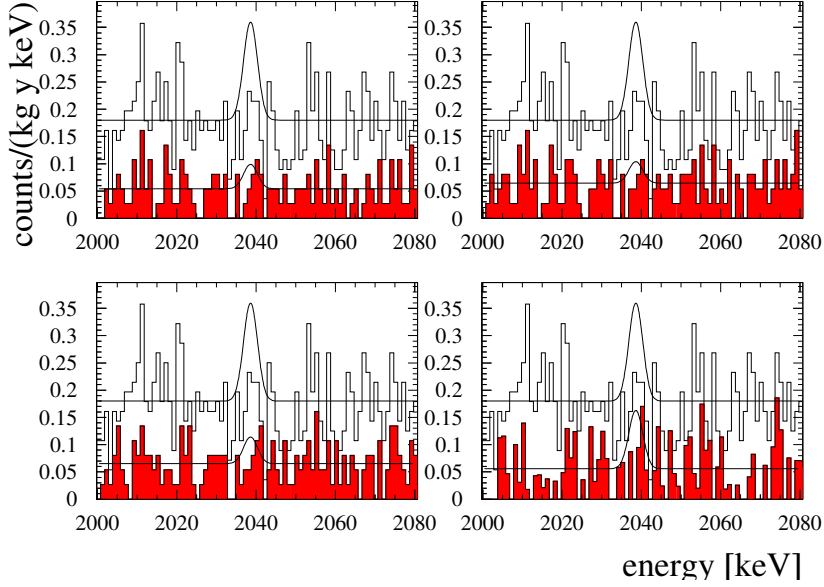
Figure 7.6: Like figure 7.5 but SSE spectra not corrected for efficiency of the method (except for lower panel right side, the old parameter cut with old data evaluation, where correction is done).

7.2 Different limits from different methods

From the different spectra obtained by the procedure described above, the limits for $0\nu\beta\beta$ decay are derived. The analysis follows the standard procedure used for the data analysis [Hei95].

In table 7.3 the relevant spectral data like life time, FWHM and background index are listed together with the obtained limits from the different spectra for 68%C.L., 90%C.L. and 99%C.L. To calculate the number of events excluded from $0\nu\beta\beta$ decay, first the number of expected background events in the three sigma region around the Q-value has to be calculated. This is done by counting the events occuring in the energy region between 2000 keV and 2080 keV in each spectrum. Two methods are then used to obtain the limit: First, following the suggestion of [PDG96], if the number of measured events is less than the number of expected events, the number of measured events is set equal to the number of expected ones. This is denoted as 'excluded a' in table 7.3. The second limit (excluded b) follows if the number of measured events within the three sigma region is used for the calculation of the number of excluded events.

The spectra in the energy region around the Q-value of double beta decay of ^{76}Ge resulting from the different methods are shown in figures 7.5 and 7.6 before and after the correction, respectively. Also shown is the excluded area (90% C.L.) for the spectra. Each spectrum also contains the full data without pulse shape analysis, including data from the detector ANG1.

	Old cut old eval. corrected	Old cut new eval. corrected	Old cut new eval. uncorr.	**Mixed network corrected**	Mixed network uncorr.	Single network corrected	Single network uncorr.	Total Spectrum No DPSA
Life time [kg y]	37.59	37.24	37.24	37.24	37.24	37.24	37.24	55.91
FWHM at 2038 keV	4.12	4.13	4.13	4.13	4.13	4.13	4.13	4.06
Background index	0.06	0.06	0.06	**0.05**	0.05	0.06	0.06	0.18
Events expected	19.3	20.6	24.2	**20.2**	20.1	20.9	24.06	117.7
Events measured	21.9	17.5	22	**16.2**	18	14.5	19	115
68%C.L								
Events excluded a	6.67	5.44	5.50	**5.08**	5.17	5.31	5.56	10.25
$T_{1/2}^{0\nu\beta\beta}$ [10^{25} years]	$\geq$2.8	$\geq$3.3	$\geq$3.2	**$\geq$3.5**	$\geq$3.5	$\geq$3.3	$\geq$3.2	$\geq$2.6
$\langle m \rangle$ [eV]	$\leq$0.29	$\leq$0.27	$\leq$0.27	**$\leq$0.26**	$\leq$0.26	$\leq$0.26	$\leq$0.27	$\leq$0.30
Events excluded b	-	3.62	4.54	3.39	4.14	2.96	3.50	-
$T_{1/2}^{0\nu\beta\beta}$ [10^{25} years]	-	$\geq$4.9	$\geq$3.9	$\geq$5.2	$\geq$4.3	$\geq$6.0	$\geq$5.1	-
$\langle m \rangle$ [eV]	-	$\leq$0.22	$\leq$0.24	$\leq$0.21	$\leq$0.23	$\leq$0.20	$\leq$0.21	-
90%C.L								
Events excluded a	10.84	9.14	9.33	**8.65**	8.67	8.98	9.41	17.50
$T_{1/2}^{0\nu\beta\beta}$ [10^{25} years]	$\geq$1.7	$\geq$1.9	$\geq$1.9	**$\geq$2.1**	$\geq$2.0	$\geq$2.0	$\geq$1.9	$\geq$1.5
$\langle m \rangle$ [eV]	$\leq$0.37	$\leq$0.35	$\leq$0.35	**$\leq$0.34**	$\leq$0.34	$\leq$0.34	$\leq$0.35	$\leq$0.39
Events excluded b	-	6.57	8.01	6.21	7.33	5.54	6.45	-
$T_{1/2}^{0\nu\beta\beta}$ [10^{25} years]	-	$\geq$2.7	$\geq$2.2	$\geq$2.9	$\geq$2.4	$\geq$3.2	$\geq$2.7	-
$\langle m \rangle$ [eV]	-	$\leq$0.29	$\leq$0.32	$\leq$0.29	$\leq$0.31	$\leq$0.27	$\leq$0.29	-
99%C.L								
Events excluded a	15.06	14.94	15.37	**14.30**	14.33	14.76	15.47	28.63
$T_{1/2}^{0\nu\beta\beta}$ [10^{25} years]	$\geq$1.2	$\geq$1.2	$\geq$1.2	**$\geq$1.2**	$\geq$1.2	$\geq$1.2	$\geq$1.1	$\geq$0.9
$\langle m \rangle$ [eV]	$\leq$0.44	$\leq$0.44	$\leq$0.45	**$\leq$0.43**	$\leq$0.43	$\leq$0.44	$\leq$0.45	$\leq$0.50
Events excluded b	-	10.15	12.07	9.66	11.11	8.78	10.06	-
$T_{1/2}^{0\nu\beta\beta}$ [10^{25} years]	-	$\geq$1.7	$\geq$1.5	$\geq$1.8	$\geq$1.6	$\geq$2.0	$\geq$1.8	-
$\langle m \rangle$ [eV]	-	$\leq$0.37	$\leq$0.40	$\leq$0.36	$\leq$0.38	$\leq$0.34	$\leq$0.36	-

Table 7.3: Limits obtained from the different data sets for different confidence levels. The quoted data from the mixed network after correction is highlighted. Quoted are the limits obtained following the suggestion of [PDG96], to set the number of measured events equal to the number of expected background events in case the number of measured events is less than expected (excluded a) and using the real number of measured events (excluded b). The limits for the effective Majorana neutrino mass are derived using the matrix elements from [Sta90].

7.3 Comparison of limits using various methods

As seen from table 7.3, the extracted half life limits for $0\nu\beta\beta$ do not vary significantly for any of the methods described before using the conservative approach as suggested in [PDG96], setting the number of observed events equal to the number of expected events. The excluded events (90%C.L.) insignificantly scatter around 9 events for the calculations. Only for the old method using the old data evaluation the number is above ten. The reason for this will be discussed later.

The variance is larger for the second analysis, where the real number of measured events is used to derive the limits. It is seen here that the correction for the efficiencies is significant: A reduction of the number of measured events of 23.7%, 20.5% and 10.0% is achieved for the single network, for the old parameter cut and for the mixed network, respectively. It is the place here to discuss the the effect of the efficiencies of the different methods.

7.3.1 The effect of the efficiency correction

The old method used two basic assumptions leading to a possibly systematic effect in obtaining the efficiency. It was assumed that a total absorption peak (with the background subtracted) contains exclusively MSE events and no SSE events. Accordingly for the double escape peak it was assumed that it contains only SSEs. The first assumption was quoted to lead to a systematic error in [Hel96], however, also the second assumption does lead to a systematic error, as can be seen from simulations of the double escape peak. From the first assumption alone, a systematic error of 24% was derived. Thus also taking into account the second assumption, the systematic error still increases significantly. A detailed investigation of this effect was not made here since the focus is on the new analysis method. Furthermore the old method was developed using a single SSE peak library only: the double escape peak of the 2614.5 keV line at 1592.5 keV. As mentioned before, this can lead to some energy dependence since the interesting energy region for neutrinoless double beta decay is at an energy approximately 400 keV higher than the mentioned peak.

The last argument also holds for the single network method since for the training of these networks also only the 1592.5 keV peak was used for the SSE library. As discussed in chapter 6.5, the resulting efficiencies from the neural network are very high (note the large error bars though) at the energy of the double escape peak. It is not known how the efficiency changes with increasing energy thus it seems somewhat dangerous to use the correction with the calculated efficiencies at a different energy than 1.6 MeV.

For this reason a second SSE library has been installed, containing a double escape peak at 2231.4 keV. Using the two SSE peaks at different energies, an energy dependence of the method can be avoided. Thus the possible systematic energy effect present in the old methods is minimized with the mixed neural network method. However, the fact that the double escape peak of the ^{56}Co is not very clean seems to reduce the overall efficiency of the method. The main systematic error entering the calculation of the efficiency here is the simulation, which is needed to determine the real ratio of SSE events inside the double escape peak.

The problem with all the methods described here is that their efficiencies

are not known with very good accuracy. It is therefore interesting to investigate the expectations from the corrections and compare it to the measured outcome.

It is interesting to investigate the relation between corrected and uncorrected data, i.e. the conditions for which the number of SSE events S recognized by the method is larger than the real number s of SSE events. First remember equation (6.10) through which the correction is done:

$$s = \frac{S - (1 - e_m)A}{(e_s + e_m - 1)}.$$ (7.1)

Assuming that a fraction f of the overall spectrum inside the considered energy interval is SSE events: $s = f \cdot A$, it is easy to calculate the fraction $\frac{S}{s}$:

$$\frac{S}{s} = e_s - (\frac{1}{f} - 1)e_m + (\frac{1}{f} - 1).$$ (7.2)

Thus for

$$f < \frac{1 - e_m}{2 - e_s - e_m}$$ (7.3)

the ratio $\frac{s}{S}$ will be less than 1, as demanded. If it is assumed that $e_s = e_m$, it immediately follows that this is always the case if $f < 0.5$. The argument still holds if $e_s \geq e_m$, like it is the case for two of the methods used here (old parameter cut, single network, see table 6.3).

Plugging in the efficiencies for the different methods into equation (7.3) yields the relations:

- $f_m < 0.4$ for the mixed network method

- $f_s < 0.65$ for the single network method

- $f_o < 0.56$ for the old parameter cut

Since the expectation for the fraction f of SSE events in the background of the relevant energy region is around $f_{exp} \sim 1/3$, it is at least for the single network and the old parameter cut method conservative to assume S > s.

For the mixed network method the fraction f_m is on the order of the fraction awaited for the relation s=S to be fulfilled, thus, if the considerations made so far are correct, it is expected for this method that no reduction will be achieved through the correction. Indeed, this method yields the smallest correction of all methods, 10% for the measured events in the three sigma energy interval and even a complete agreement for the background interval.

Another way to determine the quality of the correction is by comparing the results of the different methods before and after the correction. Since the efficiencies for the three used methods differ, a significant difference should be observable in the uncorrected spectra. If the correction for the efficiency is good, this difference should vanish completely. This is shown in figure 7.7. Indeed, the uncorrected SSE fractions do systematically differ by up to 20 percent. This situation changes after the correction for efficiency. The fractions now coincide nearly perfectly for the two neural networks and agree well for the old parameter cut method, at least in the relevant energy region above 1600 keV. This is strong support for the validity of the correction and gives confidence in the obtained efficiencies, despite the arguments discussed above.
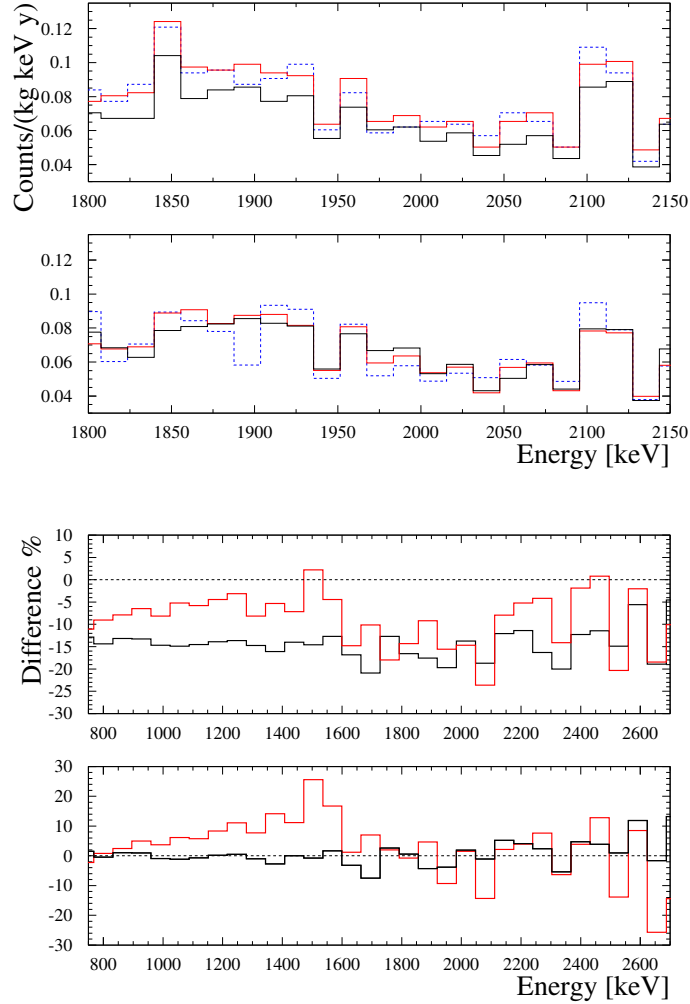
Figure 7.7: Effect of correction for efficiency for the three applied methods. Upper two histograms: In the upper panel the SSE spectra as recognized by the methods are shown as a function of energy. In the lower panel the SSE spectra after correction for efficiency are plotted. The red curve corresponds to the single network, the black curve to the mixed network and the blue striped curve to the old parameter cut method. Lower two histograms: Difference in the fractions of SSE pulses recognized by the methods. In the upper panel, corresponding to the uncorrected spectra, the values systematically differ form zero. In the lower panel the differences are shown for the corrected spectra. They are here in agreement with zero over the whole energy range for two network methods (black curve) and are consistent with zero for high energies for the difference between the mixed network and old parameter cut methods.

Therefore it is legitimate to use the limit obtained from the SSE spectrum after the correction. The limit quoted in the following is derived from the SSE energy spectrum corrected for efficiency obtained with the mixed network.

7.3.2   Comparison with the old data evaluation

In the new data analysis two major differences have been made with respect to the old evaluation code, which can explain the different outcome of the two evaluations.

Coincident events

The main reason for the improved limits is the fact that the new data evaluation code recognizes coincident events (with muon veto and with a second detector) and omits them from the further analysis. This has not been done in the old evaluation code. Since the spectra of coincident events are recorded separately, it could be calculated how much these events contribute to the overall spectrum. As seen from figure 7.8 $\sim$10% of the events in the energy region from 2000 keV and 2100 keV are coincident. Thus the background could be reduced by another 10% with respect to the former analysis.

Correction for efficiency

Other important changes, which have been made in the evaluation code regard the correction for the efficiency of the SSE recognition. As stated before and quoted in [Hel96], it is only allowed to make the correction for good statistics. This is drastically seen, if the correction equation (6.10) is considered. Assume that $\frac{S}{A}$ is smaller than (1-e_m). In this case the 'correct' number of SSE events becomes negative! This happens for all energy intervals, where only MSE events have been recognized by the method.

In the analysis done so far this effect was corrected by setting the energy bin to zero if a negative value resulted from the correction. In the new analysis the energy bin remained uncorrected if this occured, making the new procedure more conservative. In effect this difference does not change the outcome of the result significantly. As mentioned above, the corrected value mostly becomes negative, if only MSE, but no SSE events have been recognized. Both methods therefore set the SSE spectrum to zero in this case.

Much more significant is the fact that in the former analysis the correction has been made before summing the spectra of the different detectors. Since the statistics of the experiment is still not very high, especially for a single detector, it seems much more reasonable to first sum the spectra before correcting them for efficiency.

7.4   The new limit

As a result from the new data analysis using neural networks, the limit obtained from the SSE spectrum of the mixed network, corrected for efficiency is quoted.

The number of expected background events in the three sigma region around the awaited peak is 20.18$\pm$1.62. The number of measured events in the same energy interval is 16.19. Since there are less events observed than expected, the limit is obtained following the suggestion of [PDG96], to set the number of observed events equal to the number of expected events in this case. Thus 8.65 (5.08) events can be excluded with 90% C.L. (68% C.L.) to be due to neutrinoless double beta decay.
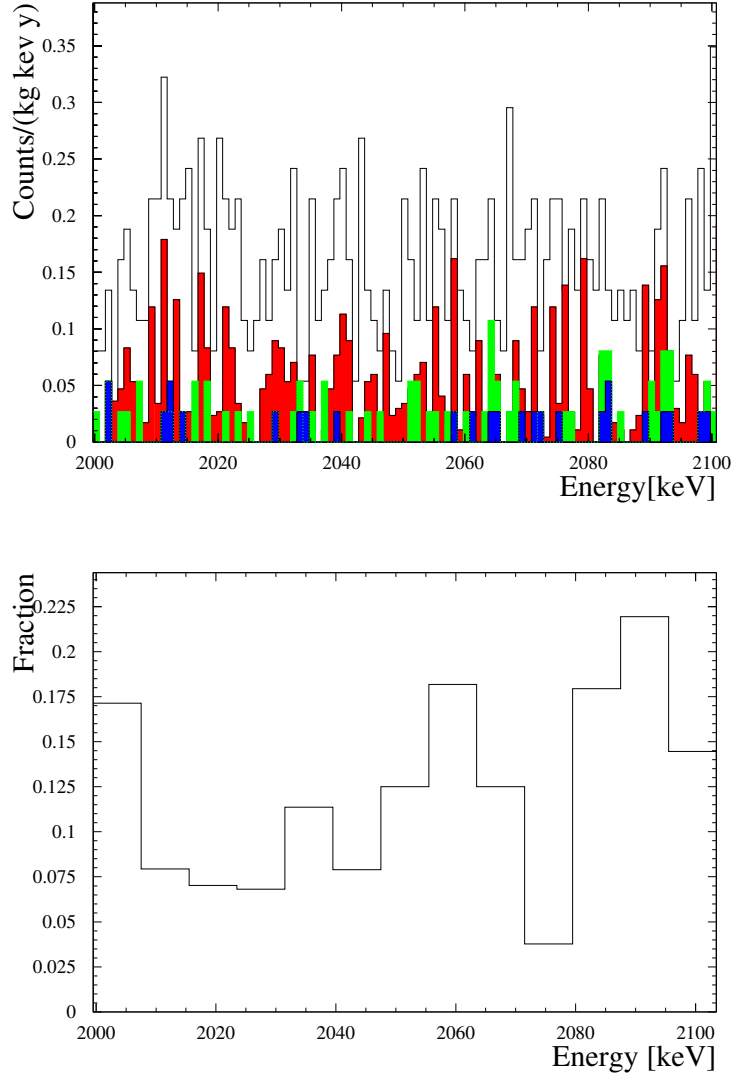
Figure 7.8: Upper diagram: Plotted are the sum spectrum of all events (open histogram), the corrected SSE spectrum resulting from the mixed network (red shaded histogram), the spectrum from coincident events within two detectors (green shaded histogram) and the events, which were coincident with the muon veto (blue shaded histogram). Lower diagram: Fraction of events coincident in two detectors in the energy interval 2000 keV to 2100 keV with respect to the sum spectrum of all events.

The corresponding spectrum with the excluded area (90 % C.L.) is shown in the upper left panel of figure 7.5.

For the half life of $0\nu\beta\beta$ decay the following lower limit can be given:

$$T_{1/2}^{0\nu\beta\beta} \geq 2.1 \times 10^{25} \text{ yr} \quad 90\% C.L. \tag{7.4}$$

$$T_{1/2}^{0\nu\beta\beta} \geq 3.5 \times 10^{25} \text{ yr} \quad 68\% C.L. \tag{7.5}$$

If the real number of measured events is taken for the analysis, a better limit is resulting from the analysis. In this case 6.21 (3.39) events could be excluded with 90 % C.L. (68 % C.L.) to be caused by neutrinoless double beta decay.

This would result in a limit on the half life of:

$$T_{1/2}^{0\nu\beta\beta} \quad \geq 2.9 \times 10^{25} \text{ yr} \quad 90\% C.L. \tag{7.6}$$

$$T_{1/2}^{0\nu\beta\beta} \quad \geq 5.2 \times 10^{25} \text{ yr} \quad 68\% C.L. \tag{7.7}$$

This result gives also a limit on $\langle m_\nu \rangle$ however it should be taken with some care as it is based on a dip in the measured spectrum. A previous analysis [Hei99] quoted a limit of $T_{1/2}^{0\nu\beta\beta} \geq 5.7 \times 10^{25}$ yr with 90 % C.L., where a similar dip was observed, thus increasing the lower limit. Shortly after this publication the number of measured events grew above the number of expected events, leading to the limit quoted in chapter 5.1.2 [Die00].

Taking the conservative limit, following [PDG96], using equation (3.7) and the matrix elements from [Sta90], the lower limit on the half life of $0\nu\beta\beta$ can be converted into an upper limit for the effective Majorana neutrino mass:

$$< m_\nu > \quad \leq \quad 0.34 eV \quad 90\% \ C.L. \tag{7.8}$$

$$< m_\nu > \quad \leq \quad 0.26 eV \quad 68\% \ C.L. \tag{7.9}$$

7.5   The $0\nu\beta\beta$ Candidates

For the first time here the candidate events for $0\nu\beta\beta$ decay are shown and discussed in detail. All events which had an energy within the 2.85σ region around the Q-value of the double beta decay count as candidates. The FWHM value of the full data set is 4.13 keV, thus the tolerance region for candidates is 2033.58 keV - 2043.58 keV. In figures 7.9 to 7.15 the pulse forms of all the recorded events in the peak region are shown. Note that also the events from invalid runs (runs, which have not been used for the analysis of $0\nu\beta\beta$ decay) are listed here. These candidates are labeled. Open histograms correspond to events classified as MSEs by all three methods. Striped histograms are events, which have been graded SSE by one of the three methods, cross striped histograms are SSEs by the means of two of the procedures and the dark shaded histograms are uniformly judged as SSEs, thus corresponding to the most probable candidates for $0\nu\beta\beta$ decay. In table 7.4 the relevant data of the candidates is shown in detail, also for the detector ANG1, for which no pulse shape data is taken. The candidates resulting from invalid runs are marked with a star. Listed is the event number, the time of the event in days after the start of the first measurement with pulse shape analysis, the exact energy, the EoI value (compare to table 7.1) and the outcome of the three mentioned discrimination procedures. In the last column the classification from the three methods is listed. For a uniform grading of the three procedures the resulting type is listed, if the outcome is different for two procedures, the ratio of methods resulting in SSEs is listed.

Figure 7.9: Candidates 1-12. Open histograms correspond to pulses classified as MSE by all three methods. Striped histograms have been rated as SSE by one, cross striped histograms by two of the three methods. Dark shaded histograms have been classified as SSE by all three methods.
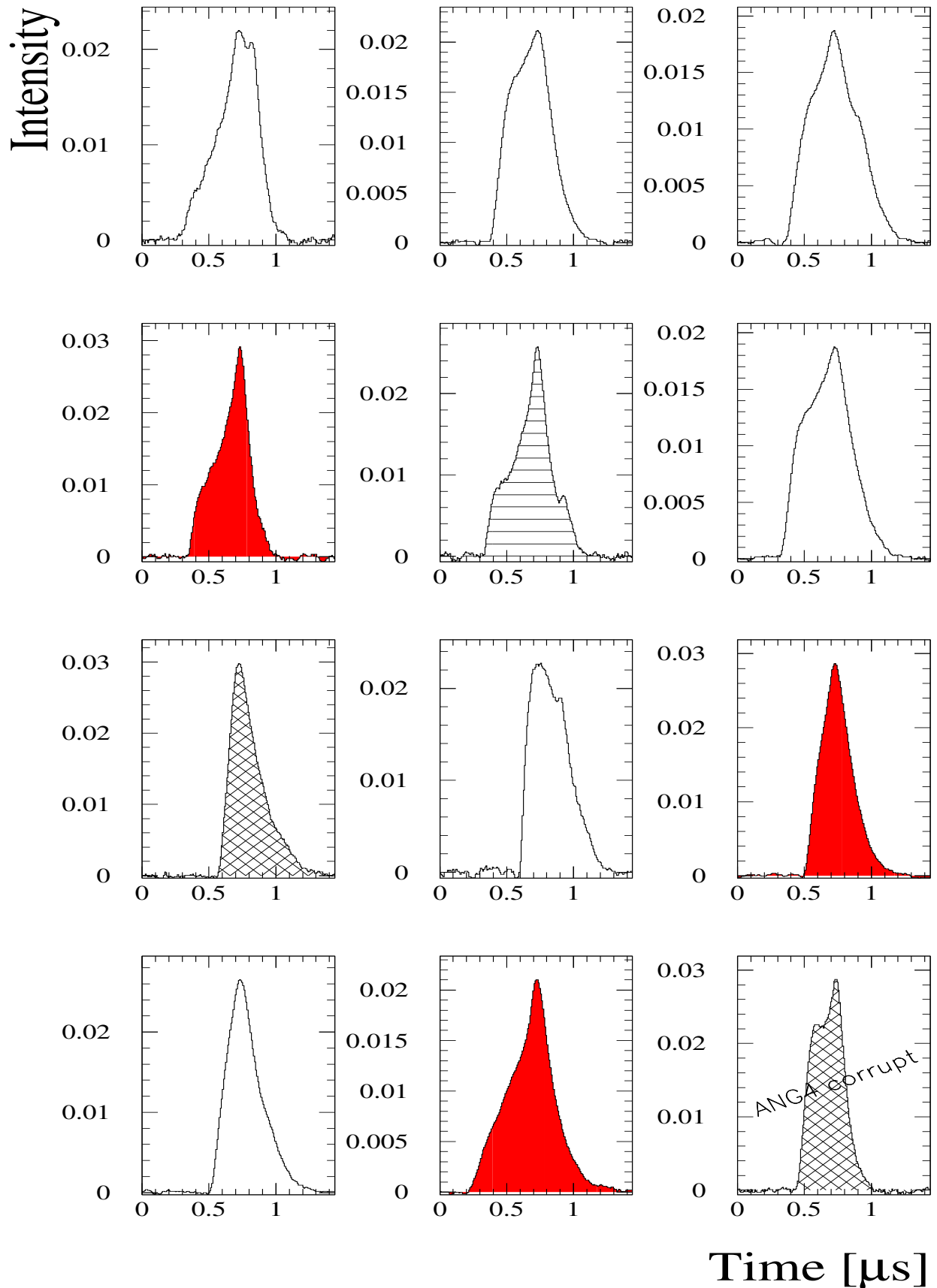
Figure 7.10: Candidates 13-24. Open histograms correspond to pulses classified as MSE by all three methods. Striped histograms have been rated as SSE by one, cross striped histograms by two of the three methods. Dark shaded histograms have been classified as SSE by all three methods.
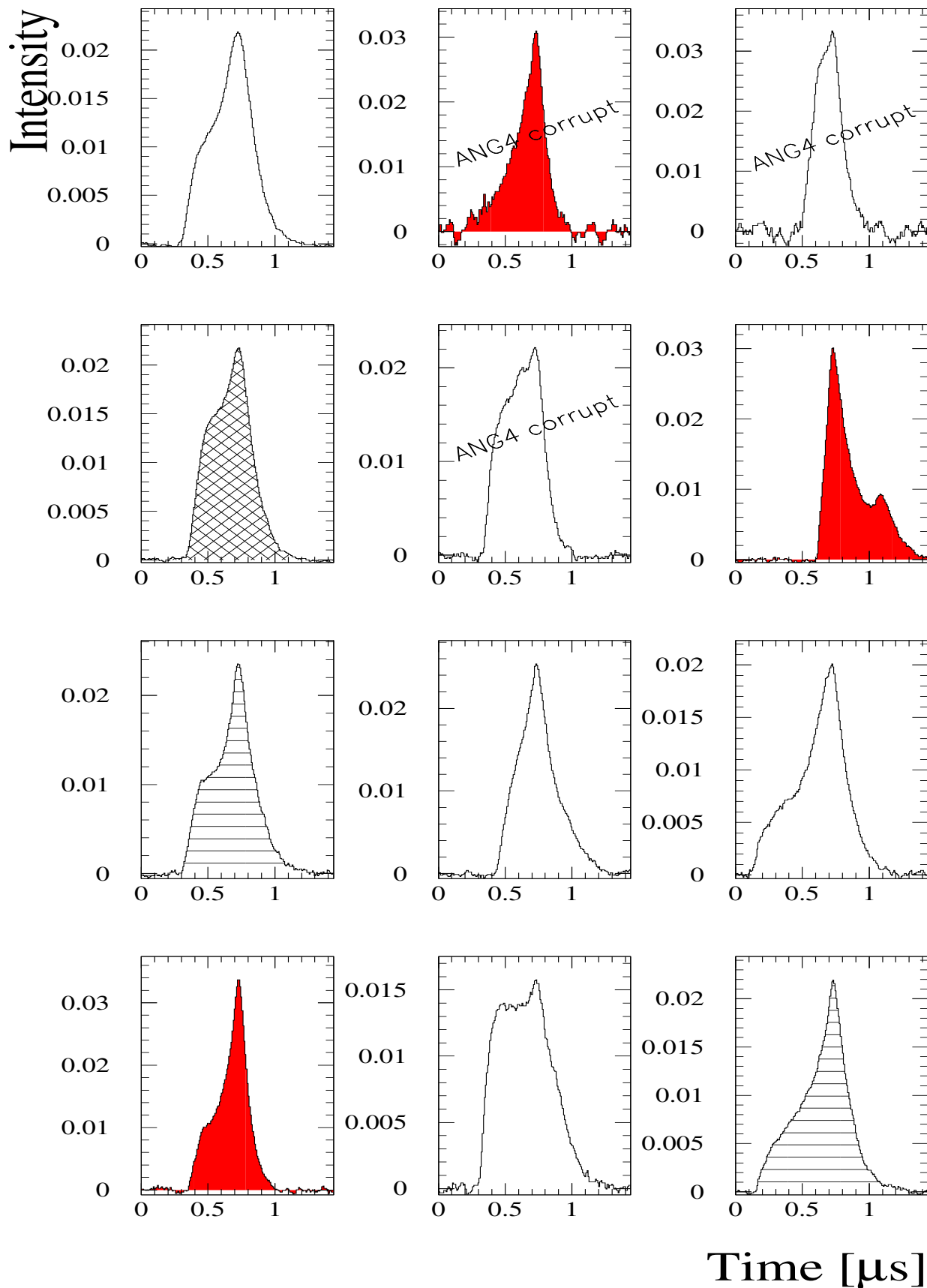
Figure 7.11: Candidates 25-36. Open histograms correspond to pulses classified as MSE by all three methods. Striped histograms have been rated as SSE by one, cross striped histograms by two of the three methods. Dark shaded histograms have been classified as SSE by all three methods.
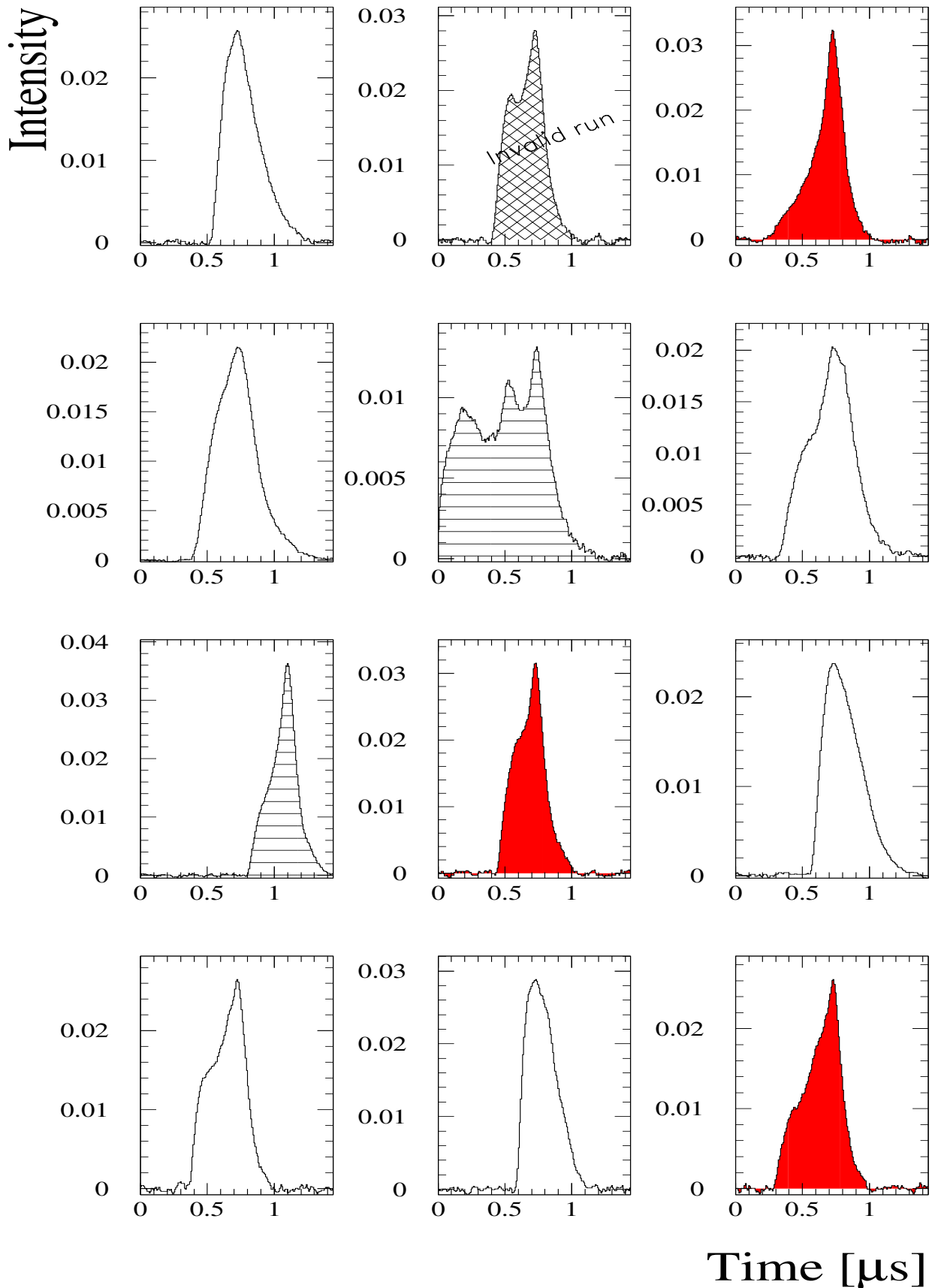
Figure 7.12: Candidates 37-48. Open histograms correspond to pulses classified as MSE by all three methods. Striped histograms have been rated as SSE by one, cross striped histograms by two of the three methods. Dark shaded histograms have been classified as SSE by all three methods.
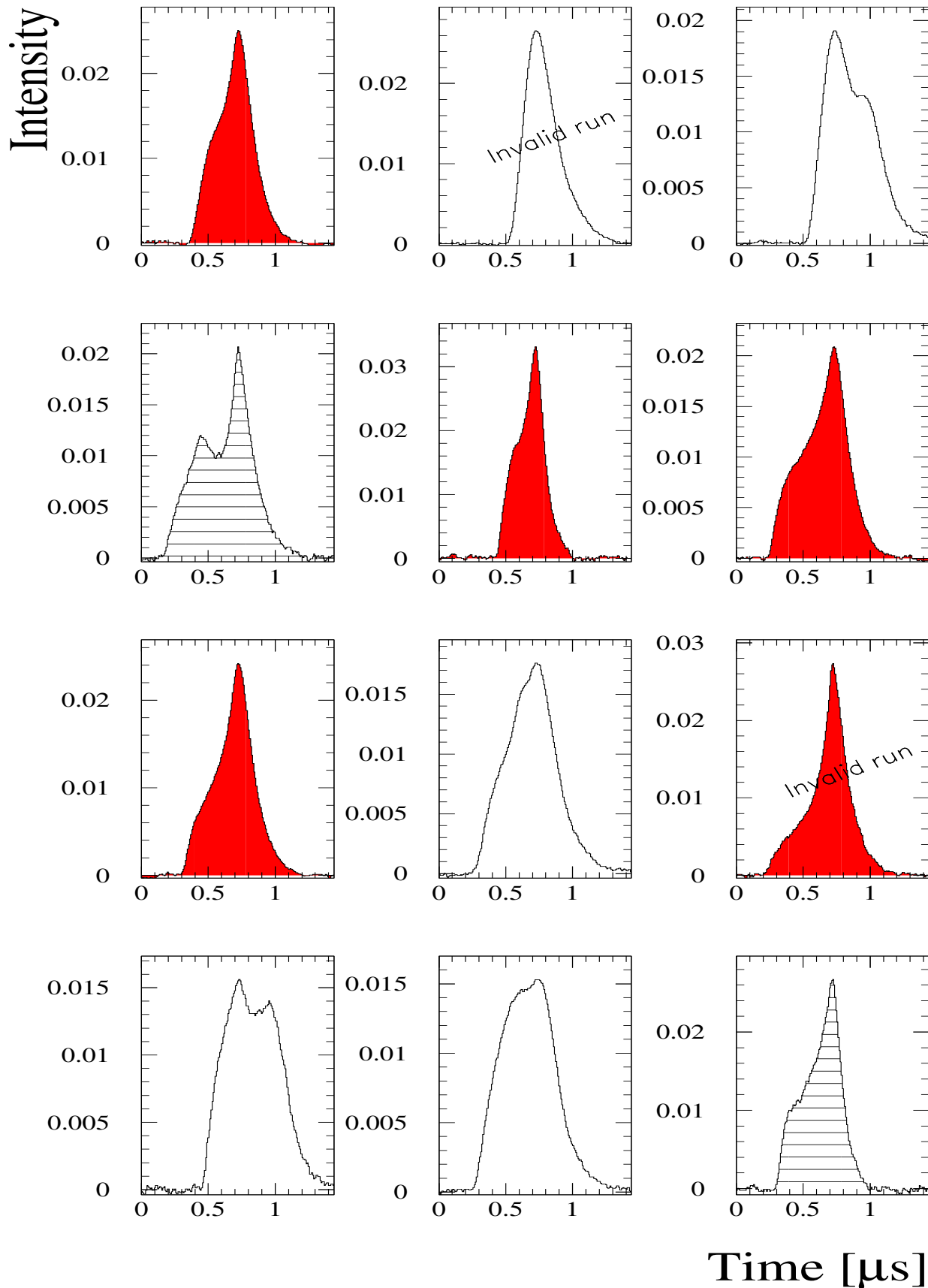
Figure 7.13: Candidates 49-60. Open histograms correspond to pulses classified as MSE by all three methods. Striped histograms have been rated as SSE by one, cross striped histograms by two of the three methods. Dark shaded histograms have been classified as SSE by all three methods.
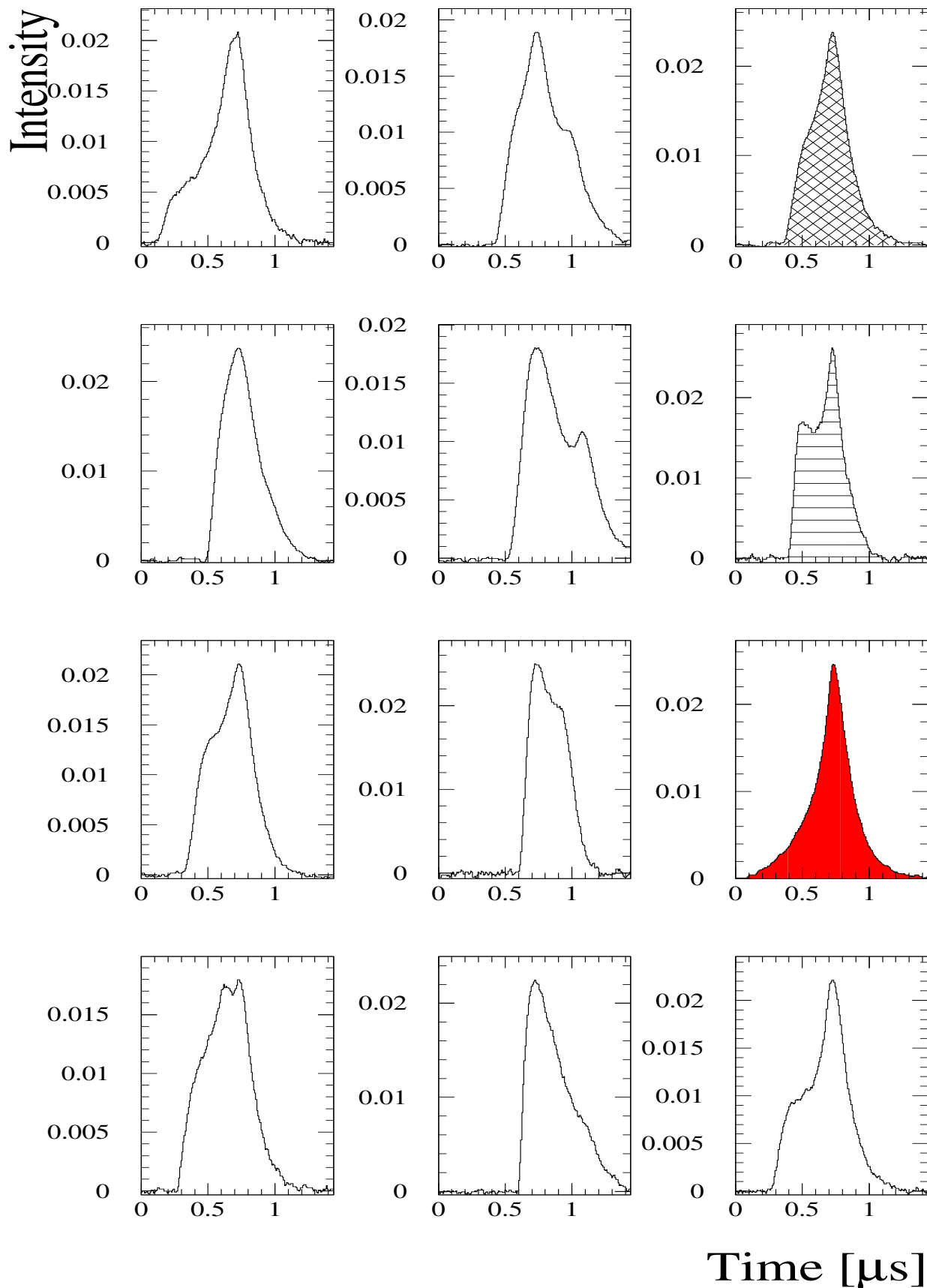
Figure 7.14: Candidates 61-72. Open histograms correspond to pulses classified as MSE by all three methods. Striped histograms have been rated as SSE by one, cross striped histograms by two of the three methods. Dark shaded histograms have been classified as SSE by all three methods.

Figure 7.15: Candidates 73-76. Open histograms correspond to pulses classified as MSE by all three methods. Striped histograms have been rated as SSE by one, cross striped histograms by two of the three methods. Dark shaded histograms have been classified as SSE by all three methods.
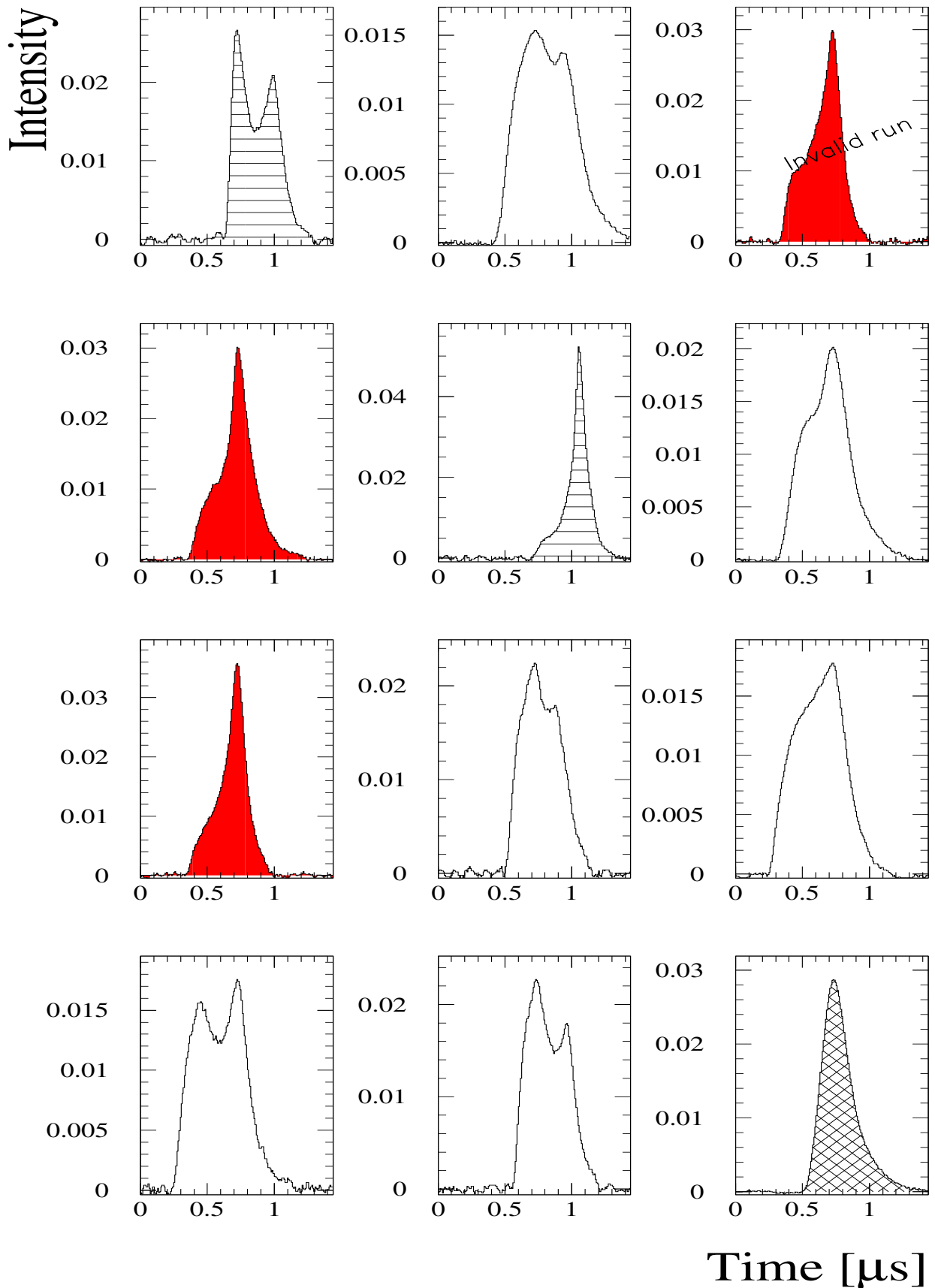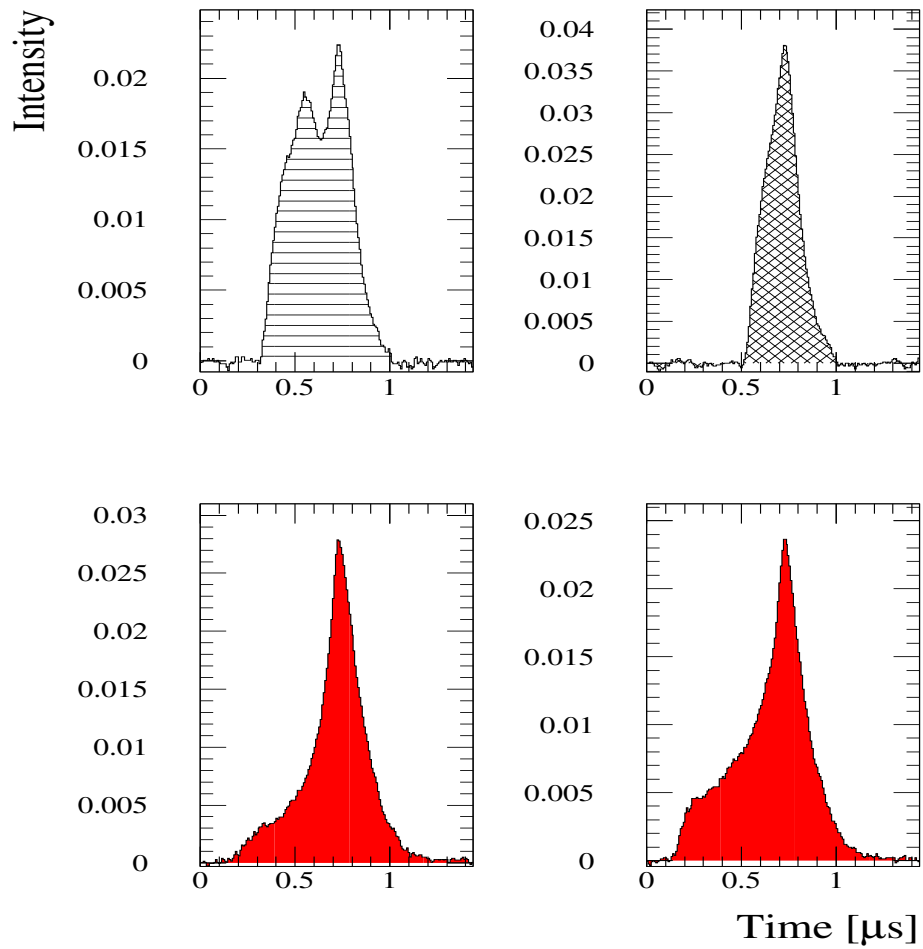
#	Run Nr.	Time in days days since 1st run	Detec- tor	Energy [keV]	EoI (compare to tab. 7.1)	Result of Neural Network#1	Result Neural Network#2	Result of old method (see tab. 7.2)	Classi- fica- tion
1	15	2.58459	ANG5	2038.7	0.18635	1	1	8.255	MSE
2	45	31.9932	ANG2	2036.7	0.12578	1	1	11.262	MSE
3	49	37.1965	ANG3	2036.8	0.13339	0.033	0.0806	8.058	2/3
4	56	44.9467	ANG3	2041.9	0.13386	1	1	14.636	MSE
5	57	48.5207	ANG2	2042.4	0.12767	1	1	11.969	MSE
6	71	61.6492	ANG4	2035.8	0.24396	0.698	0.978	4.1238	1/3
7	108	94.7724	ANG3	2035.7	0.13398	0.481	0.687	9.8488	MSE
8	124	111.009	ANG4	2042.5	0.2468	0.999	1	7.0475	MSE
9	132	118.131	ANG2	2036.2	0.12313	8.58e-05	0.000174	5.9492	**SSE**
10	233	208.741	ANG5	2039	0.18885	1	1	9.5199	MSE
11	246	223.037	ANG5	2037.8	0.19041	1	1	5.9771	MSE
12	301	266.423	ANG5	2033.6	0.18727	0.924	0.976	7.9353	MSE
13	388	331.476	ANG4	2034	0.23875	0.999	1	5.8861	MSE
14	471	390.498	ANG3	2038.3	0.13327	0.684	0.812	11.217	MSE
15	477	393.699	ANG3	2035.2	0.13348	1	1	11.535	MSE
16	543	444.166	ANG4	2034.1	0.24644	0.269	0.0255	4.5575	**SSE**
17	642	516.525	ANG4	2039.5	0.23891	0.657	0.988	4.7006	1/3
18	663	531.682	ANG3	2042	0.13368	0.998	1	11.56	MSE
19	670	535.736	ANG5	2037.9	0.18962	0.139	0.257	7.3612	2/3
20	673	538.158	ANG4	2041.5	0.23711	1	1	6.1437	MSE
	688	547.274	ANG1	2033.9	-	-	-	-	-
21	699	556.546	ANG3	2034.3	0.13342	0.00222	0.0136	8.6236	**SSE**
22	719	573.244	ANG3	2037.3	0.13252	0.99	0.999	10.56	MSE
23	735	586.126	ANG2	2038.6	0.12485	0.0257	0.133	7.9641	**SSE**
24 *	743	591.885	ANG4	2033.4	0.24591	0.344	0.0465	4.9934	2/3
25	749	595.56	ANG3	2034.2	0.13473	0.42	0.649	11.55	MSE
26 *	759	602.072	ANG4	2033.5	0.80088	0.0707	0.000169	3.8566	**SSE**
27 *	852	665.637	ANG4	2042.2	0.74423	0.477	0.773	5.0432	MSE
28	937	720.241	ANG3	2039	0.13351	0.104	0.179	9.3389	2/3
29 *	991	761.564	ANG4	2034.5	0.25309	0.831	0.993	6.5618	MSE
30	1036	797.885	ANG5	2039	0.19237	3.53e-07	6.69e-06	3.6435	**SSE**
31	1067	822.169	ANG5	2035.6	0.18986	0.467	0.818	5.8314	1/3
32	1084	830.166	ANG5	2034.9	0.19195	1	1	5.5055	MSE
33	1100	846.614	ANG5	2038.6	0.1901	1	1	6.9843	MSE
34	1125	866.565	ANG4	2042.1	0.24536	0.044	6.3e-06	3.7047	**SSE**
35	1156	891.888	ANG5	2034.9	0.19032	1	1	8.9428	MSE
36	1193	921.576	ANG5	2039.4	0.18881	0.97	0.991	5.2249	1/3
37	1201	929.045	ANG5	2041.4	0.18904	1	1	10.401	MSE
38 *	1269	982.102	ANG4	2034.6	0.24783	0.385	0.162	4.7651	2/3
39	1271	984.41	ANG4	2038.1	0.24772	0.152	0.00055	4.3873	**SSE**

Table 7.4: List of candidate events for $0\nu\beta\beta$ recorded with the Heidelberg–Moscow $\beta\beta$ experiment. All data since the change of the data acquisition for PSA is considered. The marked runs * were ommited in the data analysis since the detector ANG4 had an instable TFA in these runs. Listed is the number of the candidate, the run number in which the candidate occured, the time elapsed since the beginning of measurement with pulse recording in days, the detector in which the pulse occured, the exact energy of the event, the Energy over Integral (EoI) value of the pulse, the results from the three methods used for classification and the classification reult from the three methods combined: SSE represents pulses uniformly rated as SSE by all methods, 2/3 means classification as SSE by two, 1/3 by one of the three methods. MSE means uniform classification as MSE by all methods.

#	Run Nr.	Time in days days since 1st run	Detec-tor	Energy [keV]	EoI (compare to tab. 7.1)	Result of Neural Network#1	Result Neural Network#2	Result of old method (see tab. 7.2)	Classi-fica-tion
40	1305	1014.11	ANG2	2041.5	0.12776	0.773	0.967	15.472	MSE
41	1314	1020.78	ANG5	2037.4	0.19088	1	1	5.2304	1/3
42	1329	1030.98	ANG5	2034.1	0.18821	1	1	9.6895	MSE
43	1338	1037.3	ANG2	2042.5	0.15021	1	1	1.0772	1/3
44	1378	1071.29	ANG4	2042.6	0.24646	0.2	0.00391	4.1679	**SSE**
45	1416	1100.46	ANG3	2037.5	0.13261	0.992	1	11.771	MSE
46	1429	1104.53	ANG4	2041.3	0.24552	0.479	0.494	5.0899	MSE
47	1432	1113.67	ANG4	2042.3	0.24503	0.999	1	6.321	MSE
48	1465	1139.38	ANG4	2038.8	0.24316	0.348	0.137	4.3468	**SSE**
	1483	1155.67	ANG1	2038.1	-	-	-	-	-
	1507	1176.65	ANG1	2043	-	-	-	-	-
49	1513	1181.11	ANG3	2038.3	0.13373	0.00434	0.00503	7.669	**SSE**
50 *	1519	1185.4	ANG2	2034	0.12861	0.97	0.988	12.399	MSE
51	1531	1195.53	ANG2	2037.4	0.12831	1	1	14.002	MSE
52	1545	1205.55	ANG5	2039.7	0.1907	0.723	0.929	4.2684	1/3
	1577	1232.37	ANG1	2036.3	-	-	-	-	-
53	1592	1244.24	ANG4	2039.8	0.24208	0.111	0.000175	4.4134	**SSE**
54	1610	1259	ANG3	2041.9	0.1333	0.108	0.262	8.3003	**SSE**
55	1627	1271.39	ANG3	2034.3	0.13697	0.00835	0.021	7.8518	**SSE**
56	1646	1288.61	ANG2	2042.4	0.12781	1	1	17.466	MSE
57	1650	1290.49	ANG5	2039.9	0.19018	2.28e-05	0.000185	4.2485	**SSE**
58 *	1682	1315.87	ANG5	2038	0.19002	1	1	11.426	MSE
59	1761	1376.37	ANG2	2042.4	0.12778	1	1	22.293	MSE
60	1762	1376.97	ANG4	2037.6	0.2471	0.41	0.181	4.5387	1/3
61	1762	1377	ANG4	2034.5	0.24955	0.459	0.999	2.8347	1/3
62	1762	1377.13	ANG2	2034.4	0.12894	1	1	16.288	MSE
63 *	1764	1379.52	ANG4	2035.9	0.24452	0.157	0.00206	4.2385	**SSE**
64	1787	1396.78	ANG5	2036.2	0.19096	2.5e-09	2.85e-08	3.9238	**SSE**
	1832	1430.9	ANG1	2038.1	-	-	-	-	-
65	1852	1444.99	ANG5	2040.4	0.22635	1	1	3.977	1/3
66	1862	1453.65	ANG2	2036.1	0.12874	0.526	0.864	12.842	MSE
67	1979	1553.7	ANG4	2033.7	0.24638	0.0275	3.12e-07	3.7932	**SSE**
68	1994	1564.5	ANG4	2033.1	0.24775	1	1	9.1118	MSE
69	2024	1587.7	ANG3	2038.4	0.13547	0.982	0.995	10.053	MSE
70	2035	1597.3	ANG4	2038.3	0.25151	0.931	1	6.1817	MSE
71	2041	1599.87	ANG4	2038.7	0.24844	1	1	5.7572	MSE
72	2094	1642.91	ANG2	2037.4	0.12819	0.0178	0.00841	10.73	2/3
73	2100	1647.38	ANG4	2040.1	0.25038	0.676	0.827	4.3178	1/3
74	2133	1677.15	ANG4	2039.9	0.25225	0.177	0.000228	5.2628	2/3
75	2152	1690.02	ANG5	2042.5	0.1954	1.19e-05	3.83e-05	4.1947	**SSE**
76	2178	1712.59	ANG5	2033	0.19672	2.23e-05	0.00015	4.7629	**SSE**

Table 7.5: Like table 7.4. The marked runs were omitted due to high trigger rates in one or more of the detectors.

Chapter 8

Results from the HDMS experiment

The Heidelberg Dark Matter Search (HDMS) is an experiment designed for the search for WIMP dark matter [Bau98a]. It is using a special configuration to efficiently reduce the background in the low energy region below 100 keV.

In this chapter the latest results from this experiment are discussed. The performance of the prototype detector which was running from March 1998 until July 1999 in the Gran Sasso underground laboratory is summarized.

The final setup started taking data in Gran Sasso in August 2000. A first spectrum from 18.5 days of measurement is presented and discussed.
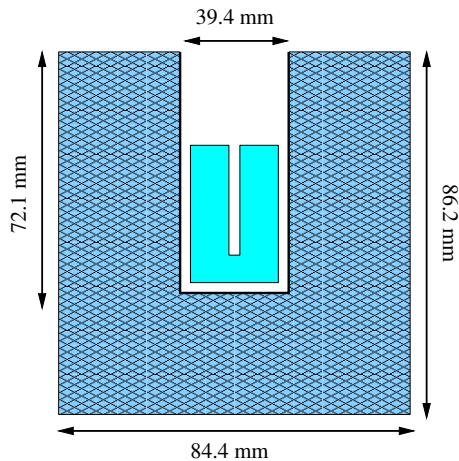

Figure 8.1: schematic view of the HDMS detector configuration. All events which are seen in both inner and outer detector can be considered as background events, not resulting from a WIMP-nucleon recoil.

8.1   Description of the experiment

In direct detection experiments looking for WIMPs one of the main goals is the reduction of background events since the sensitivity of experiments roughly

Figure 8.2: The HDMS detector during the installation in its copper-lead shield in the Gran Sasso underground laboratory.

scales with the obtained background level.

The Heidelberg-Dark-Matter-Search experiment (HDMS) uses the idea first proposed by Petry [Bau97, Bau98a] to operate two HPGe-detectors in a special configuration (see figure 8.1). A small detector is placed inside a bigger well type detector. The outer HPGe crystal acts both, as an active and as a passive shield: If an event is detected within both, inner and outer detector, it can be considered as a background event since for WIMPs it is extremely unlikely to scatter twice within such a short distance. Simulations have shown that for an optimal geometry a reduction in background by up to a factor of 20 can be achieved for the inner detector [Bau98a]. Furthermore the outer detector serves as a passive shield against external radioactivity for the inner detector. The design has the advantage that only extremely radio-pure material is in the direct vicinity of the inner detector since HPGe is one of the cleanest materials with respect to radiopurity that can presently be produced.

8.2 The prototype detector

A prototype detector with the mentioned special design was built by EG&G Ortec. Three of the four contacts of the detector were unfortunately soldered, thus resulting in radioactively contaminated material being close to the HPGe-crystals. The FETs which are the first preamplifier elements were placed 20 cm away from the crystal holder system being already outside the first 10 cm copper shield. This reduces the influence of the FET impurities onto the measurement to a negligible level. Both inner and outer crystals were made out of natural zone refined high purity germanium. The most important properties of the detector are shown in table 8.1.

The electronic data acquisition system allows to take data in calibration mode, where only the energy spectrum of the two detectors is recorded, and in list mode, where the time information and the pulse shape for each event is saved [Bau99]. The energy spectrum is recorded using 13 bit MPI ADCs. The dead time of $200\mu s$ without pulse shape recording and $\sim$200ms with the recording of pulse shapes is negligible for typical event rates of less than 0.01

Property	Inner Detector	Outer Detector
Crystal Type	p–type	n–type
Mass [g]	202	2111
Active Volume [cm^3]	37	383
Crystal diameter [mm]	35.2	84.4
Crystal length [mm]	40.3	86.2
Operation Bias [V]	+2500	-1500
Energy resolution FWHM (1332 keV) [keV]	1.87	4.45
Energy threshold [keV]	2.5	7.5

Table 8.1:
Technical data of the prototype detector of the HDMS experiment (from [Ram98a]).

Hz. For a detailed description of the electronic and the data acquisition see [Ram98a, Bau99].

8.2.1   The anti-coincidence and the crosstalk

Due to the special concentric design, the spatial separation between the two detectors is very small. This gives rise to pick up signals. If one of the detectors sees an event, a cross talk signal is induced in the other one.

Recording spectra of calibration sources with the list mode allows to visualize this pick up signal shown in figure 8.6. The anti-coincidence cut between the two detectors to recognize multiple scattered ckground events can only be applied, if the cross talk is eliminated. This cut is made by defining all events as background events, in which an energy deposition is seen in both detectors above the energy threshold of the proper detector. If however the correction for the pick up signal is not done, many events which do not correspond to energy depostion inside one of the detectors (lying on the zero energy axis) would be mistaken as mutiple scattered events and thus as background.

It was shown that the cross talk is linear with energy and stable over time and can be therefore corrected for off-line [Ram98a]. The slopes of the zero energy axes are denoted with k_{io} and k_{oi}. The pickup of the detectors is then given by the relation:

$$E_i^p = k_{io} \times E_o \quad and \quad E_o^p = k_{oi} \times E_i, \tag{8.1}$$

where E_i^p and E_o^p are the pickup energy seen in the inner and outer detector, respectively, resulting from a real energy deposition E_o and E_i in the outer and inner detector, respectively.

The true energy deposited inside the detector is given by the relation

$$E_i = \frac{E_i' - k_{io} \times E_o'}{1 - k_{io} \times k_{oi}}, \qquad E_o = \frac{E_o' - k_{oi} \times E_i'}{1 - k_{io} \times k_{oi}}, \tag{8.2}$$

where E_o and E_i are the measured energies of the outer and inner detector, respectively and E_o' and E_i' are the real energy depositions for the outer and the inner detector. The slopes were measured to be [Ram98a]:

$$k_{io} = (3.75 \pm 0.04) \times 10^{-3} \quad and \quad k_{oi} = (1.285 \pm 0.003) \times 10^{-1} \tag{8.3}$$

Property	Inner Detector prototype	Outer Detector prototype	Inner Detector ^{73}Ge	Outer Detector final setup
Threshold	(2.0±0.2)keV	(7.5±0.2)keV	(2.0±0.2)keV	(7.5±0.2)keV
Energy resolution at zero keV extrapol.	(1.06±0.30)keV	(3.04±0.10)keV	(0.76±0.05) keV	(2.82±0.06) keV
at zero keV correction	(0.92±0.01)keV	(3.34±0.01)keV	(0.83±0.01)keV	(2.91±0.04) keV
at 81 keV	(1.15±0.03)keV		(0.95±0.03) keV	
at 344 keV		(3.62±0.03)keV		(3.03±0.03)keV
at 1408 keV		(4.55±0.03)keV		(4.46±0.02)keV

Table 8.2: Energy resolutions for different energies and thresholds of the two detector configurations, prototype setup and final setup.

Once the correction is made, the anti-coincidence can be applied. The suppression factor is about a factor of four for the inner detector in the relevant energy region for WIMP dark matter search (40 keV and 100 keV).

8.2.2 Measurements at Gran Sasso underground laboratory

The HDMS prototype detector was installed at the LNGS in March 1998 and successfully took data for approximately 15 month until July 1999 with a total life time of 362.91 days [Bau99, Maj00b]. A picture of the detector before its installation into the low level shield is shown in figure 8.2.

The inner 10 cm of the shield consists of electro-polished low level copper. The outer 20 cm contain low level Boliden lead. To minimize the neutron influence on the detector, the whole shield is surrounded with 15 cm thick borated polyethylene plates.

Energy calibration of the detectors has been done weekly with standard ^{133}Ba and ^{152}Eu-^{228}Th sources. For this purpose a Teflon hose has been installed into the lead-copper shield. A wire with the sealed source at the end can be introduced through this hose into the detector chamber. The time stability of the energy resolution, threshold and calibration parameters (slope and intercept of energy calibration) has been checked elsewhere [Bau99]. The measured energy resolutions and thresholds of the detectors are listed in Tab. 8.2. They correspond to standard values for detectors of this size.

The individual typical duration of a run was about 23 hours. The experiment was stopped daily and the most important detector parameters like leakage current and mean count rates were checked. No substantial fluctuations were recorded. For a detailed discussion of the time behavior of the prototype see [Bau99].

8.2.3 Results from the prototype detector

After the individual runs were calibrated and corrected for the crosstalk using equation (8.2), they were added to provided sum spectra. From the sum spectrum of the inner detector (after the anti-coincidence cut) the limits on WIMP

Figure 8.3: Spectra of the HDMS detectors after a total measuring time of 362.91 days. Upper two panels: outer detector lower two panels: inner detector (from [Bau99]).

dark matter can be extracted.

The sum spectra

The spectra of the full time measurement for both detectors are shown in figure 8.3. The identified peaks are shown in table 8.3 for the inner detector.

Energy [keV]	Area [Counts]	FWHM [keV]	Isotope
10.37	1803 ± 48	2.00 ± 0.06	^{68}Ga and other X-rays
32.46 ± 0.25	110 ± 16	2.63 ± 0.50	??
46.5	−	−	^{210}Pb
122.06	45 ± 11	1.78 ± 0.50	^{57}Co
136.47	48 ± 17	7.48 ± 4.02	^{57}Co
143.58	45 ± 10	1.417 ± 0.39	^{57}Co
238.63 240.99 241.98	40 ± 12	3.35 ± 1.21	^{212}Pb, ^{224}Ra, ^{214}Pb
511.00	284 ± 18	2.82 ± 0.16	annih.
834.84	35 ± 8	6.46 ± 1.80	^{54}Mn
1115.55	12 ± 5	2.08 ± 0.97	^{65}Zn
1125.22	16 ± 5	2.31 ± 1.33	^{65}Zn
1173.24	28 ± 6	2.22 ± 0.45	^{60}Co
1332.50	20 ± 5	2.25 ± 0.59	^{60}Co
1460.81	15 ± 5	4.18 ± 1.00	^{40}K
1764.49	13 ± 4	7.42 ± 1.93	^{214}Bi

Table 8.3: Peaks identified in the full spectrum of the prototype measurement for the inner detector (from [Sch99])

The most prominent structures in the outer detector mainly result from the U/Th decay chains, primordial ^{40}K and some cosmogenic isotopes. Clearly visible is a smeared out structure at approximately 5 MeV, indicating the presence of a α-contamination within the detector cap.

Although the statistics of the inner detector is lower, some structures can already be identified (see table. 8.3). The most obvious structure is a peak at 10.37 keV resulting from the decay of ^{68}Ge. Also here some peaks resulting from the U/Th decay chains and other cosmogenic isotopes can be identified. Note also the existence of a peak at 46.5 keV indicating the presence of a ^{210}Pb contamination. The structure visible at 32.5 keV is slightly smeared out having a full width of half maximum of 2.0 keV (compare to the energy resolution at 300 keV: 1.15 keV). The origin of this structure could not yet be identified.

After the anti-coincidence cut the count rate of the inner detector undergoes a reduction of a factor of 4.3 in the energy region above 40 keV. The peak at 10.37 keV is, as expected, not affected by the anti-coincidence since the decays of ^{68}Ge take place within the detector itself thus leading to full energy deposition in one detector only. The structure at 32.5 keV does not vanish after the cut either, suggesting that also in this case the peak results from an effect inside the inner detector.
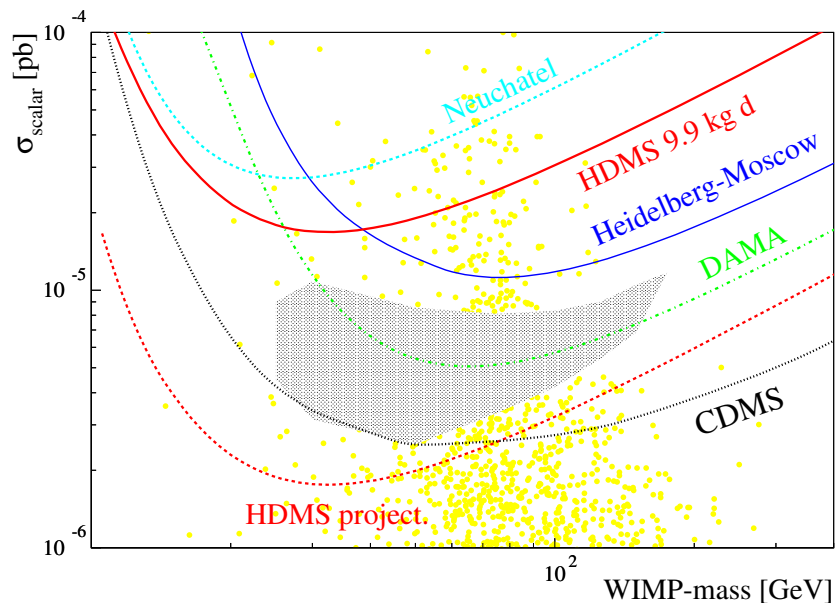
Figure 8.4: Exclusion plot for the presently most sensitive WIMP dark matter direct search experiments. It is visible that for low WIMP masses the HDMS prototype experiment is already now more sensitive than the Heidelberg–Moscow $\beta\beta$ experiment. Also shown are the present limits from the DAMA experiment [Ber98], the CDMS experiment [Abu00] and the Neuchatel experiment [Reu91].

Dark Matter limits

Since many cosmogenic isotopes have half lifes below 300 days, typically the count rate in low level detectors decreases considerably after one year of storage underground.

For this reason only the last 49 days, corresponding to 9.9 kg d of measurement for the inner detector was used for the evaluation of the HDMS prototype data. The procedure of extracting limits on WIMP dark matter from the obtained spectrum follows the method described in chapter 4.1.1. The background index in the energy region between 2 keV and 30 keV was 0.5 counts/(kg keV d). No further background subtraction was applied, i.e. the raw spectrum was used for the analysis.

The resulting upper limit is shown in the exclusion plot in figure 8.4. Already with the prototype detector the limit could be considerably improved with respect to the Heidelberg–Moscow $\beta\beta$ experiment in the WIMP Mass region below 40 GeV. This is due to the fact that an energy threshold of 2 keV could be obtained for this measurements (compare to 9 keV threshold of the Heidelberg–Moscow $\beta\beta$ experiment [Hei98]).

8.3   The final HDMS setup: first results

The detector discussed so far was in many senses only a prototype. The basic goal of this setup was to prove the feasibility of the anti-coincidence technique.
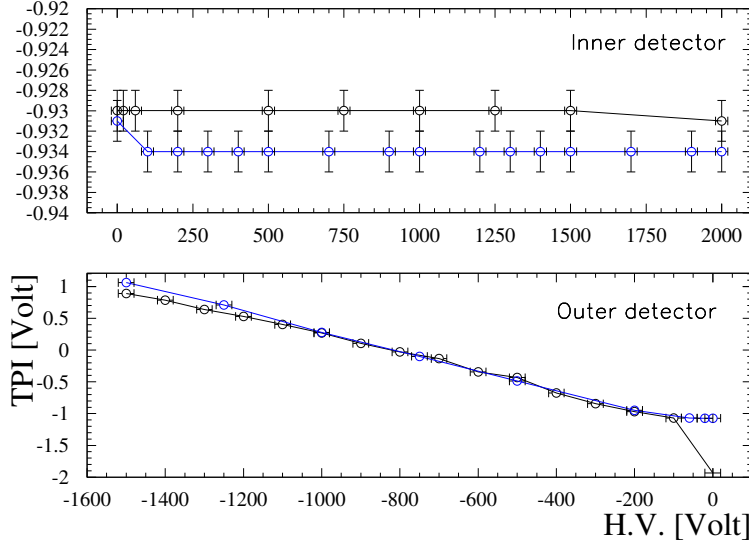
Figure 8.5: The TPI as a function of applied voltage. The black curves denote the measurement at Gran Sasso Underground laboratory, the blue curves correspond to the measurements at the Heidelberg Low Level lab. Upper panel: TPI of inner detector. Lower panel: TPI of outer detector.

For the final setup some important changes have been made. These will be discussed in the following, before discussing the detector performance and first data obtained with the final setup of the HDMS experiment.

8.3.1 Construction of the ^{73}Ge inner crystal

For the construction of the cryostat system of the prototype detector some basic experiences from the Heidelberg–Moscow $\beta\beta$ experiment concerning low level setups were not properly paid attention to.

In low level setups it is essential to avoid any materials of which it is known that they have high radio contamination or of which nothing is known about their radio purity.

As has been shown in considerations and simulations of the background spectrum measured with the HDMS prototype detector [Bau00, Sch99], the main background components seem to result from the following sources:

- Contamination of the natural HPGe inner crystal with cosmogenicaly produced isotopes, especially ^{68}Ge (10.37 keV peak).

- Soldering tin used for contacting of the detectors (α-peak at 5 MeV).

- U/Th contamination of the crystal holder system which was built out of copper provided by EG&G Ortec (now Perkin Elmer).

To further reduce the background of the final setup with respect to the prototype detector, changes were done at the identified background sources.
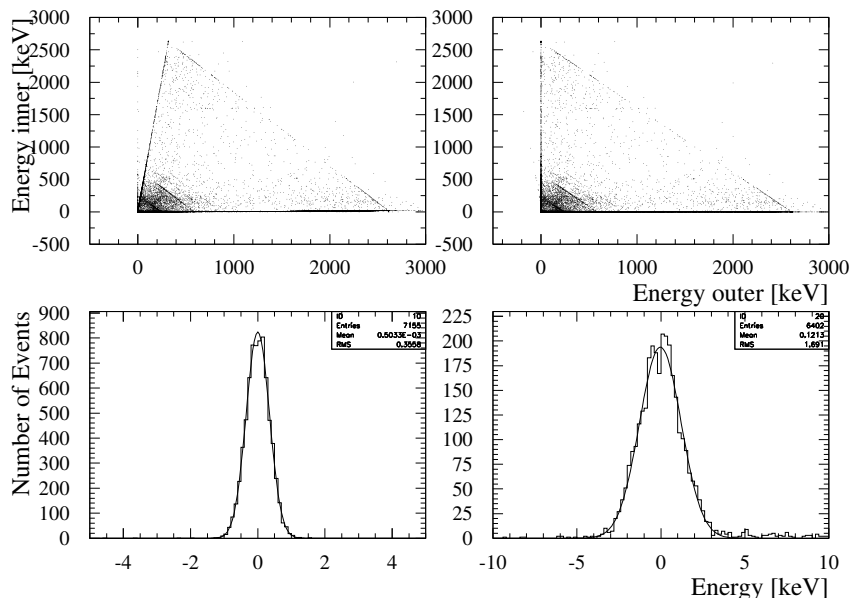
Figure 8.6: Upper panel: Scatter plot of ^{228}Th calibration measurement. Each dot corresponds to one event. The y- and x-axis display the energy deposited in the inner- and outer detector, respectively. Left: Before the correction for pick up signals the zero energy axes have a non-zero slope. Right: After the correction the zero energy axes correspond to the y- and x- axes. Lower panel: Projection of the zero energy axis onto the energy axis of the second detector. For good correction the distribution of the events has to be Gaussian around zero. Left: Projection onto energy axis of the inner detector. The FWHM of the peak is (0.81 ± 0.01) keV. Right: Same as left for the outer detector. The FWHM is (2.91 ± 0.03) keV.

The following modifications were done for the final installation of the HDMS detector with respect to the prototype one:

- The inner detector has been replaced with a crystal grown out of HPGe material enriched in ^{73}Ge. This has the effect that the mother isotope of cosmogenic ^{68}Ge production, ^{70}Ge (^{70}Ge(n,t)^{68}Ge), is deenhanced by up to a factor of 50. Thus the decay of ^{68}Ge will be suppressed by this factor with respect to a natural HPGe crystal.

- The contacts of the HPGe crystals were pinched in order to avoid the use of soldering tin inside the detector cap.

- The crystal holder system has been replaced. The new material is from the same sample as the material used in the Heidelberg–Moscow $\beta\beta$ experiment which is known to be very clean.

This detector system was installed at Perkin Elmer (formerly EG&G Ortec), Oak Ridge, Tennessee, USA, and shipped to Heidelberg, where some test measurements were made, to make sure that the detector performance is good before installation in its final location. Some of the important parameters will be discussed in the next section.
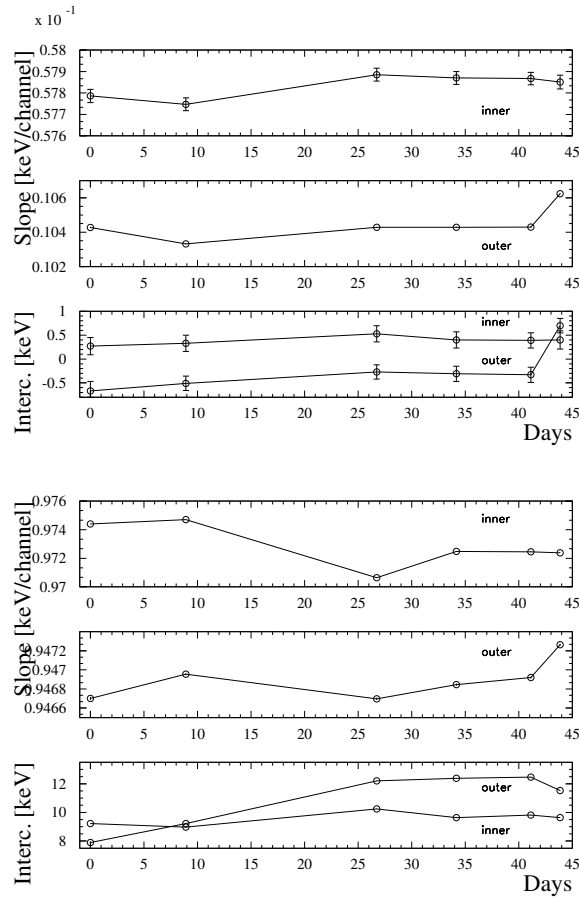
Figure 8.7: Calibration parameters of the two detectors as a function of time. Upper three panels: Low energy calibration, slopes (two upper) and intercept as a function of time. Lower three panels: Same for high energy calibration.

8.3.2 Basic parameters from measurements at Gran Sasso

After checking the stability of the detector system in the Low Level laboratory in Heidelberg, the detector was transported to the Gran Sasso Underground laboratory in Italy. It was installed in its low level surrounding, shielded by 10 cm low activity electro-polished copper followed by an outer subsequent 20 cm Boliden lead layer. A 15 cm thick borated polyethylene shield against neutrons completes the setup.

The behavior of the leakage current as a function of voltage applied to the detectors can be considered as a first stability test of the crystals. In figure 8.5 the so called TPI signal which can be measured at the preamplifier of the detector setup, and which is proportional to the leakage current of the crystal, is shown for both detectors. Especially for the inner detector the stability is remarkable. Up to the saturation voltage there is no noticeable change. The increase of the TPI with increasing voltage is significant for the outer detector, however, this behavior is as expected because the outer detector was not changed during the reconstruction. Therefore a similar TPI curve is expected as it was

measured with the prototype [Ram98a]. The same behavior is seen with the new detector setup as before: The TPI steadily rises with increasing voltage from $\sim$ -1 V at 0 V to $\sim$ +1 V at 1500 V.

The optimal electronic adjustment was investigated. Both detectors proved to have the best energy resolution with a shaping time of $8\mu s$, using ORTEC OR 572 amplifiers. Note that this means a change with respect to the old prototype setup where a $4\mu s$ shaping time was the optimum [Ram98a]. The energy resolutions obtained from calibration measurements for inner and outer detector are shown together with the old reference values in table 8.1. Apparently the performance of both detectors could be slightly improved with respect to the prototype.
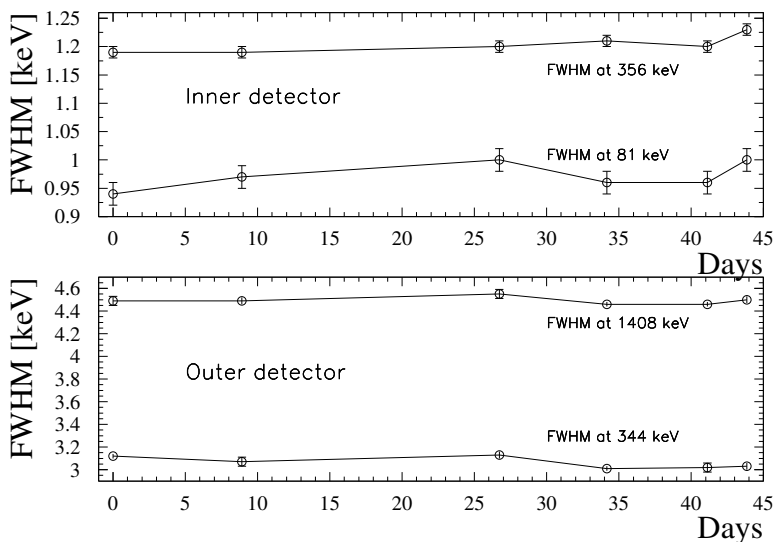

Figure 8.8: Resolution of the two detectors as a function of time.

The bahavior of the pick up signal of the new setup is shown in figure 8.6. The slopes of the zero energy axes from equation (8.2) had to be investigated again. For this reason calibration measurements with a ^{228}Th source have been made using the list mode of the data acquisition program, allowing to get information on every single event registered inside the detector. The slopes were measured to be

$$k_{io} = (6.06 \pm 0.28) \times 10^{-3} \quad and \quad k_{oi} = (1.2107 \pm 0.002) \times 10^{-1}. \qquad (8.4)$$

The slope value for the outer detector has (as expected) hardly changed with respect to the prototype setup. Regarding the slope of the inner detector there was a significant change, however, since the crystal was exchanged, this is nothing peculiar. The value is still on the same order of magnitude as before. Using the slopes k_{io} and k_{oi} the correction for the crosstalk is obtained according to equation (8.2).

Once this is done, it is possible to obtain the zero energy resolution of the detector. The pickup events of a detector follow a Gaussian distribution around

the zero energy axis. Thus, if the correction is good, the projection of all zero events of the first detector onto the energy axis of the second detector yields a peak at 0 keV with proper Gaussian shape. The width of the peak corresponds to the zero energy resolution of the second detector. This is seen for the inner and outer crystals in the lower left and right panel of figure 8.6, respectively. The resolutions are (0.81±0.01) keV for the inner and (2.91±0.03) keV for the outer detector. This is in good agreement with the extrapolated zero energy resolution from the calibration measurement which yields (0.76±0.05) keV and (2.82±0.06) keV for the inner and outer detector, respectively (see also table 8.1). Again it is apparent that an improvement has been achieved for both detectors with respect to the prototype.

The basic parameters denoting a stable detector performance have been checked frequently. Each week an energy calibration is made using standard ^{133}Ba and ^{152}Eu-^{228}Th sources. In figure 8.7 the calibration parameters are shown as a function of time. It is seen that the slopes and intercepts of the energy calibration slightly vary over time. The changes are small (at the order of 1%), corresponding to the expectations from the prototype measurements.

For the low energy ADC of the outer detector there is a significant jump in intercept and slope at the last calibration considered here. This is due to the fact that the amplifier for the low energy ADC has been changed.

The energy resolution remained stable over time. This is seen in figure 8.8 for the 81 keV and 356 keV ^{133}Ba peaks in case of the inner detector and for the 344 keV and 1408 keV peaks of the ^{152}Eu-^{228}Th source.

8.3.3 First background spectrum from the ^{73}Ge crystal

The final detector setup is taking data since August 2000. The data of 18.5 days of life time is discussed here and a first preliminary background spectrum is shown.

In figure 8.9 the time distribution of the low energetic events inside the inner detector is plotted. Clearly visible are time intervals, in which many low energetic events appear, thus significantly increasing the energy threshold. These bursts are due to microphonic events, and not to energy deposition in the detector. The cause for microphonic events is not clear, however, most probably they result from vibrations of the detector crystals, thus inducing a change in capacitance of the system.

In the lower diagram of figure 8.9 the distribution of the number of events in the energy region between 1.8 keV and 40 keV in the inner detector within a 10 minute interval is shown. It is clearly visible that some intervals contain much more events than expected for uncorrelated data since they do not obey the Poisson distribution. Thus it is safe to cut the time intervals where the bursts appeared. All intervals containing more than seven events were omitted from the further data analysis. The reduction of life time due to the bursts makes up only 0.9% of the overall measuring times.

In figures 8.10 and 8.11 the resulting spectra after 18.5 days of measurement corresponding to 3.70 kg d life time (after the cut for the burst) for the inner detector and 39.07 kg d for the outer detector are shown.

In the spectrum of the outer detector there is clear evidence for the peaks listed in table 8.4. The peaks are mainly due to the ^{238}U decay chain. A comparison with the measured spectrum obtained from the prototype reveals
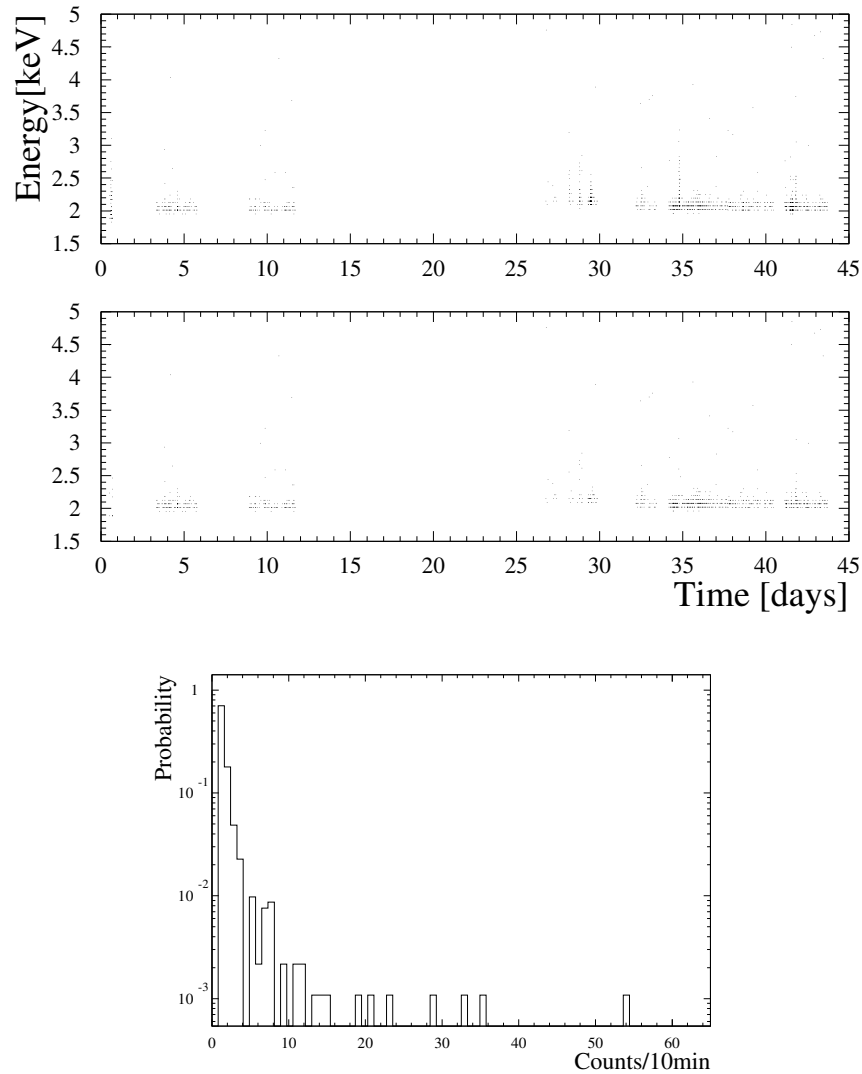
Figure 8.9: Upper two plots: Time distribution of low energetic events in the inner detector. Each dot corresponds to one event Upper panel: raw data of the inner detector. Clearly visible are some bursts at lowest energies, increasing the threshold of the measurement. Lower panel: Time distribution after the cut for the burst. Lower diagram: Probability distribution of number of events within a 10 minute interval. Clearly seen is that towards high count rates the distribution is not poissonian, thus correlated. These time intervals (corresponding to the bursts) can be cut away.

that the location of the impurities most probably must be at different locations since the relative intensities of the peaks do differ significantly in the two spectra. Besides the ^{238}U contamination some cosmogenic and anthropogenic isotopes can be clearly identified: ^{65}Zn and ^{137}Cs. Both are most probably located in the copper of the cryostat system. A distinction on the localization of the contamination can be made in case of ^{65}Zn since the peak position differs for
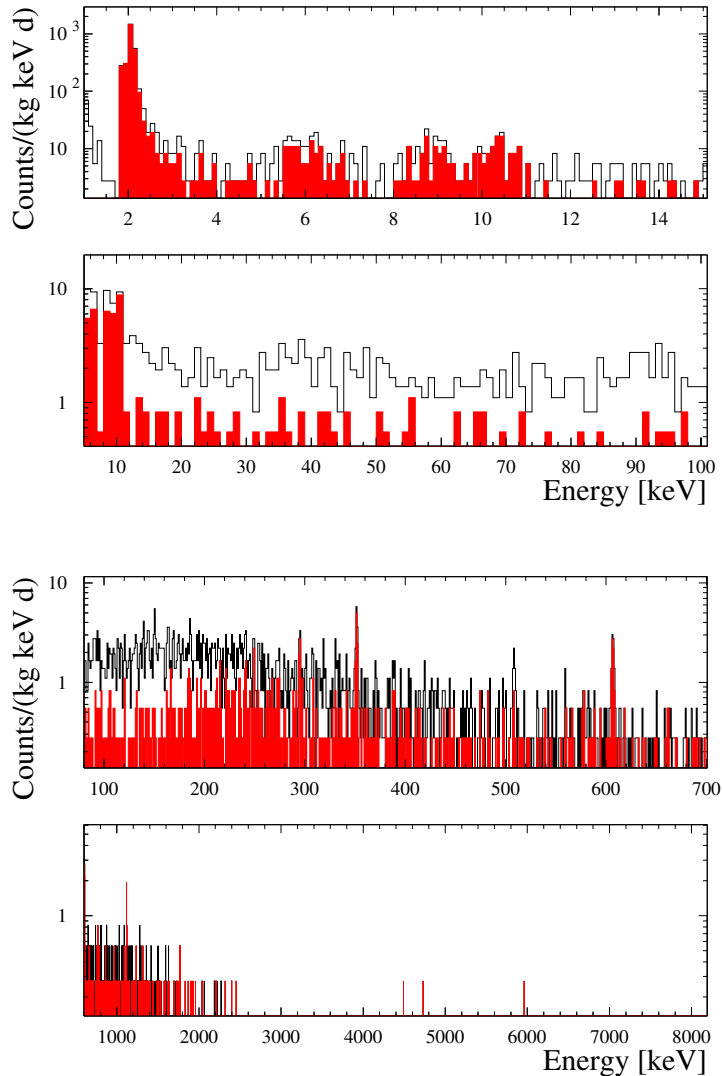
Figure 8.10: Spectrum of the inner detector after 3.70 kg d of measurement. The open histograms corresponds to the overall spectrum, the red filled histogram to the spectrum after the anti-coincidence.

different locations. If the contamination is inside the HPGe crystal itself, besides the gamma resulting from the decay of ^{65}Zn through electron capture with 1115.6 keV, an X-ray particle of 8.9 keV is emitted due to the following cascade. For ^{65}Zn only an external peak can be seen (x-ray is not added to γ with 1115.6 keV).

Despite avoiding the use of soldering tin in the final setup, the α peak in the high energy region around 5 MeV of the outer detector is still present.

Despite the low statistics some structures could already be identified in the inner detector. Clearly visible are peaks at 1120.5 keV, 609.3 keV, 352.0 keV and
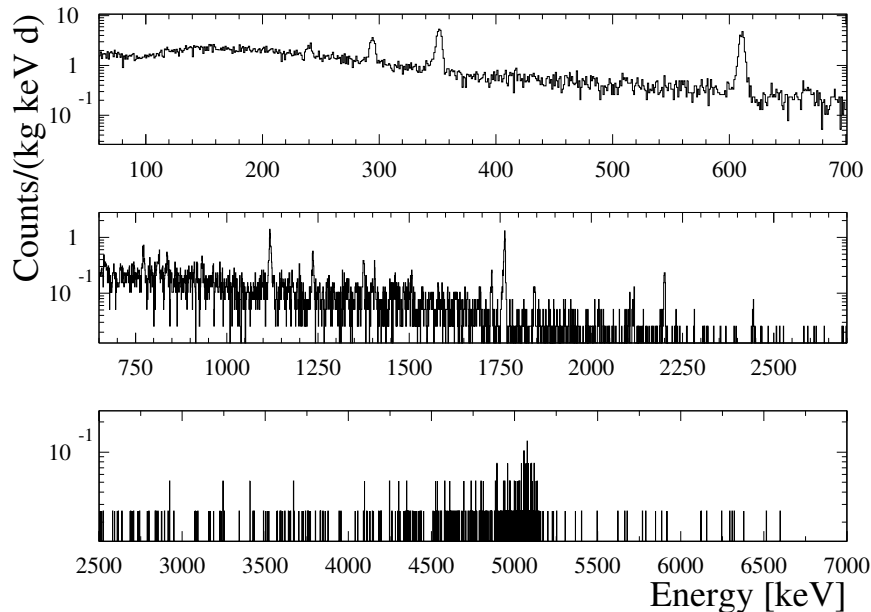
Figure 8.11: Spectrum of the outer detector after 38.72 kg d of measurement.

295.2 keV resulting from the ^{238}U decay chain. Since these peaks could not be seen in the sum spectrum of the prototype detector after its final life time, their origin has to result from the change of the cryostat system. Furthermore there is clear evidence for x-rays from cosmogenic materials: structures around 6 keV, 9 keV and 10.5 keV resulting from the decays of ^{55}Fe and/or ^{54}Mn, ^{65}Zn and ^{68}Ge respectively. All these peaks do not vanish through the anti-coincidence cut as expected from contaminations inside the crystal, as e.g. cosmogenic isotopes.

The overall count rate is comparable to the prototype detector after the same time of measurement for both inner and outer detector [Ram98a]. Thus it follows that the contaminations were most probably not due to the soldering tin and copper holder or that there are new impurities inside the detector cap introduced during reconstruction.

In figure 8.12 the achieved reduction factor on the spectrum of the inner detector through the anti-coincidence effect of the outer detector is shown. At lowest energies (below 15 keV) the reduction does hardly have an effect since this energy region of the spectrum is dominated by cosmogenic activities inside the detector. At energies between 30 keV and 70 keV the spectrum is reduced by a factor of 4.3 which perfectly agrees with the achieved reduction factor of the prototype detector [Bau00].

Already now it can be stated that no reduction of the background with respect to the prototype detector could be achieved. The reasons for this still have to be investigated. Especially the source for the α contamination seen at high energies in the outer detector and the contamination with ^{238}U which appeared in the inner detector after the reconstruction have to be located. Once the lo-

Energy [keV]	Isotope	$T_{1/2}$
238.6	^{214}Pb	
295.1	^{214}Pb	from
351.9	^{214}Pb	^{238}U
609.3	^{214}Bi	decay
1238.1	^{214}Bi	chain
1377.7	^{214}Bi	
1764.5	^{208}Tl	
2204	^{214}Bi	
661.7	^{137}Cs	30.07 yr
1115.6	^{65}Zn	243.9 days

Table 8.4: Identified peaks in the sum spectrum of the outer detector after 18.5 days of measurement.
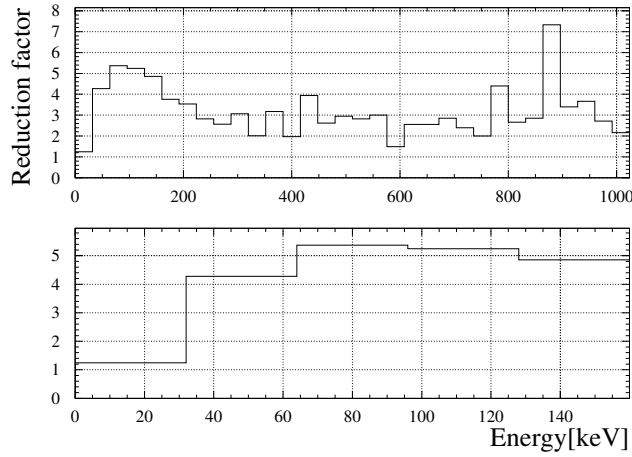

Figure 8.12: Reduction factor of the spectrum after 18.5 days of measurement for the inner detector through the anti-coincidence effect of the outer detector as a function of energy.

cations are known, it could be considered to open the setup again and to clean the detector from these impurities. However, after 18.5 days of measurement it is too early to make predictions on the final sensitivity of the setup. More statistics has to be gathered in order to make safe statements on the reasons for the background.

It is too early at this stage to make reliable projections of the final sensitivity of the final setup of the HDMS experiment. From experience with other detectors it can however be stated that the background index will decrease considerably with time since the typical half lifes of cosmogenic isotopes is around 200-300 days. This was impressively seen with the prototype setup. After one year of storage at the Gran Sasso underground laboratory the background index in the low energy region was reduced by approximately a factor of five with respect to the beginning of the measuremennt.

Chapter 9

The Genius Project

Dark matter search is presently in a very interesting and exciting epoque. The DAMA collaboration claims to see an annual modulation of their experimental spectrum obtained with 100 kg NaI scintillation crystals [Bel00]. The preferred explanation for this modulation is by means of WIMP dark matter since the frequency and phase are as predicted (see chapter 4.1.2).

Already now first experiments are testing the preferred $M_{WIMP} - \sigma_0$ parameter space [Abu00], however, the evidence is not yet confirmed. This somewhat controversial [Ger00, Gai00] result will be tested in the near future searching for the claimed WIMP dark matter signal: the recoil spectrum. There is no means, however, using the present experiments, to check the annual modulation signature independently from the DAMA experiment.

Comparing the sensitivities of the present direct detection WIMP dark matter searches to predictions from minimal supersymmetrical standard models makes clear that, once the DAMA evidence should be disproven, a big effort has to be made in order to be able to cover large parts of the favored parameter space. As visible in figure 9.1 an improvement of sensitivity of at least three orders of magnitudes is needed for experiments aiming at this goal.

Lately the situation has become even more unpleasant since it becomes more and more evident that the favored parameter space stretches down to very low WIMP-Nucleon cross-sections [Nat00, Ell00]. Scatter plots like those shown in figure 9.1 strongly depend on assumptions made by the authors and can thus vary significantly for different references.

These considerations also show that a dramatic increase of sensitivity of direct detection experiments is desired to test at least parts of the parameter space. Since the sensitivity of a WIMP dark matter direct search experiment roughly scales with the background, it is therefore the major goal of future experiments to greatly reduce the background index.

The situation is quite similar regarding neutrinoless double beta decay. The most sensitive experiment, the Heidelberg–Moscow $\beta\beta$ experiment, is close to reaching its final sensitivity. The sensitivity to the effective Majorana neutrino mass increases only with the fourth root of the measuring time, active mass and achieved background level (see equations (4.12) and (3.7)). Therefore, once a certain statistics is reached, it is practically impossible to further increase the sensitivity of the experiment within a reasonable time span.

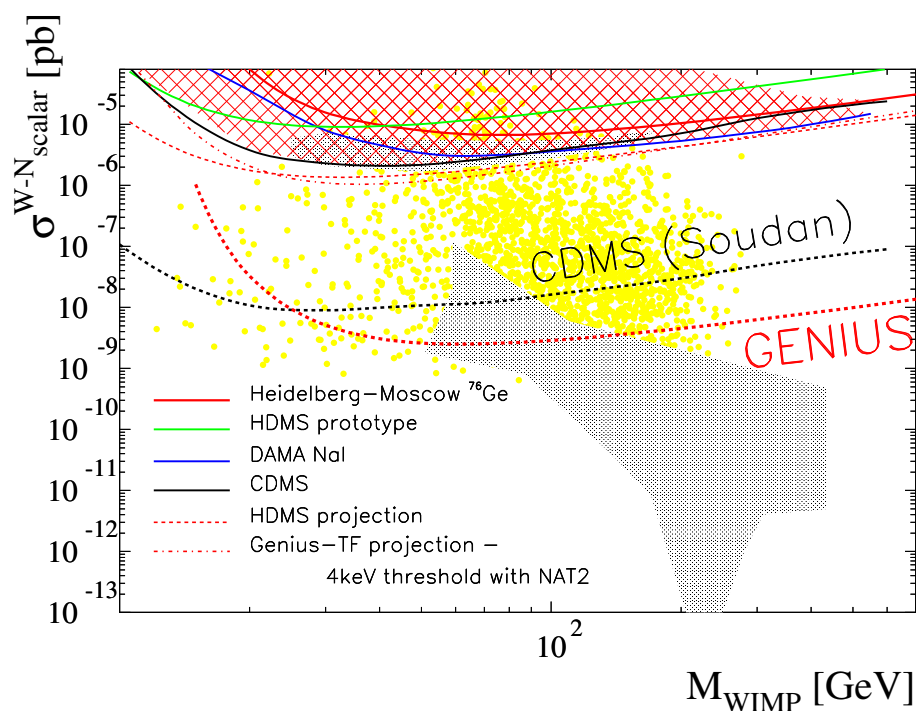As seen in figure 4.2 the best experiments which are presently taking data

Figure 9.1: WIMP-nucleon cross section limits as a function of the WIMP mass. The hatched region denotes the parameter space excluded by the Heidelberg Moscow experiment [Hei98], the DAMA experiment [Ber98] and the CDMS experiment [Abu00]. Shown are also the projected sensitivities of the HDMS experiment and the Genius TF [Kla00d, Maj00c] which will provide data in the near future. Furthermore the expected sensitivities of the CDMS setup in Soudan and of the GENIUS experiment in its dark matter phase is shown. The limits and expected sensitivities are compared to expectations for WIMP-neutralino calculations in the MSSM framework with different assumptions [Ell00, Bed00a].

or are under construction have a maximal sensitivity on the effective Majorana neutrino mass of ~ 0.1 eV. On the other hand it is clear that double beta decay experiments are just now entering a very exciting time since first neutrino mass scenarios can be tested (see chapter 3.3.1 and figure 3.3 therein). Since only neutrinoless double beta decay in connection with neutrino oscillation experiments will be able to get further information on this topic, it is of utmost importance to further increase the sensitivity of future double beta experiments. However, to do so, two requirements have to be fullfilled simultaneously:

- Increase of the target mass of the experiment

- Reduction of background.

In order to achieve a dramatic step forward regarding background reduction, a new experimental technique is needed.

Lately there have been two promising approaches to reach this goal:

- Cryo-detectors have been developed which are able to detect two signals of the WIMP-nuclear recoil phonons and ionization (e.g. the CDMS experiment [Sch00]), or phonons and scintillation (e.g. the CRESST phase 2

experiment [Sei00]) simultaneously. This enables a very effective discrimination between nuclear recoils and electromagnetic interactions.

- Application of standard detection techniques while removing all dangerous contaminations from the direct vicinity of the detectors.

The GENIUS (GErmanium in liquid NItrogen Underground Setup) proposal which is discussed in this chapter uses the second concept. First the basic concept of the project is discussed and it is shown that the new detector technique works. The previous background simulations and calculations are shortly summarized, before presenting some new considerations on the tritium enhancement inside the HPGe crystals during production. Finally it is shown that GENIUS could be built in any underground laboratory with a shielding overburden of more than 2000 mwe.

9.1   The concept of the GENIUS experiment

The GENIUS project is based on the idea to operate 'naked' HPGe crystals directly in liquid nitrogen [Heu95]. The idea is to first prove that this techniques really works and then to use it to remove all dangerous contaminations from the direct vicinity of the crystals. To shield against external radioactivity the liquid nitrogen tank is enlarged [Kla98a]. This has the great advantage that the liquid nitrogen which is very clean with respect to radiopurity due to its production history (fractional distillation), can act simultaneaously as cooling medium and shield against external activities.

The proposed detection technique is based on ionization in HPGe detectors. The crystals would be of p-type. p-type detectors have the advantage that the outer contact is n^+ and the surface dead layer therefore several hundred micrometers. This effectively prevents the detection of α- and β particles which would otherwise dominantely contribute to the background. The ideal working temperature of the p-type detectors is 77 K. The cooling of the HPGe crystals is very efficient since the detectors are in direct thermal contact with the cooling medium liquid nitrogen. The good performance of this detector technique regarding energy resolution and enery threshold is discussed in the next section.

It has been shown before that with this approach a reduction of background by three to four orders of magnitudes can be achieved [Kla98a, Kla98b, Bau98c, Kla99a]. The conceptual design of the experiment is depicted in figure 9.2.

Besides a dramatic decrease of background, the concept has the great advantage that the experiment can house large amounts of detectors, thus increasing the target mass to 100 kg of natural germanium detectors for the first step (dark matter search) and up to 1 ton of enriched ^{76}Ge for the full scale double beta decay experiment. This would already in the first step allow to search with high significance for the annual modulation effect discussed in chapter 4.1.2.

The experimental site could be the Gran Sasso underground laboratory with a shielding overburden of $\sim$ 3800 mwe.

9.2   Technical Studies

Several studies have been carried out to demonstrate the possibility of operating 'naked' High-purity Germanium-Detectors in liquid nitrogen [Kla99a, Kla98b,
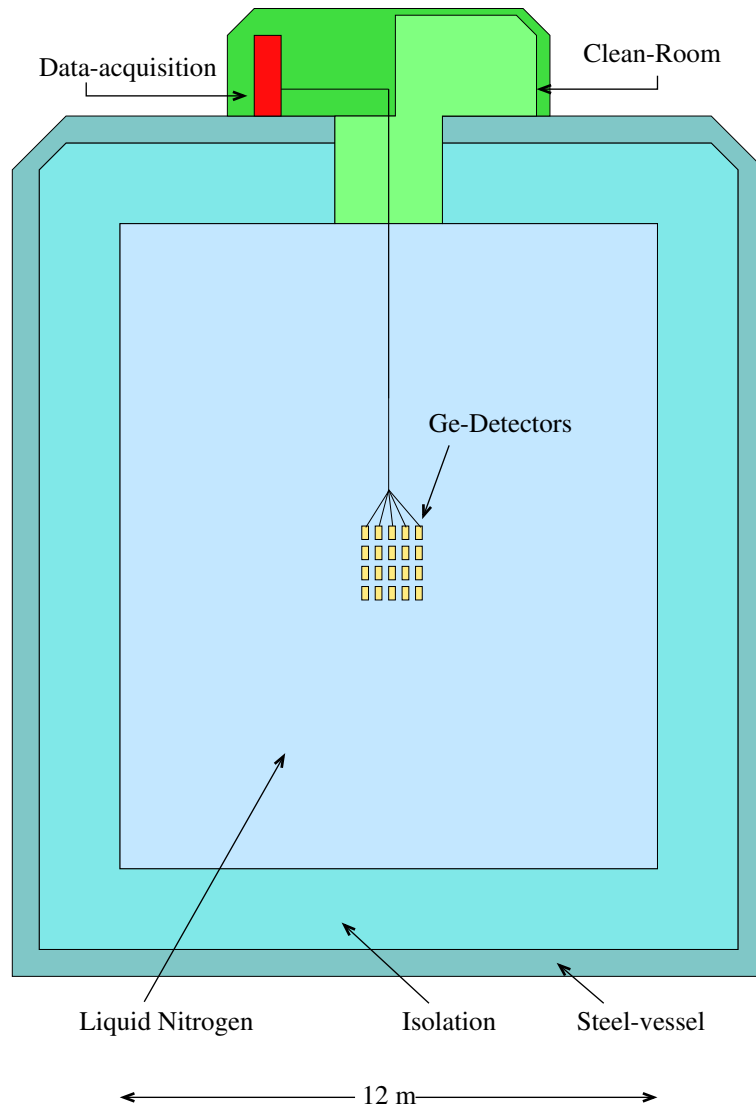
Figure 9.2: Schematic view of the GENIUS project. An array of 100 kg natural HPGe detectors for the WIMP dark matter search (first step) or 1 t of enriched ^{76}Ge for the double beta decay search (final setup) is hanging on a support structure in the middle of the tank immersed in liquid nitrogen. The size of the nitrogen shield would be 12 meters in diameter at least. On top of the tank a special low level clean room and the room for the electronics and data acquisition will be placed.

Bau98c]. It was shown that the concept of this new detector design works well and is equivalent in detector performance compared with conventionally operated High-Purity Germanium-Detectors.

In this section the latest results of detector development using less than five grams of material for contacting the crystal is presented [Maj00a].

In the previous studies [Kla99a] the contacts were established by firmly pressing the high-voltage and signal cables onto the crystals with the help of polyethylene plates thus requiring a non-negligible amount of material in the
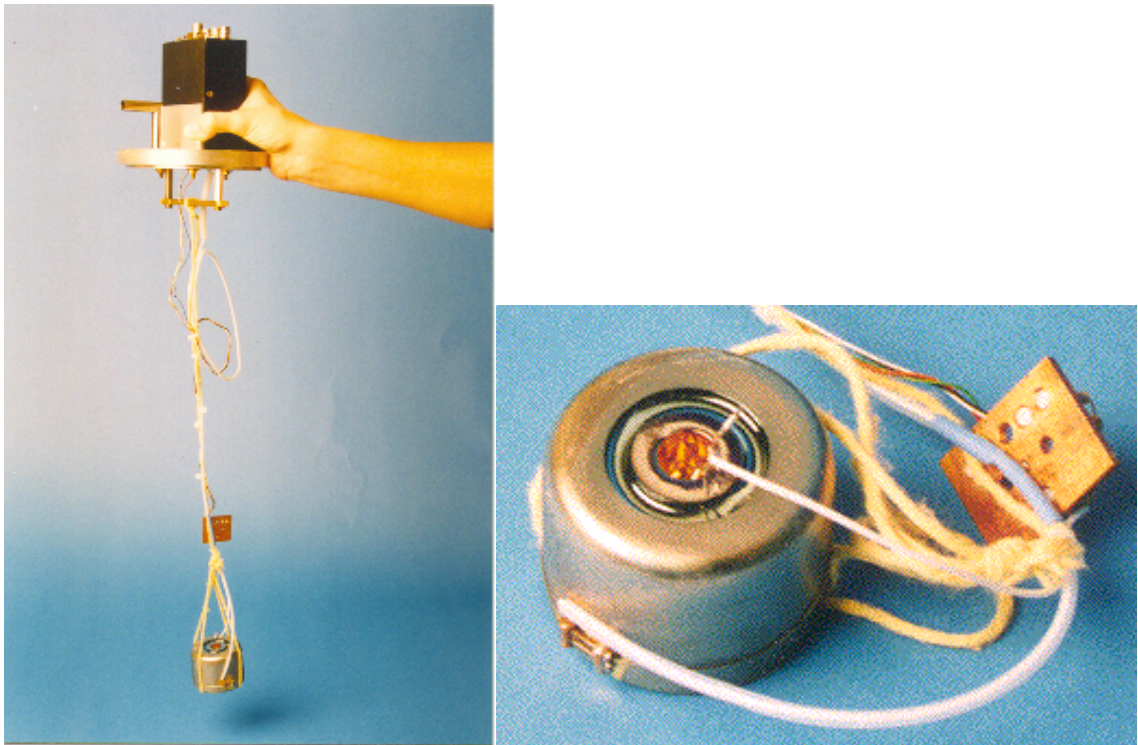
Figure 9.3: Left: Picture of the detector system including the complete FET circuit (rectangular plate above the knot, first preamplifier element) and the preamplifier (black box). The HPGe-crystal is hanging on a Kevlar rope. Right: The naked HPGe-crystal. The FET and both contacts are visible: the high-voltage contact is underneath the two screws on the left side of the crystal. The signal contact is obtained by a spring loaded steel wire placed inside the well.

direct vicinity of the crystal. The main goal of this study was to further minimize the amount of material. For the high-voltage contact a thin steel ring was used, adjustable by two small screws to the exact circumference of the crystal. A thin gold layer was placed between the bolts holding the screws on the steel ring and the crystal surface providing a contact area for the high-voltage cable. The signal contact is made of a bent elastic steel wire pressed against the inner surface of the well by its spring load. In this way an overall amount of only 3.5 g was needed to provide stable contacts. The crystal was deployed on a Kevlar rope into a 50 l liquid nitrogen dewar (see figure 9.3). For this study the used materials were not specially checked for low-level requirements. It is known that Kevlar is not suitable to be used for low-level applications. An alternative to Kevlar is polyethylene which is commonly used in low-level experiments. As will be shown later, the steel ring does not account for a considerable background rate provided the radiopurity is as good as has been reached by the Borexino Collaboration [BOR98].

The performance of the detector proved to be good despite the fact that a scratch in the outer surface of the crystal (resulting from transport from Belgium to Heidelberg) affected stable operation of the detector at its nominal voltage. figure 9.4 shows a calibration spectrum obtained with ^{133}Ba and ^{241}Am sources.
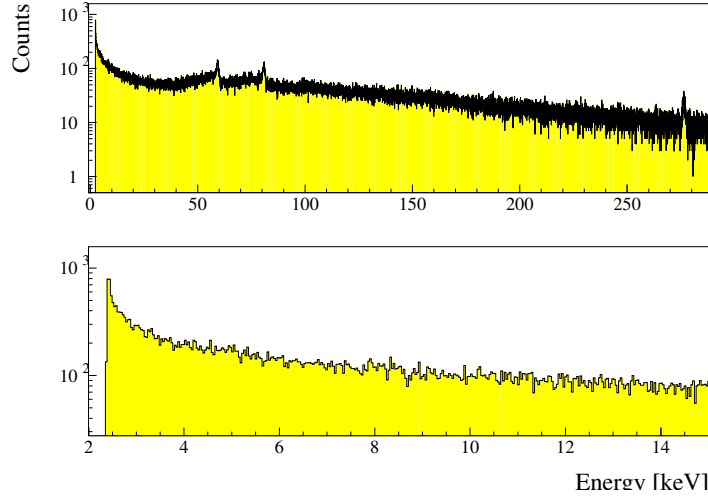
Figure 9.4: A Calibration measurement with the new detector. Upper panel: The whole recorded spectrum. The energy resolution was 1.1 keV at 276keV. Visible are the characteristic peaks at 81.0 keV and 276.4 keV from the ^{133}Ba calibration source and at 59.5 keV from the ^{241}Am source. Note the logarithmic scale of the spectrum. Lower panel: The extrapolated energy threshold of this setup was around 5 keV in this measurement.

The achieved energy resolution of this setup was 1.1 keV at 276 keV. The energy threshold was limited to 5 keV due to the before-mentioned impairment.

This study nicely proves that most of the materials from around the detectors can be abandonned using the new detector technique. This is a very important prerequisite for the low level suitability of the concept. In comparison to present experiments where the cryostat system is of the order of kilograms, the material needed for stable operation could therefore be reduced by roughly three orders of magnitudes which is also the basis of the background reduction power of the GENIUS concept.

9.3 Background simulations and considerations

Detailed investigations and simulations of the possible background sources expected for the GENIUS setup at the Gran Sasso underground laboratory with a shielding overburden of 3800 mwe have been made earlier [Kla99a, Maj98, Bau98c]. Figure 9.5 shows the sum spectrum in the low energy region below 100 keV obtained from the simulations relevant for WIMP dark matter direct detection.

The details of the geomtery and assumed impurities of the different components can be found elsewhere [Bau98c, Kla99a, Maj98].

The impurities simulated were the following:

- Photon flux from the surrounding,

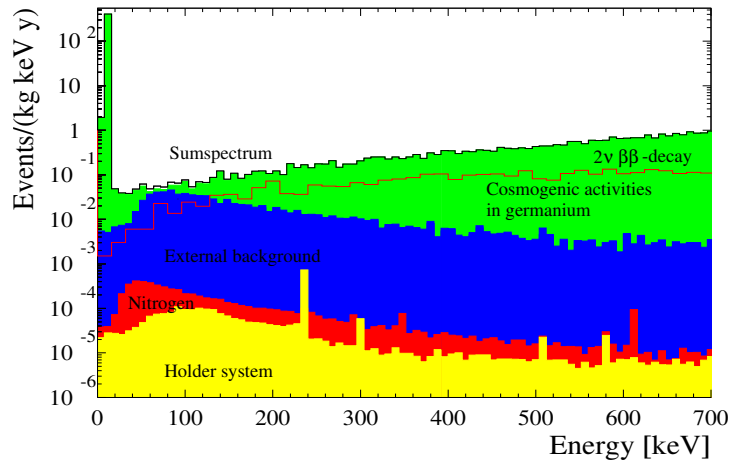- neutron flux from the surrounding,

- the Muon flux,

Figure 9.5: Sum spectrum of simulated background contributions for the GENIUS experiment in the energy region interesting for WIMP dark matter search. The most dominant feature of the spectrum will be the contribution from the cosmogenically produced isotopes.

- impurities of the steel vessel,

- intrinsic impurities of the liquid nitrogen,

- contribution from the detector holder system,

- cosmogenic activation of the germanium crystal.

Additionally some considerations regarding the muon flux have been made:

- Neutrons generated by muons,

- negative muon capture,

- inelastic muon scattering.

The background components resulting from the muon flux are discussed in detail in a later section of this chapter, where it is shown that any underground site with a shielding overburden greater than 2000 mwe is a suitable place for the GENIUS experiment. The main contributions are summarized in table 9.6, whereas this list makes the assumption of a shallower underground site as the Gran Sasso laboratory with a shielding overburden of 2000 mwe. The expected count rates for the Gran Sasso Underground laboratory due to muon interaction therefore varies slightly, but not significantly. For the original table of the GENIUS proposal see table 3.7 therein [Kla99a].

The sum spectrum of the simulated components is shown in figure 9.5. It is obvious that the cosmogenically produced isotopes will by far contribute the most to the overall background spectrum. Thus they deserve some more attention.

9.4 Cosmogenic activation of the Ge detectors at sea level

As evident from figure 9.5 the main background source limiting the sensitivity of GENIUS as a WIMP dark matter search experiment results from the isotopes produced by spallation reactions inside the germanium material induced by the hard component of cosmic rays during detector production and transport at sea level.

The activation of the germanium crystals with cosmogenic radioisotopes has been estimated using the Σ code [Boc94]. The programme was developed to calculate the enhancement of radionuclides in natural and enriched germanium and copper. It has been demonstrated earlier that it can reproduce the measured activations within a factor of approximately two [Mai95]. It should be noted however that the Σ code does not give any information on the cosmogenic tritium production. This matter is being discussed later.

In table 9.1 the result is shown for ten days of fabrication and transportation time, followed by three years of deactivation. For ^{68}Ge the saturation activity has been assumed since this isotope can not be removed through the zone refining process. All other isotopes not shown in table 9.1 are not relevant, since they either have a very short or long half life or their production rate is very low.

Isotope	Decay mode $T_{1/2}$	Energy [keV]	Ativity $[10^{-6}\mathrm{Bq\ kg^{-1}}]$
^{3}H	β^{-}, 12.35 a	E_{β_-}=18.6	$\sim 3.6(0.12)$
^{49}V	EC, 330 d	no γ, E (K$_\alpha$ ^{49}Ti)=4.5	0.17
^{54}Mn	EC, 312.2 d	E_γ=1377.1, E (K$_\alpha$ ^{54}Cr)=5.99	0.20
^{55}Fe	EC, 2.7 a	no γ, E (K$_\alpha$ ^{55}Mn)=5.9	0.31
^{57}Co	EC, 271.3 d	136.5 (99.82%) E (K$_\alpha$ ^{57}Fe)=7.1	0.18
^{60}Co	β^{-}, 5.27 a	318 (99.88%), $E_{\gamma 1,2}$=1173.24, 1332.5	0.18
^{63}Ni	β^{-}, 100.1 a	$E_{\beta-}$=66.95 no γ	0.01
^{65}Zn	EC, 244 d	E_γ=1115.55 (50.6%),E (K$_\alpha$ ^{65}Cu)=8.9	9.08
^{68}Ge	EC, 288 d	E (K$_\alpha$ ^{68}Ga)=10.37, Q_{EC}(^{68}Ga)= 2921	101.4

Table 9.1: Cosmogenic produced isotopes in the Ge crystals for an exposure time at sea level of 10 days and for 3 years deactivation time (except for ^{68}Ge, where the saturation activity was assumed)

The expected contributions from cosmogenic isotopes resulting from the simulations are shown in figure 9.6. The count rate of the detectors below 12 keV will clearly be dominated by X-rays from the decays of ^{68}Ge,^{49}V,^{55}Fe and ^{65}Zn and by the β spectrum of the ^{3}H decay if no protection against the hard component of the cosmic rays is provided during production. The X-rays al one will set the energy threshold of the experiment to 12 keV, however, this is still acceptable for dark matter search.

As discussed in the next section, it will be mainly ^{3}H which limits the attainable sensitivity of the experiment.
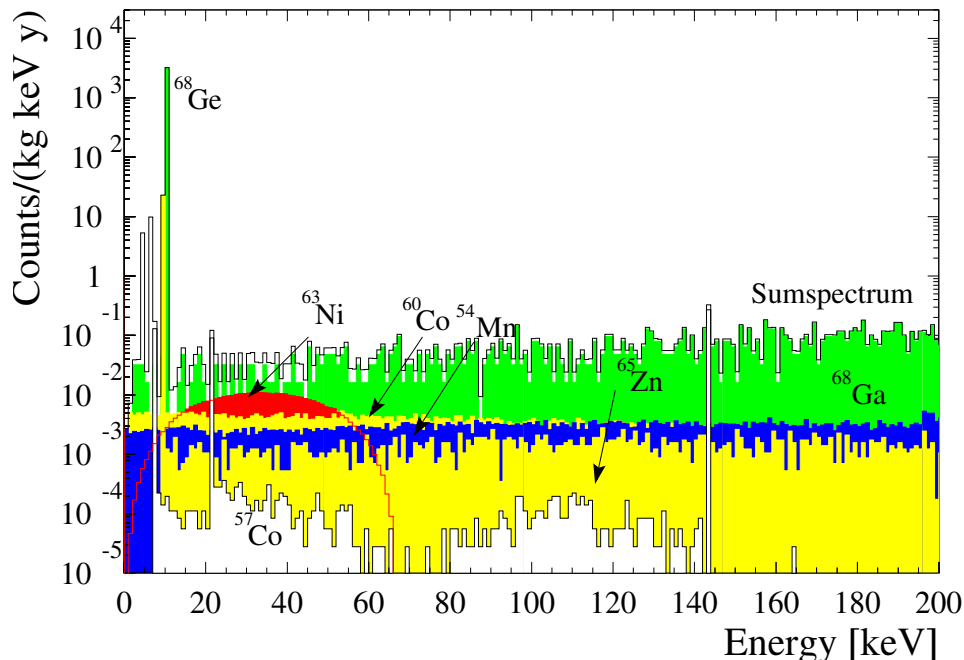
Figure 9.6: Expected contributions from the cosmogenically produced isotopes to the energy spectrum.

9.5   Tritium Production

As evident from the previous section, great care has to be taken about the cosmogenic isotopes produced inside the HPGe crystals at sea level. Without additional shield against the hard component of cosmic rays during a fabrication time of ten days many isotopes are produced which significantly reduce the sensitivity of GENIUS as a dark matter detector. Especially the production of ^{68}Ge from the isotope ^{70}Ge affects the sensitivity by increasing the energy threshold of the detector to 12 keV. In the main reaction leading to ^{68}Ge enhancement also tritium is produced: ^{70}Ge(n,t)^{68}Ge. Tritium has a half life of 12.35 years and can thus not be deactivated within a reasonable time. ^{3}H is a β emitter with a Q-value of 18.6 keV. The measured spectrum of tritium decay is shown in figure 9.7 [Lew70].

The cosmogenic production rate of ^{3}H in natural germanium has been estimated through simulations in [Col92, Avi92] using the cosmic neutron fluxes cited in [Lal67, Hes59]. For natural germanium it is estimated to be less than $\sim$ 200 atoms per day and kg material. Using this upper limit for tritium production at sea level with an overall fabrication time of ten days this would mean a tritium abundance of $\sim$ 2000 atoms per kilogram material. With the half life of 12.3 years this results in a decay rate of $\sim$3.6 μBq/kg equivalent to $\sim$113 decays per year (this is in very good agreement with the result in [Pon98]). Even assuming an energy threshold of 12 keV and taking into account the spectral
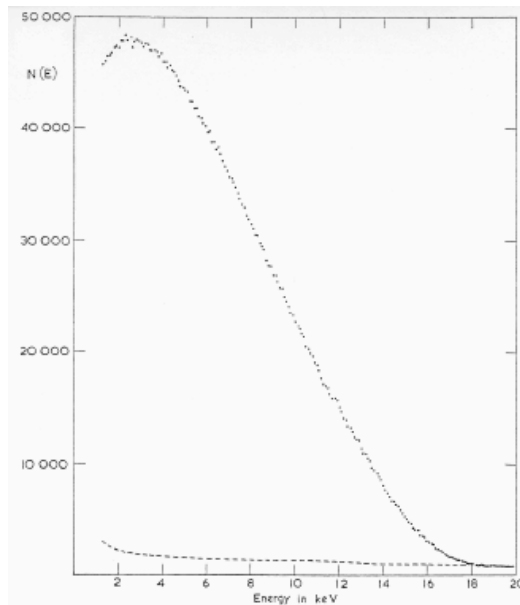
Figure 9.7: Measured Tritium spectrum (from [Lew70]). The lower curve corresponds to the background of the measurement without the tritium source.

shape of tritium decay (see figure 9.7) this yields an event rate of approximately 2 counts/(kg keV y) in the energy region between 12 keV and 19 keV, which is by two to three orders of magnitudes above the allowed count rate.

This consideration drastically shows the importance of proper planning of the crystal production and transportation. To avoid major problems with cosmogenic isotopes it is therefore essential to minimize the exposure of the crystals to cosmic rays at sea level.

In table 9.2 the detailed fabrication steps together with their duration are listed as reported by Perkin Elmer [San00]. It has been assumed here that during the zone refining process the germanium material is sufficiently shielded against the cosmic radiation. As evident from this table and from the previous considerations, the unshielded time is still by two orders of magnitudes too long. 3.5 days of exposure at sea level would result in approximately 0.7 counts/(kg keV d). Note though, that this would be the count rate due to the exposure during production only. In addition it has to be taken into account that the crystal might have to go through steps 10 to 13 in table 9.2 several times thus increasing the exposure time by another 16 hours per additional cycle.

It is therefore suggested to additionally shield the detector material during production and transportation using approximately 2m of heavy concrete. Heavy concrete can be produced with a density up to 5.9 g/cm^3. Thus an additional concrete shield of 1 m could act as a shield of roughly 5 mwe. This reduces the hard nucleonic component mainly responsible for the cosmogenic isotope production by one to two orders of magnitudes [Heu95]. A further increase of shielding strength does not seem to be reasonable since the cosmogenic production through the cosmic fast muons which is by approximately two orders of magnitudes less than through the hadronic component can not be shielded

	Process description	Duration
1	Receive Ge material from Eagle-Pitcher and cut into pieces appropriate for zone refining process	4 hours
2	Etch and load Ge material into zone refining machine	2 hours
3	Zone refining process	0 hours[1]
4	Evaluate and cut zone refined material into pieces appropriate for crystal growth	3 hours
5	Clean and etch zone refined Ge material and load into crystal growth machine	2 hours
6	Melt zone refined Ge material and grow Ge crystal into single crystal	28 hours
7	Cut, analyze and evaluate for detector suitability	8 hours
8	Mechanically shape and machine crystal into detector structur	8 hours
9	Lap, clean, etch and perform Li diffiusion	12 hours
10	Wet chemical processing into Ge detector	8 hours
11	Install detector inside cryostat and perform vacuum pumping and baking	4 hours
12	Cool detector to perform testing and evaluation	0 hours
13	If performance is acceptable, warm detector for transport	4 hours
	Total unshielded time	84 hours (3.5 days)
	If detector performance is not acceptable, steps 10,11,12 and 13 have to be repeated	16 hours

Table 9.2: Steps to be performed during production process of HPGe detectors. It has been assumed that the zone refining process can be done with propoer shielding of the germanium against comic rays.

whatsoever.

It is clear from the qualitative considerations made here that this topic still has to be investigated in great detail and solutions for the most effective shielding during production and transport have to be found.

To make a first approximation of the tritium abundance in the crystals after production and transportation, it is assumed that a shield of 5 mwe can be provided during both fabrication and transport, resulting in a reduction of tritium production by a factor of ~ 30 (see figures 2 and 3 in [Heu95]). Considering table 9.2 the time interval relevant for tritium enhancement starts directly after the zone refining process, since in this step most of the contamination is being removed from the germanium material. Thus for the fabrication (in the ideal case) 78 hours are needed. Without considering transport, this results in approximately 20 tritium atoms per kg detector material. Taking into consideration also a transportation time of one week (shipping), the amount of produced tritium atoms increases to $\sim$70 atoms per kg.

The expected decay rate is $\sim$1.1 per year without and $\sim$3.9 per year with transportation considered. If an energy threshold of 12 keV is assumed for the experiment due to the decay of ^{68}Ge, the events resulting from tritium decay below 12 keV can be neglected. Due to the spectral shape of tritium (figure 9.7), every $\sim$10th decay deposits more than 12 keV of energy in the

---

[1]Propper shielding of the germanium material during the zone refining process is assumed here.

detector. In the energy interval between 12 keV and 19 keV thus 0.11 events pre year and 0.39 events per year are expected from tritium without and with transportation considered, respectively. The final background sensitivity would therefore be $\sim$1.6$\times$10^{-2} counts/(kg keV y) without additional transportation and $\sim$5.6$\times$10^{-2} counts/(kg keV y) with a week of transport from the fabrication site to the site of the experiment.

Note that the consideration made here is a very crude approximation. It is however possible to say that tritium will definitely limit the sensitivity of GENIUS as a dark matter detector if the germanium crystals are not produced directely underground. Thus it should be seriously considered to produce the detectors underground, directly at the experimental site.

9.6 GENIUS at shallower underground laboratories

For the background considerations made so far it was assumed that the experiment will be built at the Gran Sasso underground laboratory in Italy. Due to the limitations in space it is however possible that annother installation site might be chosen. It is therefore important to know the background expectations for underground sites with different shielding overburden.

In this section calculations are presented which prove that also shallower underground sites as the Gran Sasso[2] with 3800 mwe, like e.g. the Waste Isolation Pilot Plant (WIPP) in Carlsbad Cavern, New Mexico, USA with a shielding of > 2000 mwe are suitable to operate the GENIUS experiment. The main difference between the two locations is the muon flux which is higher by up to a factor of 26 at WIPP in comparison to Gran Sasso. Various background contributions related to the higher muon flux at WIPP have been studied in detail. It is shown in this section that even an underground laboratory with only' 2000 mwe of shielding depth is acceptable as a location for the setup of the GENIUS experiment.

Evaluation of muon influences at WIPP

As a conservative assumption on the overall muon flux at WIPP, a shielding of 2000 mwe at this location is assumed (compare to > 2000 mwe given in [WIP00]). To crosscheck the method, we calculate from figure 4 of [Ure97] the vertical muon flux for the Gran Sasso Underground Laboratory, assuming a uniform muon intensity from all zenith angles of the upper half sphere. The calculated flux of $5\times10^{-4}m^{-2}s^{-1}$ coincides very well with the measured $2.3\times10^{-4}m^{-2}s^{-1}$ [Arp92] taking into consideration that the assumption of a uniform flux from all zenith angles is very conservative.

We obtain from figure 4 in [Ure97] a flux of $\sim6\times10^{-3}m^{-2}s^{-1}$ for WIPP, about 26 times larger compared to Gran Sasso.

Muon showers

The effect of muon showers has been studied using the energy distribution of muons at the Gran Sasso Underground Laboratory in a previous proposal

---

[2]for which the calculations have been carried out in [Bau98c, Kla00a]

[Kla00a]. It is a conservative assumption to use the same energy distribution since the energy spectrum of the muons hardens with increasing shielding. Using the result of this simulation we scaled the spectrum to the expected muon flux at WIPP. From muon generated electromagnetic showers we expect $\sim$2.6 counts/(kg keV y) in the detectors. Taking advantage of the anticoincidence between the 38 detectors we still expect $\sim$0.5 counts/(kg keV y). This is by about a factor of 50 above the aimed level. Thus a muon veto-shield with an efficiency of at least 99% has to be developed to reduce the muon induced countrate to a negligible level. This seems reasonable considering the fact that the CDMS experiment for instance reports a 99.9 % efficiency on their muon veto [Abu00]. With such a veto efficiency the count rate could be reduced to $\sim 5 \times 10^{-3}$ counts/(kg keV y).

Reaction	$T_{1/2}$ of the product	Decay energy
$^{14}N(n,p)^{14}C$	$T_{1/2}$=5.7$\times 10^3$y	$E_{\beta-}$=0.16 MeV
$^{14}N(n,\gamma)^{15}N$	stable	
$^{14}N(n,2n)^{13}N$	$T_{1/2}$= 9.96 m	$E_{\beta+}$=1.2 MeV
$^{14}N(n,\alpha)^{11}B$	stable	
$^{14}N(n,t)^{12}C$	stable	
$^{14}N(n,2\alpha)^7Li$	stable	

Table 9.3: Neutron interactions in the liquid nitrogen of the GENIUS vessel for neutron energies < 20 MeV.

Neutrons generated by muons

In extended muon showers fast neutrons are being produced at a non-negligible level. To estimate the number of produced neutrons per year, we scaled the result reported in [Kla99a] to the flux at WIPP. The old calculation can now be confirmed by comparison with new data obtained by the LVD collaboration [Agl99]. In this paper a mean production rate per muon at Gran Sasso of $\langle N \rangle$=(1.5$\pm$0.4)$\times 10^{-4}$ neutrons/(muon event)/(g/cm^2) is reported. For the dimensions of the proposed Genius tank this results in a production rate of $\sim 1.2 \times 10^5$) neutrons/year in the whole tank at the Gran Sasso. This is in good agreement with our previous calculation based on [AGL89] of 2.5$\times 10^5$ neutrons/year [Kla99a]. To be conservative, we use the higher old value from [Kla99a]. Scaling this value up to the flux at the WIPP site (assuming the same energy spectrum of the muons as in Gran Sasso which is again a conservative assumption), yields a production rate of $\sim 6.5 \times 10^6$ neutrons/year in the whole tank.

This neutrons can undergo reactions with the nitrogen as listed in Tab. 9.3 [MLa88]. The resulting nucleus is normaly produced in an excited state. The deactivation gammas, typically with energies around 10 MeV give rise to a further background contribution. The assumption that each muon induced neutrons undergoes one of the reactions from Tab. 9.3 results in $\sim$6.5$\times 10^6$ high energetic gammas per year, randomly distributed in the tank. Monte Carlo simulations, starting 5$\times 10^6$ 15 MeV gammas show that no more than $\sim$1.6$\times 10^{-2}$ counts/(kg keV y) result from this component. Using the muon veto with an efficiency of 99% this countrate reduces to $\sim$1.6$\times 10^{-4}$counts/(kg

Isotope	$T_{1/2}$	Decay mode	Decay energy	Rate at WIPP [y^{-1}]
^{69}Ge	39h	EC (64 %)	E_{x-ray}=10.37 keV	74
		β^+ (36 %)	$Q_{\beta+}$=2.23 MeV	41
^{71}Zn	2.4m	β^-	$Q_{\beta-}$=2.82 MeV	70
^{72}Ga	14.1h	β^-	$Q_{\beta-}$=3.99 Mev	46
^{74}Ga	8.1m	β^-	$Q_{\beta-}$=5.4 MeV	46
^{75}Ge*	48s	γ to ground state	E_{γ}=140 keV	115
^{75}Ge	82.8m	β^-	$Q_{\beta-}$=1.18 MeV	92

Table 9.4: Isotopes produced in 100 kg HPGe through muon induced neutrons [MLa88]. Note that the excited states of the isotopes ^{74}Ge* and ^{71m}Ge* are not listed here since they can be effectively vetoed using the muon veto, due to their short life times.

keV y).

From the products of the reactions listed in Tab. 9.3 only ^{13}N and ^{14}C are not stable and can not be discriminated through the muon veto since their half lifes are too long. The production rate of these nuclei is $\sim 7.5 \times 10^5$ ^{14}C atoms and $\sim 2.5 \times 10^5$ ^{13}N atoms per year in the whole tank. ^{14}C is negligible as a background component due to its long half life and the resulting low decay probability ($\sim$ 100 decays per year randomly distributed in the whole tank). For the contribution of ^{13}N we made Monte Carlo simulations. We expect $\sim 10^{-3}$counts/(kg keV y) from this contribution at the WIPP site.

In the High Purity Germanium material $\sim$ 300-600 neutrons/y will be generated by muons in the WIPP site in 100 kg of detector material [AGL89, Agl99]. Reactions of these neutrons with the Ge target nuclei result in isotopes [MLa88] listed in Tab. 9.4 together with the decay mode and production rate at the WIPP site. The effect of the decay of these nuclei has been simulated resulting in a background contribution of $\sim 3 \times 10^{-3}$ counts/(kg keV y) in the energy region below 100 keV. In the energy region of the neutrinoless Double-Beta decay of ^{76}Ge a contribution of $\sim 2 \times 10^{-4}$ counts/(kg keV y) is expected.

Reaction	$T_{1/2}$	Decay energy	Rate at WIPP[y^{-1}]	at LNGS [y^{-1}]
^{14}N(μ,ν_μ)^{14}C	$T_{1/2}$=5.7×10^{4}y	$E_{\beta-}$=0.16 MeV	15184	584
^{14}N(μ,$\nu_\mu\alpha$)^{10}Be	$T_{1/2}$=1.6×10^{10}y	$E_{\beta-}$=0.6 MeV	754	29
^{14}N(μ,ν_μp)^{13}B	$T_{1/2}$=17.33ms	$E_{\beta-}$=13.4 MeV	3016	116
^{14}N(μ,ν_μn)^{13}C	stable		98748	3798
^{14}N(μ,$\nu_\mu\alpha$n)^{9}Be	stable		442	17
^{14}N(μ,$\nu_\mu\alpha$p)^{9}Li	$T_{1/2}$=178ms	$E_{\beta-}$=13.6 MeV	16	0.6
^{14}N(μ,ν_μ2n)^{12}C	stable		30368	1168
^{14}N(μ,ν_μ3n)^{11}C	$T_{1/2}$=20.38m	$E_{\beta-}$=.96 MeV	7592	292
^{14}N(μ,ν_μ4n)^{10}C	$T_{1/2}$=19.3s	$E_{\beta+}$=1.9 MeV	3042	117

Table 9.5: Spallation reactions from muon capture.

Negative muon capture and spallation

Tab. 9.5 shows the possible muon spallation reactions and the calculated rate for the Gran Sasso and the WIPP site. At WIPP $\sim 1.6 \times 10^5$ negative muon

Source	Component	Count rate (11-100 keV) [counts/(kg y keV)]
Nitrogen	^{238}U	7×10^{-4}
intrinsic	^{232}Th	4×10^{-4}
	^{40}K	1×10^{-4}
	^{222}Rn	3×10^{-4}
N activation	^{14}C	1×10^{-4}
Steel vessel	U/Th	1.5×10^{-5}
Holder system	U/Th	8×10^{-4}
Surrounding	Gammas	4×10^{-3}
	Neutrons	4×10^{-4}
	Muon shower	5×10^{-3}
	$\mu \to$ n in LN$_2$	1.2×10^{-3}
	$\mu \to$ n in HPGe	3×10^{-3}
	$\mu \to$ capture	4×10^{-4}
	$\mu \to$ inelastic	1×10^{-3}
Cosmogenic	^{54}Mn	3×10^{-3}
activities	^{57}Co	1×10^{-4}
in the crystals	^{60}Co	4×10^{-3}
	^{63}Ni	6×10^{-3}
	^{65}Zn	1.5×10^{-3}
	^{68}Ge	3.7×10^{-2}
Total		6.8×10^{-2} counts/(kg y keV)

Table 9.6: Summation of background components expected at the WIPP-site in the region 12 keV–100 keV.

capture reactions are expected, resulting in excited nuclei which emit high energy gammas. We expect a countrate from the abovementioned simulations from these nuclei of $\sim 4 \times 10^{-4}$ counts/(kg keV y). The muon veto anticoincidence makes this contribution negligible. Also the production of unstable nuclei - which can not be discriminated through the muon veto due to their long half lifes - is very low (see Tab. 9.5).

Inelastic muon scattering

Through the reactions of the type $\mu + N \to \mu' + X^*$ only the isotopes ^{13}N and ^{14}C are produced with a half life > 1s. We expect a production rate of $\sim 2 \times 10^5$ nuclei per year for both isotopes. Again ^{14}C is negligible. The contribution from ^{13}N will be of the same order as from muon induced neutrons, resulting in an expected count rate of $\sim 10^{-3}$ counts/(kg keV y).

9.6.1   Intrinsic impurities and natural radioactivity and the sum spectrum

For the contribution of the intrinsic impurities in liquid nitrogen, the holder system and the vessel wall we can refer to [Kla99a]. These values have been used in Tab 9.6.

The natural radioactivity and the ^{40}K activity from the surrounding is lower at the WIPP site by a factor of 1.5-10 for the natural decay chains and up to

a factor of 10 for thermal neutrons. Thus it is conservative to assume the same contributions from these sources as in [Kla99a].

The sum of all contributions awaited at an underground side with a shielding overburden of 2000 mwe is shown in table 9.6. It is evident that the increase of the muon induced contribution to the background is not relevant with respect to the contribution expected from the direct surrounding. It can therefore be stated that the background requirements for the GENIUS experiment can be fulfilled in all Underground laboratories with a shielding depth of > 2000 mwe and with a similar level of natural background radiation as in the Gran Sasso underground laboratory. Therefore it seems reasonable to take into consideration alternative installation sites like the Waste Isolation Pilot Plant (WIPP) in Carlsbad Caverns, New Mexico, USA or the Center for Underground Physics in Pyhäsalmi (CUPP) [CUP00].

Chapter 10

Proposals for smaller scale test setups

The concept of the GENIUS proposal has the great advantage that no individual cryostat system is needed. Instead the HPGe crystals are surrounded by liquid nitrogen of much higher radiopurity which in addition provides ideal cooling and shielding against external radiation. Thus the background can be considerably reduced and the sensitivity can be drastically improved with respect to the Heidelberg–Moscow $\beta\beta$ experiment. This opens new investigation potentials for Genius [Kla98a, Kla98b]. The planned installation site for the GENIUS experiment is the Gran Sasso Underground Laboratory at LNGS/INFN in Italy. Due to the limited space in the underground facilities the size of the experiment puts severe constraints on the installation location. It therefore seems reasonable to first explore the possibility of setting up an intermediate or small size test detector as a first step towards the realization of the full scale GENIUS experiment.

In this chapter first the GENINO proposal is introduced which is based on the idea to replace a part of the liquid nitrogen shielding strengths against external radiation by an additional lead or steal layer around the tank. Detailed simulations were made in the course of this thesis to investigate the reachable sensitivitiy of such an experiment. In the second section the BARGEIN setup is proposed which uses the idea to abandon the liquid nitrogen shield and thus drastically reduces the overall size of the experiment while still being able to obtain physically relevant data in terms of dark matter search and neutrinoless double beta decay.

10.1 The GENINO proposal

A study for a smaller scale experiment, GENINO, was made which could allow to test the complete holder system with 38 HPGe crystals, the time stability of detector performance, the electronics and data acquisition system and the radiopurity and activations of the used materials down to the level of approximately 10^{-1} events/(kg keV y).

The goal of an intermediate step is to drastically reduce the size of the tank in comparison to the full scale GENIUS site while still yielding valuable scien-

tific results. The size of the experiment can be reduced by partially replacing the nitrogen shield by a radio pure material with significantly higher density. The material taken into consideration for the GENINO setup is commonly used Boliden lead. If however a significant improvement of sensitivity with respect to the Heidelberg–Moscow $\beta\beta$ experiment has to be reached, the liquid nitrogen still has to be used to partially serve as a shield against the lead. Thus the minimal size of the tank for the GENINO proposal is determined by the radioactive contaminations of the vessel wall, the polystyrene foam isolation and the additional lead shield. The GENINO project aims for a reduction of background by a factor of ∼20 with respect to the Heidelberg–Moscow $\beta\beta$ experiment. As will be shown in this section, this requires a liquid nitrogen shielding thickness of 5 meters in diameter.

The GENINO detector would consist of two concentric stainless steel tanks with the Ge crystals positioned in the center. The inner tank would contain liquid nitrogen as the working medium for the Ge crystals and as a partial shield against the natural radioactivity from the Gran Sasso rock. The outer vessel would contain the isolation material. The germanium crystals would be placed on a holder system made of e.g. teflon which could house up to six layers of 38 crystals each (see figure 10.2). On the top of the tank there would be a clean room with a lock chamber, a room for the electronics and the data acquisition system, and a muon veto shield.

It is shown in this chapter that GENINO could give important insights into the field of direct dark matter detection despite the reduced sensitivity with respect to the GENIUS project [Kla00a]. Also the sensitivity for neutrinoless double beta decay could be improved by a factor of ∼5 with respect to the present sensitivity of the Heidelberg-Moscow experiment.

However, the cost for such a step would be comparable to that of the full size setup since the main cost factor for both projects are dominated by the production of the HPGe-detectors and the development of a super low level clean room on top of the tank. On the other hand, both, clean room and HPGe detectors designed for GENINO could be used in the GENIUS experiment thus substantially reducing the cost for the later.

10.1.1 The concept of the GENINO Proposal

GENINO would operate an array of 38 'naked' crystals made out of HPGe in a cylindrical vessel filled with liquid nitrogen. The total mass of the 38 detectors would be 100 kg. The goal of GENINO is to reach a count rate of about 1 event/(kg keV y) in the energy region below 100 keV (a factor 20 less than reached for the Heidelberg-Moscow experiment). This would permit to test the complete DAMA evidence region which was confirmed by the DAMA collaboration after another two years of data taking with a total statistics of 57986 kg d [Ber00b]. Besides that an active mass of 100 kg would be high enough to search for the WIMP dark matter signature in form of the annual modulation of the event rate with high modulation significance. This could be an independent test of the claimed DAMA evidence [Ber00b] by measuring the WIMP-recoil energy spectrum as well as the WIMP modulation amplitude.

The nitrogen shielding of the GENINO setup would be 5 m in diameter. In addition to the nitrogen, a shield of 25-30 cm of lead is unavoidable in order to reduce the background by a factor of 20 with respect to the current level of

the Heidelberg-Moscow experiment. The possibility of using such a setup for the GENIUS experiment with full sensitivity has been studied before [Maj98]. The thickness of the thermal isolation material would be 1.2 m. Thus the total dimension of the experiment would be about 8.0 m in diameter and height (see figure 10.1 for a schematic view).
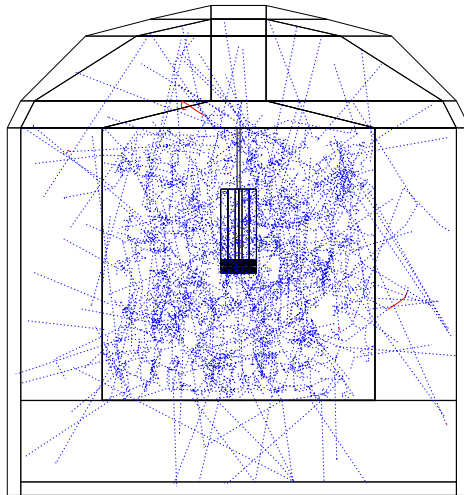

Figure 10.1: Simulated geometry of the GENINO proposal. The HPGe detectors are centered in the tank. They are immerse on a holder structure into the liquid nitrogen. The liquid nitrogen is isolated by a polystyrene foam layer of 1.2 meters which is held by inner and outer steel vessels. A subsequent ~ 30 cm lead layer shields the detectors against the external radioactivity.

The detection technique for GENINO is based on ionization in the HPGe detectors. The detectors would be coaxial HPGe crystals of p-type, weighing about 2.7 kg each (same design as for the GENIUS project since the detectors used for this setup are designed to be later implemented into the final experiment). Since the crystals would be of p-type, the outer dead layer, corresponding to the inactive mass of the crystal would be about 0.7 mm, thus effectively protecting the detector against external α- and β-radiation. The working temperature of the detectors, 77 K, would be the same as for the GENIUS project as well as the energy resolution and threshold with 0.3% and 12 keV respectively.

10.1.2   Background simulations

To study the expected background in the GENINO setup, detailed Monte Carlo simulations of all the relevant background sources were performed with a new detector geometry (see figure 10.1). The background sources can be divided into external and internal ones. External background is generated by events originating from outside the shield such as photons and neutrons from the Gran

Sasso rock, muon interactions and muon induced activities. Internal background arises from residual impurities in the liquid nitrogen, in the steel vessel, the isolation material and the shield, in the crystal holder system, in the Ge detectors themselves and from activation of both, liquid nitrogen and Ge crystals at the earth surface.

For the simulation of muon showers the external photon flux, the neutron flux and the radioactive decay chains the GEANT3.21 package [GEANT] extended for nuclear decays were used [Mai95]. This version has already been successfully tested in establishing a quantitative background model for the Heidelberg-Moscow experiment [Hei97, Die99].

The following detector geometry was used to perform the simulations: The nitrogen shield is supplied by a cylindrical vessel of 5 m in diameter and height, with the detector crystals positioned in its center. The vessel is surrounded by a 1.2 m thick polystyrene-foam isolation which is held by two 5 mm thick steel layers. A 30 cm thick lead shield can optionally surround the outer steel layer. The simulated setup consists of 38 natural Ge detectors integrated into a holder system of high molecular polyethylene. See figure 10.1 for a schematic view of the simulated geometry.
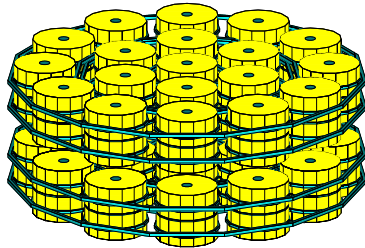

Figure 10.2: Schematic view of possible configuration of the holder system for the Ge crystals with two layers.

Photon flux from the surrounding

For the photon flux data from a measurement in hall C of the Gran Sasso underground laboratory with energies between 0-3 MeV [Arp92] was used. This measurement is in good agreement with calculations of the photon flux performed by the Borexino collaboration [BOR91]. The main contributions are given in table 10.1.

The obtained count rate from the external low energy gamma rays for a 5 m liquid nitrogen tank in the energy region 12-100 keV is 3×10^4 counts/(kg keV y) without additional lead shielding. This is by a factor of three to four orders of magnitudes higher than the actual background of the Heidelberg–Moscow $\beta\beta$ experiment. Consequently, an outer shield of 25-30 cm of low level Boliden lead would be unavoidable. This reduces the count rate in the low energy region to $\sim 7 \times 10^{-2}$ counts/(kg keV y). An alternative to lead could be a 50 cm steel

Isotope	Energy [keV]	Flux $[\mathrm{m}^{-2}d^{-1}]$
^{214}Pb	241.9	$0.3 \cdot 10^7$
^{214}Pb	295.2	$0.8 \cdot 10^7$
^{214}Pb	352.0	$1.8 \cdot 10^7$
^{214}Bi	609.3	$2.9 \cdot 10^7$
^{214}Bi	1120.3	$1.4 \cdot 10^7$
^{214}Bi	1764.5	$1.7 \cdot 10^7$
^{212}Pb	238.6	$0.34 \cdot 10^7$
^{208}Tl	338.7	$0.09 \cdot 10^7$
^{208}Tl	538.0	$0.41 \cdot 10^7$
^{208}Tl	911.2	$0.48 \cdot 10^7$
^{208}Tl	2614.5	$1.35 \cdot 10^7$
^{40}K	1460.0	$3.8 \cdot 10^7$

Table 10.1: Simulated components of the gamma ray flux from natural radioactivity in the Gran Sasso laboratory (taken from [Arp92])

shield (corresponding to ~500 tons) under the prerequisite that steel can be produced in low level quality in such a large amount.

Besides the low energy photon flux the photons with energies between 6 MeV and 36 MeV were simulated. The gamma-ray flux with energies between 6 MeV and 9 MeV results from (α,n)-reactions in the Gran Sasso rock with subsequent n-capture. The flux in the higher energy region between 9 MeV and 32 MeV originates from bremsstrahlung photons created in the muon interactions with the rock and other materials. This flux has been measured in the Modane Laboratory in Frejus, France [Dec99].

By comparing the U and Th abundances of the Modane and Gran Sasso (Hall C or B) rock on the one side and the muon fluxes at the depth of the two laboratories on the other side, the following upper limits on the high energetic photon flux in the Gran Sasso laboratory is inferred: between 6 MeV and 9 MeV: 1.5×10^{-6}cm^{-2}s^{-1}, between 9 MeV and 32 MeV: 6×10^{-8}cm^{-2}s^{-1}.

The results of the simulation are 50 counts/(kg keV y) in the energy region below 100 kev without lead shield and 5×10^{-3} counts/(kg keV y) with lead shielding. The simulated spectrum is shown in figure 10.3.

Neutron flux from the surrounding

For the simulation of the neutron flux measured in Gran Sasso [Bel89] the GCALOR95 program package [GCAL95] was used. GCALOR95 simulates hadronic interactions down to the thermal region for neutrons, using the low energy neutron code MICAP [GCAL95]. For high particle energies the FLUKA model is used. MICAP calculates interactions of low energetic neutrons (energies from 20 MeV down to 10^{-5} eV) with a given nucleus. It utilizes data on partial cross-sections, angular distributions and secondary energy distributions which are available for 48 isotopes, among them also germanium, nitrogen, carbon, hydrogen, lead and iron. The type of processes implemented in MICAP range from elastic scattering to all types of inelastic reactions like n(A,A$^{'}$)n$^{'}$, n(A,A$^{'}$)2n$^{'}$, n(A,A$^{'}$)γ, n(A,A$^{'}$)d, etc (see the GCALOR manual [GCAL95]). If the residual nucleus remains in an excited state after the interaction, deexcita-

tion gammas are generated. The interactions which are particularly important for GENINO are ^{14}N(n,p)^{14}C* and ^{14}N(n,γ)^{15}N* since the relevant contribution to the background results from the deexcitation of the ^{14}C* and ^{15}N* nuclei. The contribution of the β-decay of ^{14}C in the liquid nitrogen is negligible since only low energy electrons (E$_{\beta max}$=156 keV) are emitted and the decay probability is very low due to the long half life (10^{-4} per year). The resulting mean countrate in the low-energy region due to neutron interactions is about 8×10^{-3} counts/(kg keV y) (see also figure 10.3).

Activities induced by muons

The measured muon flux in the Gran Sasso Underground laboratory is about ϕ_μ=2.3$\times10^{-4}$m^{-2}s^{-1} with a mean energy of $\bar{E}_\mu$=300 GeV [Arp92]. The total flux with the energy distribution taken from [deM92] was simulated. The count rate due to the muon induced showers in the low energy region is about 1×10^{-1} counts/(kg keV y). This is reduced to 2×10^{-2} counts/(kg keV y) ($\sim$ factor five) taking into account the anti-coincidence between the 38 Germanium detectors (see figure 10.3 for the simulated anti-coincidence spectrum resulting from the muon showers)

In the GENIUS proposal [Kla98b] also muon-induced nuclear disintegration and interactions due to secondary neutrons generated in the above reactions were considered. However, these reactions did not give a substantial contribution to the background even with a count rate as low as 1×10^{-2} counts/(kg keV y) aimed at. Their contribution would be even less in the GENINO project.

Steel vessel, lead shielding and isolation material

One of the dominant background sources is the 5 mm thick steel vessel. Assuming a contamination of 9 mBq/kg for the ^{238}U decay chain and 11 Bq/kg for the ^{232}Th decay chain (as measured in a sample for the Borexino collaboration [Lau99]), according to the simulations a count rate of $\sim$0.25 counts/(kg keV y) results from this component using a tank with 5 m of liquid nitrogen shield. This is lower by two orders of magnitudes than the mean count rate of the Heidelberg–Moscow $\beta\beta$ experiment in the same energy region thus being sufficient for a reasonable reduction of the mean background count rate.

For a tank geometry with 4 m in diameter the steel would give a contribution of $\sim$1 counts/(kg keV y) in the low energy region. Thus with a 4 m liquid nitrogen tank the vessel contamination alone would already contribute with the maximal allowed background count rate not considering the fact that the steel contamination values were obtained from a very clean sample. Therefore it is evident that an inner vessel with 4 m diameter is not sufficient for a reasonable increase in sensitivity with respect to already existing experiments. The impurity of commonly used Boliden lead was measured in an independent measurement with one of the low level detectors in the Gran Sasso laboratory resulting in a contamination of this lead of $\sim$4 mBq/kg for the ^{238}U decay chain and $\sim$2 mBq/kg for the ^{232}Th decay chain. The contribution of such a lead shield to the overall background can be seen in figure 10.3. It accounts with $\sim$0.2 counts/(kg keV y) to the count rate.

The radioactivity of polystyrene granulate was obtained in an earlier measurement to be 7.3 mBq/kg for the ^{238}U decay chain, 2.1 mBq/kg for the ^{232}Th decay chain and 8.0 mBq/kg for the ^{40}K contamination (see chapter 10.3.2). Using these values a mean count rate from the polystyrene isolation material of ~0.07 counts/(kg keV y) is expected (see figure 10.3).
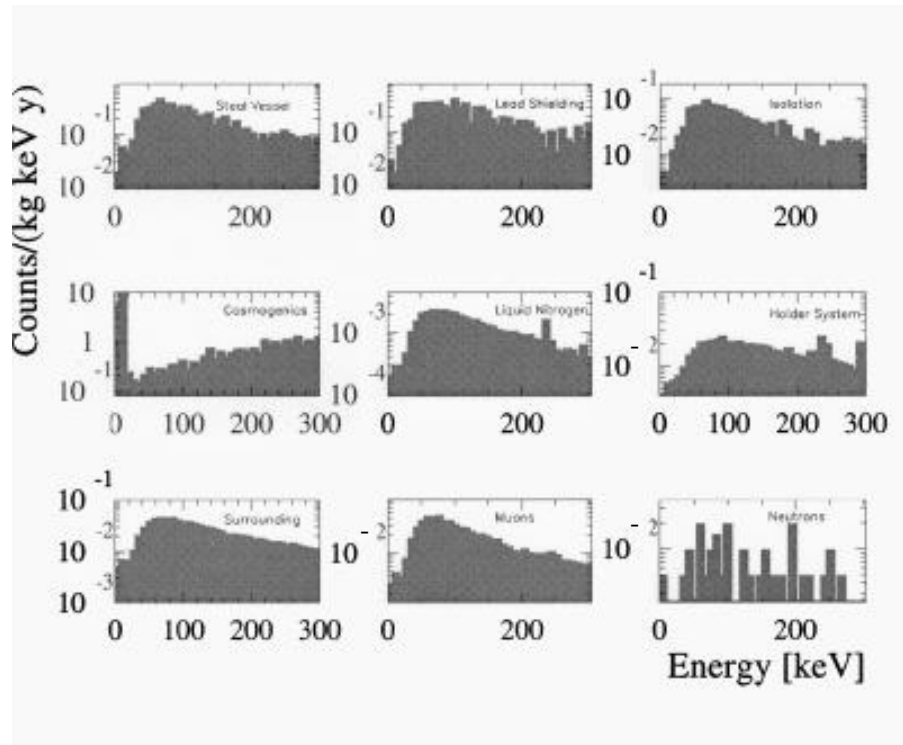

Figure 10.3: Simulated background components awaited for the GENINO proposal. The main contributions to the background are awaited from contaminations of the steel vessels, the lead shielding and the intrinsic contamination with cosmogenicallyof produced isotopes in the HPGe detectors.

Liquid nitrogen and holder system

The assumed impurity levels for the liquid nitrogen are listed in table 10.2. For the ^{238}U and ^{232}Th decay chains they have been measured by the Borexino collaboration for their liquid scintillator [BOR98]. Due to the very high cleaning efficiency of fractional distillation, it is conservative to assume that these requirements will also be fulfilled for liquid nitrogen. The ^{238}U and ^{232}Th decay chains were simulated under the assumption that they are in secular equilibrium.

Measurements of the ^{222}Rn contamination of freshly produced liquid nitrogen yield 325 μBq/m^3 [Heu00]. After about a month this is reduced to about 3 μBq/m^3 (T$_{1/2}$=3.8 days). Such a level could be maintained if the evaporated nitrogen is always replaced by Rn-pure nitrogen, previously stored in an underground facility (or if a nitrogen cleaning system is used) or if a nitrogen recycling device (through condensation) is installed inside the tank. The latter

would reduce the Rn contamination to a negligible level. Surface contaminations are reduced to a negligible level for cooled surfaces in direct contact with liquid nitrogen.

Source	Radio-nuclide	Purity
Nitrogen	^{238}U	3.5×10^{-16}g/g
	^{232}Th	4.4×10^{-16}g/g
	^{40}K	1.0×10^{-15}g/g
	^{222}Rn	3μBq/m^3
Steel vessel	^{238}U	0.7×10^{-9}g/g
	^{232}Th	2.7×10^{-9}g/g

Table 10.2: Assumed contamination levels for the liquid nitrogen and the steel vessel (the radon contamination for liquid nitrogen is given for gaseous nitrogen). Data taken from [BOR98, Heu00, Lau99].

The expected mean count rate from the contamination of liquid nitrogen with ^{222}Rn, ^{40}K and the U/Th decay chains in the region below 100 keV is $\sim 1 \times 10^{-3}$ counts/(kg keV y) assuming the activities from table 10.2. As evident from figure 10.3, even if the assumptions on purity of the liquid nitrogen are weakened by one order of magnitude, the resulting count rate would not severely constrain the attainable background level.

The geometry of the simulated holder system is depicted in figure 10.2. It was assumed that it is possible to obtain a holder material with an impurity concentration of 10^{-12}g/g or less for the U/Th decay chains. Encouraging are the results already achieved by the SNO experiment [SNO97]; they developed an acrylic with current limit on ^{238}U and ^{232}Th contaminations of just this values of 10^{-12}g/g. For the contamination with ^{40}K we took upper limits from a measurement of vespel polyamid obtained by the Borexino collaboration of 1.05 mBq/kg [vHen99].

Assuming the above impurity levels, with the simulated geometry a count rate of $\sim 1 \times 10^{-2}$ counts/(kg keV y) in the energy region below 100 keV from this component is expected.

For the intrinsic impurity concentration in Ge crystals we can give upper limits from measurements with the detectors of the Heidelberg–Moscow $\beta\beta$ experiment. A clear α-peak is seen in two of the enriched detectors at 5.305 MeV and a n indication for the same peak in two other detectors. It originates from the decay of ^{210}Po (which decays with 99% through an α-decay to ^{206}Pb) and is a sign for a ^{210}Pb contamination of the detectors. However, it is very unlikely that the contamination is located inside the Ge-crystals. The most probable location of this impurity is the crystals surface at the inner contact.

Using three Ge detectors, an upper limit at 90% C.L. (after 19 kg y counting statistics) of 1.8×10^{-15}g/g for ^{238}U and 5.7×10^{-15}g/g for ^{232}Th was derived in [Kla99a]. Assuming these impurity concentrations throughout the whole Ge detector volumes, the simulations yield a count rate of about 10^{-2} counts/(kg keV y) in the low energy region below 100 keV for both ^{238}U and ^{232}Th decay chains which is lower as what can be reached with GENINO by two orders of magnitudes.

Cosmic activation of the germanium crystals

An estimation of the cosmogenic production rates of radio-isotopes in the germanium crystals during production at sea level has been done earlier [Kla99a] (see also chapter 9.4, however note the different assumed history of the detectors) using the Sigma program [Boc94]. The program was developed to calculate cosmogenic activations of natural germanium, enriched germanium and copper. It was demonstrated that it can reproduce the measured cosmogenic activity in the Heidelberg–Moscow $\beta\beta$ experiment within about a factor of two [Hei97, Mai95]. For estimation of the Tritium production inside Germanium, data were obtained from [Col92]. See chapter 9.5 for a discussion of this component.

Isotope	Decay mode $T_{1/2}$	Energy [keV]	Activity $[10^{-6}\text{Bq kg}^{-1}]$
^{3}H	β^-, 12.35 a	E_{β_-} =18.6	3.6
^{49}V	EC, 330 d	no γ, E (K_α ^{49}Ti)=4.5	0.79
^{54}Mn	EC, 312.2 d	E_γ=1377.1, E (K_α ^{54}Cr)=5.99	1.03
^{55}Fe	EC, 2.7 a	no γ, E (K_α ^{55}Mn)=5.9	0.52
^{57}Co	EC, 271.3 d	136.5 (99.82%) E (K_α ^{57}Fe)=7.1	1.17
^{60}Co	β^-, 5.27 a	318 (99.88%), $E_{\gamma 1,2}$=1173.24, 1332.5	0.24
^{63}Ni	β^-, 100.1 a	$E_{\beta-}$ =66.95 no γ	0.01
^{65}Zn	EC, 244 d	E_γ=1115.55 (50.6%),E (K_α ^{65}Cu)=8.9	9.08
^{68}Ge	EC, 288 d	E (K_α ^{68}Ga)=10.37, Q_{EC}(^{68}Ga)= 2921	588

Table 10.3: Like table 9.1 with different assumed history of Ge-crystals: exposure time at sea level of 10 days and 1 year deactivation time (except for ^{68}Ge, where the saturation activity was assumed)

Assuming a production plus transportation of 10 days at sea level for the natural Ge detectors (with the exception of ^{68}Ge, where the saturation activity has to be assumed) and a deactivation time of one year, the radio-isotope concentrations listed in table 10.3 are obtained. All other produced radio-nuclides have much smaller activities.

The count rate below 12 keV is dominated by X-rays from the decays of ^{68}Ge, ^{49}V,^{55}Fe, ^{65}Zn and ^{3}H (see table 10.3). Due to their strong contribution, the energy threshold of GENINO would be at 12 keV which is still acceptable.

^{68}Ge plays a special role. Since it can not be extracted by zone melting like all other, non-germanium isotopes, the starting activity would be in equilibrium with the production rate. After one year of deactivation below ground, the activity is about 600μBq/kg. With a half life of 288 days it will dominate the other background components in all energy regions (with about 10^{-1} counts/(kg keV y) below 100 keV). Since the typical half life of cosmogenically produced long lived materials is around 200 days, the situation changes as time passes by. After three years of deactivation below ground, the activity of ^{68}Ge is about 100μBq/kg, thus the contribution of other long lived cosmogenics like ^{63}Ni becomes more important in the energy region between 12 keV and 100 keV. Details on this topic are found in [Kla99a]. It is important that the production and underground storage of the detectors to be implemented in the GENIUS setup starts as soon as possible to have enough time for deactivation of the cosmogenic isotopes before the start of the measurements.

However, the Heidelberg–Moscow $\beta\beta$ experiment presently operates several

HPGe-detectors in the Gran Sasso underground laboratory which could be used in the first test setup. These detectors are stored below ground since several years. Therefore their contamination with cosmogenic materials is suppressed by a factor of up to three orders of magnitudes. This would especially allow to achieve a lower energy threshold (of about 5 keV) due to the vanishing of the X-ray lines around 10 keV.

Cosmic activation of nitrogen at sea level

An estimation of production rates of long-lived isotopes in the nitrogen at sea level has been made [Kla99a, Kla00a], revealing the importance of ^{7}B, ^{10}Be, ^{14}C and ^{3}H. These components are discussed in detail elsewhere [Kla99a].

Sum spectrum from simulation of the GENINO setup

In table 10.4 the components discussed so far are listed and summed up.

Source	Component	Count rate (12-100 keV) [counts/(keV kg y)]
Germanium	U/TH	1×10^{-2}
Nitrogen	U/Th/K/Rn	1×10^{-3}
Steel vessel	U/Th	2.5×10^{-1}
Lead	U/Th	2.0×10^{-1}
Isolation	U/Th	7.0×10^{-2}
Holder system	U/Th	1.0×10^{-2}
Surrounding	Gammas (LE)	7.0×10^{-2}
	Gammas (HE)	5.0×10^{-3}
	Neutrons	8.0×10^{-3}
	Muon showers	2.0×10^{-2}
Cosmogenics in Ge	^{54}Mn, ^{57}Co,^{60}Co ^{63}Ni, ^{65}Zn,^{68}Ge	1×10^{-1}
Cosmogenics in N	^{7}Be	8×10^{-3}
	^{14}C	1×10^{-4}
Total		$\sim 7.5 \times 10^{-1}$

Table 10.4: Summation of background components in the energy region 12 keV- 100 keV.

Assuming a background as stated above, with GENINO it would be possible to achieve a mean count rate in the energy region of interest for dark matter search below 100 keV of about 0.8 counts/(kg keV y). This would mean a further reduction of background in comparison to the best measurement obtained with the Heidelberg–Moscow $\beta\beta$ experiment (20 counts/(kg keV y)) by more than one order of magnitude.

In figure 10.4 the spectra of the individual contributions and the summed total background spectrum are shown. As mentioned before, the low energy spectrum is dominated by events originating from the steel of the tank vessel, from the natural radioactivity of the Gran Sasso rock, from the shielding material and from the cosmogenic activations of the Ge-crystals. The above count rates were obtained for a tank diameter of 5 meter and a lead shield thickness of 30 cm. While a lead shield of 25 cm would still be feasible, a tank diameter
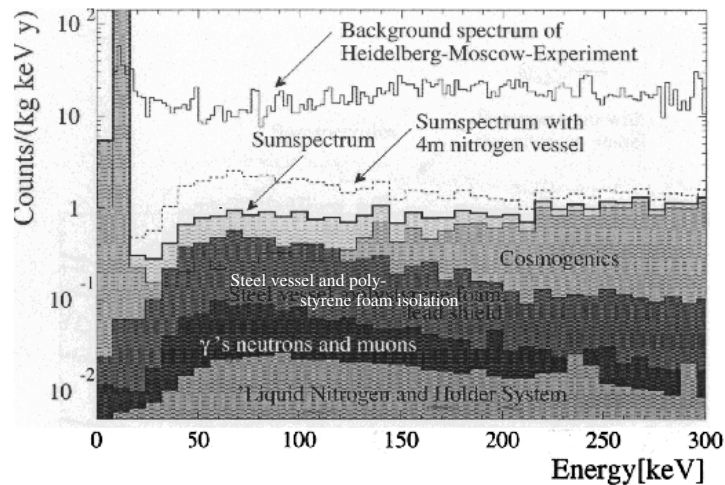
Figure 10.4: Simulated spectra of the dominant background sources for a nitrogen tank of 5 m diameter. Shown are the contributions from the tank walls, the detector holder system, from neutron capture in the nitrogen, from natural radioactivity and from the ^{222}Rn contamination of the nitrogen. The solid line represents the sum spectrum of all the simulated components. The dashed line corresponds to the expectation for a geometry of the tank with 4 m diameter.

of 4 m would be problematic since the count rate of the steel vessel would be by far dominating the background. Consequently a dimension of 5 m for the inner steel vessel in diameter and height is proposed.

10.2   Argon as an alternative to liquid nitrogen cooling

It has been considered before to install the GENIUS experiment with liquid argon (or Xenon) cooling instead of nitrogen [Hel97]. The clear advantage of liquid argon is its higher density. The size of the experiment could be reduced by a factor of approximately two by using argon instead of liquid nitrogen as the cooling medium.

However the problem arises that in the liquid argon the isotopes ^{39}Ar and ^{42}Ar will be present, resulting in a higher count rate in the low energy spectrum due to their decays.

^{39}Ar and ^{42}Ar are β emitters with Q-values of 565 keV and 600 keV, respectively. The half lifes are of $T_{1/2}$=269 years for ^{39}Ar and $T_{1/2}$=33 years for ^{42}Ar.

^{39}Ar decays with 100% probability into the ground state of the stable isotope ^{39}K. Thus no additional gammas are emitted. Also ^{42}Ar decays into the ground state of ^{42}K with 100% probability, however, ^{42}K is a β-emitter with a half life of 12.36 hours and a Q-value of 3.525 MeV. With 17.64% this isotope decays into an excited state of ^{42}Ca, thus being accompanied by the emission of a 1524.7 keV γ [Fir96].

Although it has been argued in [Hel97] that argon is not an alternative to liquid nitrogen as a shield due to these isotopes, the influence of ^{39}Ar and ^{42}Ar

Isotope	contamination	Number of atoms in tank
^{39}Ar	3.5×10^{-21}	4.3×10^9
^{42}Ar	7.4×10^{-22}	9.1×10^8

Table 10.5: Contaminations of liquid argon with the isotopes ^{39}Ar and ^{42}Ar.

has not been studied yet in detail.

In the light of installing a smaller scale test experiment before the full scale setup, it could be considered to use argon as cooling and shielding shielding in this step. For this reason the argon contribution to the low energy background spectrum has been simulated. In this section the results are discussed and the sensitivity obtainable with such a setup is explored.

10.2.1   Simulation of argon contribution

For the simulation of the effect of ^{39}Ar and ^{42}Ar the tank geometry of the GENINO simulation has been used (see figure 10.1). The content of the vessel has been changed from liquid nitrogen to argon in the simulation. $N_{sim}=10^8$ decays of each, ^{39}Ar and ^{42}Ar, were started randomly distributed from inside the tank volume. For the abundances of the isotopes, estimates from measurements of the ICARUS collaboration [Cem95] were taken. The simulated spectrum has to be scaled with the factor

$$\Sigma = \frac{ln2 \times N_A \times \rho_{Ar} \times c}{M_{Ar} \times T_{1/2} \times N_{sim} \times M_{det}}, \tag{10.1}$$

using the values listed in table 10.5 for the contamination and where $\rho_{Ar}=1.63$ g/cm^3 is the density of liquid argon, N_A is the Avogadro number, c is the contamination with the isotope, $M_{Ar}=39.948$ g/mole is the mole mass of argon and $M_{det}=100$ kg is the mass of the simulated detectors.
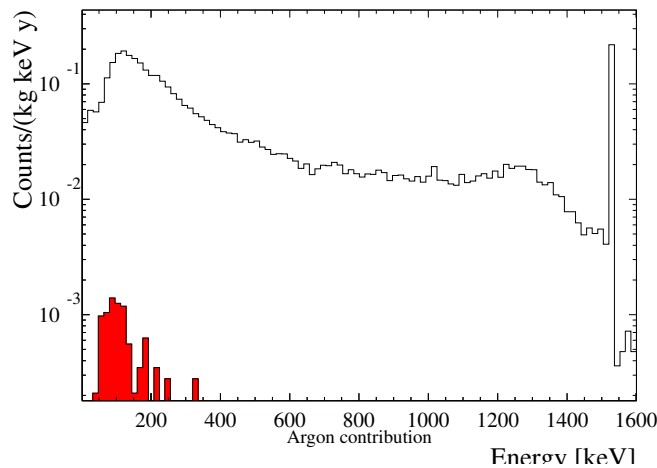

Figure 10.5: Contribution of ^{39}Ar and ^{42}Ar to the background. The open spectrum corresponds to the ^{42}Ar signal, whereas the filled spectrum results from ^{39}Ar.

The resulting spectrum is seen in figure 10.5. The main effect results from the decay of ^{42}Ar. As seen from this figure the count rate resulting from the ^{42}Ar decay would limit the attainable sensitivity of such a setup. The minimum attainable count-rate would be around 0.1   counts/(kg keV y)in the low energy region below 100 KeV. Using argon instead of liquid nitrogen as a cooling medium for the GENINO proposal could thus improve the sensitivity of this setup by approximately one order of magnitude. This sensitivity level would however be the final attainable one. Argon is considerably more expensive as liquid nitrogen and some research and development would still have to be done considering argon cooling of naked HPGe crystals. Thus this option does not seem very attractive as an intermediate step, despite the possibility to increase the sensitivity by one order of magnitude.

10.3 The BARGEIN Box Arrangement

As discussed in the previous section, it makes sense to first investigate the long term feasibility of the technical concept of the Genius proposal while still gathering relevant data for dark matter search before installing the full scale GENIUS experiment. The GENINO proposal manages to substantially reduce the size of the setup (by 50 %) while still improving the sensitivity of the experiment by more than one order of magnitude with respect to the Heidelberg-Moscow experiment. GENINO would be sensitive to both, signal and signature of the claimed DAMA evidence for WIMP dark matter [Kla00a]. Although this smaller scale setup could later be recycled for the installation of the Genius experiment, the effort for construction of such an experiment would not substantially differ from the installation of the full scale experiment, both, technically and concerning money. Therefore it seems reasonable to think about alternative solutions.

Here it is proposed to install a detector setup on a very small scale using the same technical conceptual idea of operating 'naked' HPGe detectors directly in liquid nitrogen as in the GENIUS proposal. However, the idea to use the cooling medium of the HPGe crystals, liquid nitrogen, as the shield against external radioactivity is given up since this step blows up the scale of the experiment. It is shown here that nevertheless such a study using a conventional shield can be sensitive in the range of the DAMA result [Ber00b] even on a short time scale [Maj00a, Maj00c, Maj00d]. In the following section the basic idea is described and discussed in detail, introducing the BARGEIN concept.

10.3.1 The basic concept

The idea for this Box ARrangement of GErmanium in liquid Nitrogen (BARGEIN) grew from the consideration that a technical study on the long term stability of the new detector design should be completed within the shortest possible time scale. The basic concept was, to build up the test setup with material already owned by the Heidelberg-Moscow collaboration. This would significantly reduce the cost and time factor of such an experiment. In addition the setup should be able to provide relevant physical data.

The conceptual design proposed here and depicted in figure 10.6 is based on a dewar made from low activity polystyrene and on a shield of zone refined germanium bricks inside the dewar and low activity lead outside the dewar. A layer of boron loaded polyethylene plates for suppression of neutron induced background completes the shield [Maj00a].

The polystyrene dewar serves also as a support for the roof shield so that no other less radio-pure structure material is needed. As a backup solution a copper plate could be used to support the upper shielding lead.

Polystyrene as dewar material has the following advantages:

- low specific radioactive contamination (see below, table 10.7).

- good insulation properties and low density, so that even a rather thick dewar wall for low evaporation of the purified liquid nitrogen has little mass in respect of radiopurity.

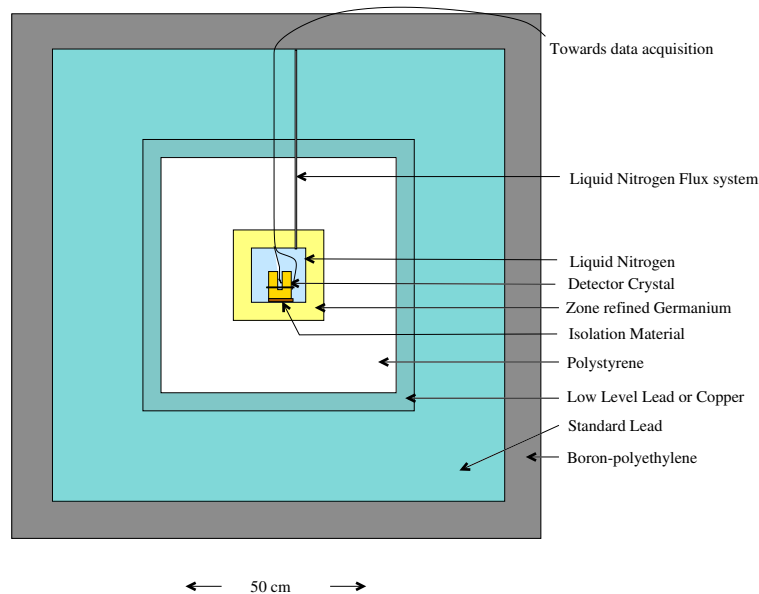- low cost for the construction of the dewar box.

Figure 10.6: Design of the BARGEIN setup. The High-purity Germanium Crystal is located inside a polystyrene box which is serving as the liquid nitrogen dewar. To minimize the influence of the polystyrene impurities, an additional inner shielding layer of zone-refined Germanium is used. The box is surrounded by a subsequent layer of low-level lead.

The Heidelberg-Moscow collaboration possesses $\sim$340 kg of zone-refined high-purity Germanium bricks which could serve as the inner layer to shield the 'naked' HPGe detector against the less radio-pure polystyrene. Due to the restrictions on the background also the first 5cm layer outside the polystyrene-dewar needs to be of extreme radiopurity. The same LC2 lead or low-level copper as installed in the Heidelberg-Moscow experiment or the ancient lead discussed below could be used. To shield the external γ (natural radioactivity from the surroundings) an overall lead layer of approximately 35 cm is needed.

With a wall thickness of 20cm of the polystyrene-box the liquid nitrogen content would evaporate within approximately 15 hours. The loss will be compensated from an external supply system.

10.3.2   Background considerations and simulations

To study the attainable sensitivity of this detector design, the radiopurities of all the used materials have to be known. The main goal of the BARGEIN experiment is to lower the background of the Heidelberg-Moscow experiment by another order of magnitude to $\sim$ 2 counts/(keV kg y) in the energy region below 100 keV.

Internal activities of the HPGe-crystal

The internal activities of the detector crystals from activation through cosmic rays on ground level have been estimated using the Σ program [Boc94, Kla98a]. It is evident from these considerations that a suppression of the ^{68}Ge and other cosmogenically produced activities is essential. This can either be achieved by

underground production or by deactivation of the crystal deep underground. Two HPGe-detectors which are operated in the Gran-Sasso Underground Laboratory since 1992 could be used for the first stage of this project. They could be removed from their cryostat system in the underground and placed in the new liquid nitrogen surrounding.

The contacting material and liquid nitrogen

The new detector design developed in the course of this thesis and discussed in chapter 9.2 reduces drastically the amount of material used for contacts. Selected low-level steel with an impurity of $< 10^{-7}$ g/g Uranium and Thorium (Borexino measured 10^{-9}g/g [BOR98]) makes its background contribution negligible. According to the simulations the effect of impurities of the liquid nitrogen is also negligible provided that a purity level of $< 10^{-14}$g/g for U/Th and a corresponding ^{222}Rn contamination could be reached. Even better standards have been achieved by the Borexino collaboration for purified water. This well supported estimation has been discussed in [Bau98c]. ^{222}Rn can be strongly reduced by charcoal column adsorption from liquid nitrogen [Heu00].

Polystyrene

The only so far unknown component in the proposed setup is the polystyrene material for the dewar box. In order to estimate the purity of this material 3 kg of raw polystyrene granulate in a low-level germanium-spectrometer at the Gran-Sasso underground laboratory were measured. This material measurement was following a measurement of background only. The intrinsic background of the polystyrene measurement can in principle be substracted resulting in a spectrum being due to the polystyrene contaminations.

The same detector Nat2 has been used as in [Maj98] for a previous material measurement. The geometry of the lead box and the detector itself remained unchanged in both, simulation and measurement with respect to the earlier ones. For the background measurement however the inner lead layer was changed. It has been replaced with ancient lead which had been stored under water in a sunken ship for approximately 400 years.

The polystyrene granulate inside a vacuum tight plastic bag was tightly pressed to the detector cap from above, trying to maximize the counting efficiency by supplying a large angular coverage of the detector for the material measurement (see figure 10.7 for a schematic view). The exact positioning of the bag could not exactly be reproduced in the simulation thus entering the analysis as a systematic error.

For the calculation of the polystyrene impurities only the characteristic peaks of the background measurement have been substracted from the according peaks in the polystyrene measurement. The count rates of the most prominent characteristic peaks obtained like this is shown in table 10.6. The assumption that the excess count rate in the peak is a result of the additional polystyrene in the second measurement is safe since other than the polystyrene probe nothing was changed in the setup. If however additional contaminations not being due to the polystyrene were introduced into the setup, this leads to a systematic overestimation of the polystyrene contamination thus the assumption made is conservative.

The counting efficiency has been estimated using a simulation with the Monte Carlo code GEANT3.21.
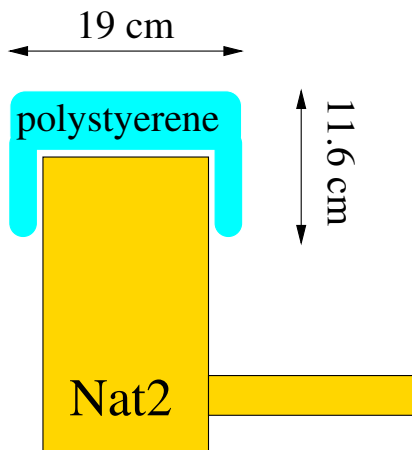

Figure 10.7: Sketch of the detector setup of Nat2 during the polystyrene measurement.

To obtain the systematic uncertainty, simulations of the same setup were carried out, with the geometry of the polystyrene probe changed by enlarging or lowering the angular coverage of the detector while keeping the absolute mass constant. These spectra were then compared to the original one. The systematic error on the efficiencies is inferred to be 15%.

To simulate the counting efficiency for different characteristic peaks of the contaminations, 10^7 decays were started for the U/Th decay chains and for ^{40}K randomly distributed within the polystyrene volume. The detector response was then recorded. The efficiency for a certain characteristic peak is given as the ratio ϵ of started events n_{sim} to the counts seen in the characteristic peak n_{Peak} :

$$\epsilon = \frac{n_{Peak}}{n_{sim}}. \tag{10.2}$$

Once the efficiency for a peak is known, the contamination of the simulated material is calculated through the expression:

$$A = \frac{N_{Peak}}{\epsilon M} = \frac{N_{Peak}\, n_{sim}}{n_{Peak}\, M}, \tag{10.3}$$

where M denotes the mass of the observed material.

The result for the most prominent peaks of the U/Th decay chains as well as for ^{40}K are shown in table 10.6 together with the count rate in the difference spectrum, resulting from the polystyrene contamination.

Assuming the natural decay chains to be in equilibrium, for the ^{238}U chain an activity of $(2.13\pm0.41(\text{stat.})\pm0.27(\text{sys.}))$ mBq/kg, for the ^{232}Th decay chain $(7.3\pm0.58(stat.)\pm0.91(\text{sys.}))$ mBq/kg and for ^{40}K $(8.0\pm3.2(stat.)\pm1.3(\text{sys.}))$ mBq/kg was obtained where for the calculation of the U/Th contaminations the summed count rates of the most prominent peaks in the spectrum resulting from the decay chain have been used (see table 10.6). The comparison of the results obtained from the single peaks within the decay chains are very well consistent within the errors.

Source	Energy [keV]	measured count rate [cpd]	simulated efficiency in promille	contamination [mBq/kg]
^{40}K	1460.0	0.77±0.31	0.37±0.06	**8.02±3.23±1.3** (stat.) (syst.)
^{238}U decay chain	295.2	2.59±0.60	1.55±0.23	6.5±2.4
	351.4	6.58±0.64	2.95±0.44	8.6±2.1
	609.3	4.13±0.64	2.55±0.38	6.2±1.9
	1120.3	1.10±0.34	0.57±0.05	7.4±3.0
^{238}U decay chain combined		14.40±1.14	7.62±0.95	**7.29±0.58±0.91** (stat.) (syst.)
^{232}Th decay chain	238.6	1.64±0.60	4.45±0.67	1.4±0.7
	583.2	1.36±0.45	1.85±0.28	2.8±1.4
	511.0	1.04±0.47	0.65±0.10	6.2±3.7
	911.2	1.42±0.40	1.15±0.20	3.4±2.2
	2614.5	0.07±0.18	0.76±0.11	0.4±1.0
^{232}Th decay chain combined [1]		4.49±0.87	8.21±1.12	**2.11±0.41±0.29** (stat.) (syst.)

Table 10.6: Impurities of the polystyrene granulate seen in the material measurement. Listed are the identified characteristic peaks with their energy, the measured count rate of the peak, its simulated efficiency and the resulting contamination of the polystyrene. Listed is also the contamination with ^{238}U and ^{232}Th obtained from a combined analysis of the peaks.

Although we assume that this is not the ultimate purity reachable since the material used for the measurement was not specially selected or treated for higher purity from dust particles, these values were used in our further analysis. Cleaning the granulate in a dust free area before the production of the polystyrene foam could further reduce radio-impurities of primordial nuclides. Note that for this last step in fabricating the dewar-box only water is needed which can be produced with high radiopurity [BOR98]. Thus hardly any additional materials can enter the polystyrene isolation if care is taken during the production of the foam.

The shielding materials

Another critical component of the setup is the shielding material. In order to reduce the influence of the polystyrene dewar on the background, we plan to shield the crystals with 5cm thick HPGe bricks (see figure 10.6). Even with the most sensitive HPGe detectors their contamination could not yet be measured [Mai95]. Zone-refined Germanium is one of the most radio-pure materials presently obtainable. It is assumed for the following considerations that its activity is in the range of the low-level LC2 lead used in the Heidelberg-Moscow experiment. For the first 5cm of the shield outside the polystyrene dewar box a low-level lead or copper layer will be used. The LC2 lead of the Heidelberg-Moscow experiment has recently been demonstrated to be purer than 10 μBq/kg for the U/Th natural decay chains [Die99]. The activity of ^{210}Pb has been measured to be 0.36 Bq/kg [Mai95].

For the contamination of the ancient lead with ^{210}Pb, the measurement

---

[1] Without 511 keV peak

Material	Source	Activity	Countrate (0 - 100 keV) [counts/(kg keV y)]
Cosmogenic activities in crystal	^{68}Ge ^{63}Ni	0.2 μBq/kg 0.7 μBq/kg	**0.5**
Liquid Nitrogen	^{238}U chain ^{232}Th chain ^{40}K	1.0 μBq/kg 1.0 μBq/kg 1.0 μBq/kg	**<0.2**
zone-refined Germanium bricks	^{238}U chain ^{232}Th chain ^{40}K	3.0 μBq/kg 3.0 μBq/kg 10.0 μBq/kg	**0.6**
polystyrene	^{238}U chain ^{232}Th chain ^{40}K	7.3 mBq/kg 2.13 mBq/kg 8.0 mBq/kg	**2.5-3.5**
LC2 Lead	^{238}U chain ^{232}Th chain ^{210}Pb ^{40}K	10.0 μBq/kg 5.0 μBq/kg 0.36 Bq/kg 100.0 μBq/kg	**1.5**

Table 10.7: List of the background rates expected from the materials of the BARGEIN setup.

mentioned above has been used. To estimate the pollution, the efficiency for detection of the 46.5 keV gamma resulting from the decay of ^{210}Pb has been simulated with GEANT3.21. In the simulation 10^{10} ^{210}Pb decays have been started randomly distributed within the 221.33 kg of ancient lead used in the measurement. The simulated spectrum had 412±23 events in the 46.5 keV peak leading to an efficiency of $\epsilon_{^{210}Pb}=(4.1\pm0.2)\times10^{-8}$. Using equation (10.3) with a count rate of 0.43±0.08 in the 46.5 keV peak of the experimental spectrum, this leads to a ^{210}Pb contamination of A=0.55±0.13Bq/kg of the ancient lead. This is approximately the same level as measured for the LC2 lead mentioned above.

Contributions from the surroundings

From considerations of the measured background gamma flux inside the Gran Sasso underground laboratory [BOR98] and from experience made by the Heidel-berg-Moscow experiment it is evident that a layer of 35 cm lead is sufficient to reduce the natural γ flux to an insignificant level [Gue97]. The effect of the neutrons [Bel89] has been shown to be sufficiently reduced by 20 cm of boron-loaded polyethylene [Gue97].

Monte Carlo Simulations

With these data detailed a Monte Carlo simulation of the proposed setup using the GEANT3.21 package [GEANT] was performed. The used purity levels of the various materials and the resulting expected rates in the energy region below 100 keV are listed in table 10.7. The resulting spectrum is shown in figure10.8. Below 100 keV an average countrate of ~3-6 counts/(kg keV y) is expected. For the energy spectrum around the Q-value of the double-beta decay (2038 keV), the expected count rate is about 0.1 counts/(kg keV y).
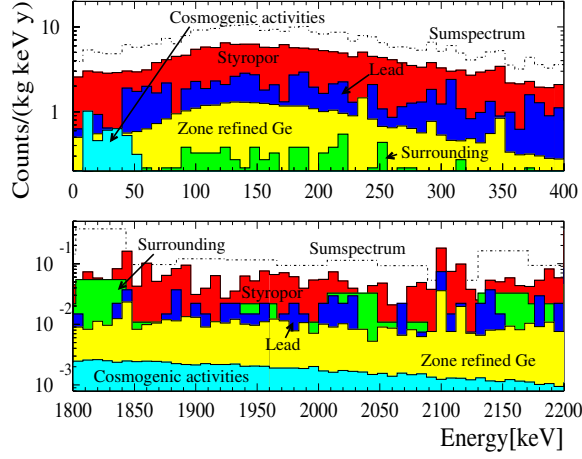
Figure 10.8: Simulated background spectrum of the BARGEIN setup in the interesting energy regions. Upper spectrum: Low Energy region interesting for dark matter search. The largest contribution is expected from the impurities of polystyrene (see text). Lower spectrum: Energy region relevant for the search for neutrinoless double-beta decay. According to the simulations a background of ~0.1 counts/(kg keV y) can be reached.
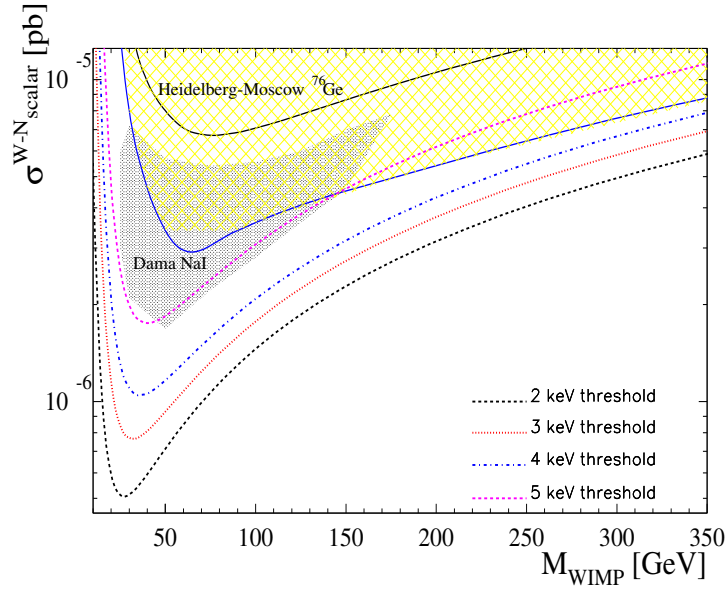
Figure 10.9: Exclusion plot for spin independent WIMP-nucleon elastic scattering cross section as a function of the WIMP mass. The exclusion curves (90 % C.L.) have been obtained by using the analysis parameters of [Hei98] and the simulated spectrum from figure 10.8. Different thresholds have been assumed. Already with a 5 keV threshold the whole evidence contour for WIMPs claimed by the DAMA collaboration [Ber00a] (shaded area) can be tested. The present limits given by the DAMA 100 kg NaI experiment [Ber98] and the limit from the Heidelberg-Moscow experiment [Hei98] are also shown.

10.3.3 Sensitivity

The spectrum obtained from the Monte-Carlo simulation was used to deduce the sensitivity of the proposed setup for WIMP dark matter search and for neutrinoless double-beta-decay.

Dark matter search with BARGEIN

The spectrum shown in figure 10.8 was used to obtain the exclusion plots for elastic spin-independent WIMP-nucleon scattering cross sections given in figure 10.9. Standard values for WIMP parameters [Hei98] as well as varying thresholds have been assumed for the analysis. It is evident from figure 10.9 that the resulting exclusion plots are very sensitive on the achieved threshold of the detector. A threshold of 5 keV would allow to test the full claimed range of the DAMA experiment [Ber00b] within a running time of two years.

BARGEIN and the neutrinoless double-beta decay

It can be considered to use the detectors of the Heidelberg–Moscow $\beta\beta$ experiment enriched with up to 86% with ^{76}Ge for the seach of neutrinoless double beta decay. A background as low as 0.1 counts/(kg keV y) in the energy region relevant for the detection of neutrinoless double-beta decay (2038 keV) is expected using the new setup. A further reduction by pulse shape analysis will result in about 0.03 counts/(kg keV y) (see chapter 6 and [Maj99, Hei99]). This corresponds to a reduction compared to the present background level of the Heidelberg-Moscow experiment by a factor of two [Hei99]. Note that for this analysis different values for the cosmogenic activation of the detectors due to the different detector material (^{76}Ge) have to be taken into account. A sensitivity for the lifetime of $\sim 2.5 \times 10^{25}$y can be reached.

Chapter 11

Outlook: The GENIUS Test Facility (TF)

This chapter gives an outlook into the near future and describes the GENIUS Test Facility, a setup derived from the BARGEIN idea. This experiment will be installed in the Gran Sasso underground laboratory in the near future as a first step towards the realization of the GENIUS experiment.

11.1 Enlarging the box setup

Despite the favorable quality of the BARGEIN proposal concerning cost and time, it should also be considered to use such a setup for a wider variety of applications.

It has been shown in the previous chapter that with a setup using a conventional shield, a sensitivity can be reached which allows for a test of the DAMA evidence region within a short time period [Maj00a]. However, with the BARGEIN setup this test could only be done looking for the expected signal of WIMP dark matter in HPGe detectors: the WIMP-nucleus recoil spectrum. Thus the BARGEIN setup can only verify the CDMS result of excluding the possibility of WIMP dark matter as favored by the DAMA data [Abu00]. If the active mass of the detector can be increased to approximately 40 kg and the background index as discussed in the earlier section can be maintained also the expected signature of WIMP dark matter in form of the annual modulation signal could be tested within a reasonable time window [Kla00d, Maj00c, Maj00d].

For the GENIUS experiment it is furthermore of utmost importance to produce and store the HPGe detectors underground very soon in order to give the germanium crystals time to deactivate from cosmogenically produced materials. It therefore has to be carefully considered to enlarge the above discussed setup in order to be able to house as much detector material as possible inside the polystyrene dewar. Also the possibility of constructing a holder system for a large array of detectors out of a very small amount of sufficiently radio-pure material has yet to be shown.

With the proposed Genius Test-Facility we could test all the mentioned points: the long term stability of 'naked' HPGe-detectors in liquid nitrogen, the possibility of constructing a feasible holder system and in addition the DAMA

evidence contour, through testing the expected signal and signature. In addition we will be able to set more stringent bounds on the radiopurity of liquid nitrogen being an important requirement for the realization of the GENIUS-project. The GENIUS-TF will also be a suitable place to develop and test the electronics needed for the GENIUS experiment. It is of great importance to carefully design and develop a data acquisition system which is based on a modular structure being capable of taking data from up to 300 detectors simultaneously.

11.2 The Test Facility

The concept of the GENIUS proposal has the great advantage that no individual cryostat system is needed. Instead the HPGe crystals are surrounded by liquid nitrogen of much higher radiopurity which in addition provides ideal cooling and shielding against external radiation. This opens the new research potentials for the Genius project [Kla98a, Kla98b].

It is proposed here to install a setup with up to fourteen detectors on a small scale in order to be sensitive in the range of the DAMA result [Bel00] on a short time scale and to prove the long term stability of the new detector concept.

The design is shown in figure 11.1. It is based on a dewar made from low activity polystyrene and on a shield of zone refined germanium bricks inside the dewar and low activity lead outside the dewar. A layer of boron loaded polyethylene plates for suppression of neutron induced background completes the shield.
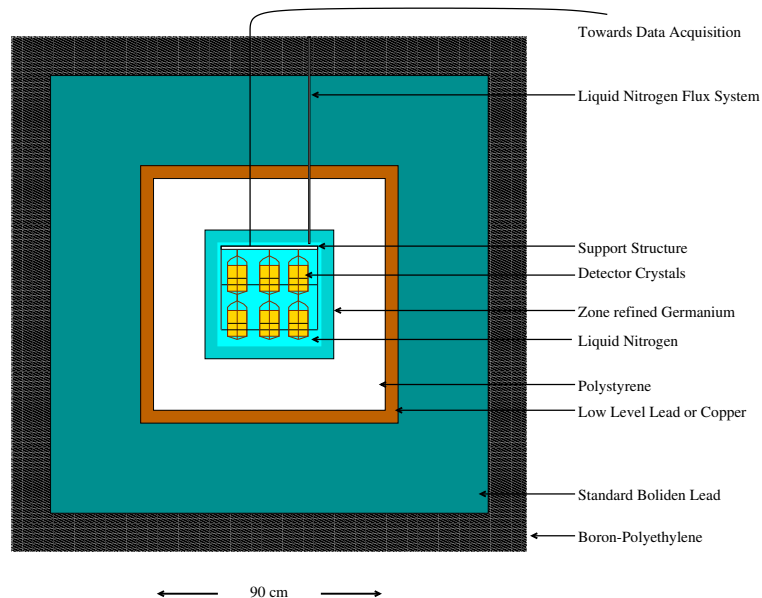
Figure 11.1: Conceptual design of the Genius TF. Up to 14 detectors will be housed in the inner detector chamber, filled with liquid nitrogen. As a first shield 5 cm of zone refined Germanium will be used. Behind the 20 cm of polystyrene isolation another 35 cm of low level lead and a 15 cm borated polyethylene shield will complete the setup.

340 kg of zone-refined high-purity Germanium bricks would serve as the inner layer to shield the 'naked' HPGe detector against the less radio-pure polystyrene.

Also the first 5cm layer outside the polystyrene-dewar needs to be of extreme radiopurity. The same type of copper as installed in the Heidelberg-Moscow experiment, and/or some complementary low-level lead could be used. To shield the external γ rays (natural radioactivity from the surroundings) an overall lead layer of approximately 35 cm is needed.

Using this concept an inner detector chamber of 40 cm×40 cm×40 cm would be sufficient to house up to seven HPGe-detectors in one layer or 14 detectors in two layers. This will allow for the development and test of a holder system for the same amount of crystals.

The overall dimension of the experiment will be 1.8 m×1.8 m×1.8 m thus fitting in one of the buildings of the Heidelberg–Moscow $\beta\beta$ experiment which is used momentarily for material measurements.

The background considerations and simulations discussed in the previous chapter and in [Maj00a] suggest that a reduction of the background by a factor of ∼4 with respect to the Heidelberg-Moscow-Experiment can be attained with the proposed setup. The only difference of the Genius TF with respect to BARGEIN is the larger detector chamber and the fact that freshly produced HPGe detectors will be used. Since no additional material is introduced (except for the very radio-pure HPGe detectors themselves), it is safe to estimate the expected background index of the Genius TF using the simulations made for the BARGEIN proposal (chapter 10.3 and [Maj00a]). If the two (or one of the two) natural germanium detectors stored in the Gran Sasso underground laboratory since 1992 are also used for the Genius TF, the same sensitivity on the WIMP nuclear recoil spectrum can be reached as derived before.

For the new detectors the production history has to be taken into account. Since they will not have the time to get deactivated from cosmogenic isotopes like ^{68}Ge the threshold of these detectors will be considerably higher, around 12 keV. The expected contamination of these detectors would be the same as assumed for the GENINO proposal seen in table 10.3 for a production without additional shield.

The Genius TF will also in this sense be a very important test setup since it will be able to check the prediction of the cosmogenic isotope production rates and make reliable statements on the final background level of the GENIUS experiment resulting from these isotopes. Furthermore the logistic needed for the optimal production and transportation time of the HPGe detectors can be explored.

Assuming a final target mass of 40 kg, an energy threshold of 12 keV and a background index of 4 counts/(kg keV y) corresponding to ∼ 0.01 counts/(kg keV d) in the energy region between 12 keV and 100 keV the Genius TF would need a significance of 190 kg y to see the claimed DAMA annual modulation with 95% probability and 90%C.L. (see [Ceb99]). This corresponds to an overall measuring time of approximately five years which would correspond to the life time of this experiment.

However, as reported by Perkin Elmer, the new detectors will have an energy threshold of 0.7 keV [San00] thus allowing for the use of the experimental spectrum in the energy range between the threshold and the X-ray peaks seen from the cosmogenically produced isotopes. This could significantly improve the sensitivity of the Genius TF on the annual modulation effect. Details on this topic still have to be worked out in the near future.

11.2.1   Evaporation of liquid nitrogen

In order to get a feeling for the amount of liquid nitrogen which has to be refilled to the dewar box, the evaporation rate has to be estimated. It can be calculated from the equation for energy loss through materials:

$$\frac{dE}{dt} = P = \Lambda \times \Delta T \times \frac{\mathcal{O}}{x}, \tag{11.1}$$

where ΔT is the temperature difference between the cooling medium and the surrounding, $\mathcal{O}$ is the inside surface of the dewar box, through which energy can escape and x is the thickness of the polystyrene wall. Λ is the heat conductivity corresponding to $\Lambda_{polys} \sim 35 \times 10^{-3} \; J/(s \; m \; K)$ for polystyrene. Note however that this is an approximate value only. The exact value depends on the production history of the polystyrene foam and can vary significantly.

For the Genius TF the inside surface would be around 6×50 cm $\times 50$ cm $= 1.5 \; m^2$. The wall thickness of the dewar $x = 20$ cm and the temperature difference between the liquid nitrogen inside the dewar and the surrounding of $\Delta T \sim 297 \; K - 77 \; K{=}220 \; K$.

Once the evaporation energy of the material is known, the evaporated volume can easily be calculated:

$$V = \frac{P}{H_N}[mol/s] = \frac{\Lambda \times \Delta T \times \mathcal{O} \times M_N}{H_N \times \rho_N \times x}[m^3/s]. \tag{11.2}$$

Here M_N and ρ_N are the Mole number and the density of liquid nitrogen respectively. For liquid nitrogen the specific evaporation energy is $H_N = 2790$ J/mole.

Plugging in the numbers yields: $V = 3.59 \times 10^{-4}$ l/s$=30.99$ l/day for the Genius TF.

To check this result independently and to get a feeling for the amount of nitrogen needed to first cooling down the material inside the dewar (zone refined germanium bricks) and filling it, a polystyrene box with the geometry of the planned Genius TF dewar was constructed and filled with liquid nitrogen. The inside of the dewar box was mantled with a 5 cm lead layer prior to filling the nitrogen into the box. The inside volume left was ~ 65 l.

Approximately 50 l of liquid nitrogen were needed for cooling the interior of the bof before the dewar would keep nitrogen in its liquid form. There were no problems to fill up the dewar, once the inside temperature of the box was low enough. The amount of evaporated nitrogen was then measured. The result is $V_T{=}21.6{\pm}0.5$ l/day. This is by 50 % less than the calculated value which is most probably due to the inaccurately know value for the heat conductivity of the used polystyrene foam.

11.2.2   Installation of the Genius TF

With the dimensions for the inner detector chamber given above, the materials shown in table 11.1 will be neede for the installation of the GENIUS-TF.

The Heidelberg-Moscow-Collaboration possesses ~ 330 kg of zone refined Germanium bricks, ~ 10 tons of Boliden-lead and ~ 500 kg ancient low level lead. These materials can be installed in the GENIUS-TF without any additional costs.

Material	Amount
14 HPGe-detectors	$\sim$ 40 kg
Electronics	—
Germanium bricks[2]	$\sim$ 330 kg
Polystyrene box	$\sim$ 40 kg
Low Level Lead (LC2 or ancient)	3076 kg
Low Level Copper	2428 kg
Boliden Lead bricks	35.14 t
Nitrogen filling and cleaning device	3-4 100 liter low level dewars

Table 11.1: Amount of materials needed for the installation of the GENIUS-TF.

The Borexino collaboration is running a liquid nitrogen filtering device in the Gran Sasso underground laboratory. The capacity of this machine is by far not used by the needs of the Borexino collaboration. Thus this device could also serve as the low level nitrogen support for the Genius TF. Once a week two 100 liter low level nitrogen dewars could be filled from the filtering device and stored for deactivation of ^{222}Rn for one week. This amount of liquid nitrogen would be enough for approximately one week.
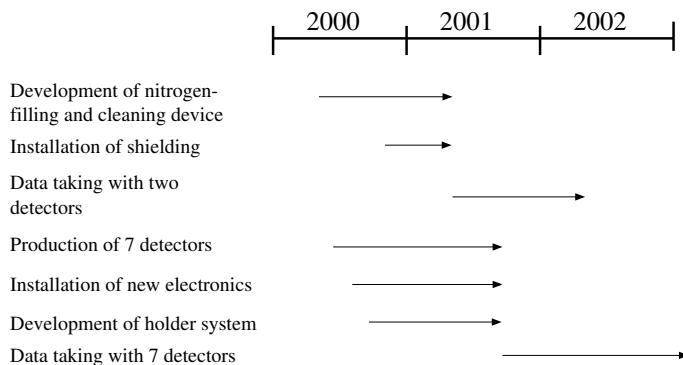
Figure 11.2: Time schedule for the GENIUS-TF.

11.2.3 Time Schedule

The time schedule of the GENIUS-TF is shown in figure 11.2. The development of the liquid nitrogen cleaning and filling device should be started soon in collaboration with the Borexino experiment. The construction of the setup can be started immediately since no additional space in the Gran Sasso Underground Laboratory is required. The data acquisition system of the HDMS experiment can be used to obtain first data with two detectors which are already housed in the Gran Sasso Underground Laboratory. The first results can be expected in the end of the year 2001 already.

---

[2]Property of the Heidelberg-Moscow-Collaboration

Chapter 12

Summary and Conclusion

The focus of this thesis is on WIMP dark matter search and the search for neutrinoless double beta decay using HPGe detectors.

A great part of the thesis concentrates on the present experimental effort to improve the sensitivities of the Heidelberg–Moscow $\beta\beta$ experiment and the HDMS experiment.

The Heidelberg Moscow experiment is presently the most sensitive experiment looking for neutrinoless double beta decay (see figure 4.2). Its present status is discussed in chapter 5.1.

Already since 1995 a digital pulse shape analysis has been applied to the data of the Heidelberg–Moscow $\beta\beta$ experiment in order to reject the background in the interesting energy region around the Q-value of the double beta decay [Hei97, Hel00]. The sensitivity for neutrinoless double beta decay was considerably increased using this method. In the course of this thesis a new method was developed which allows to do the background recognition through Pulse Shape Analysis (PSA) with a high efficiency. Some assumptions made for the previous method could be abandoned. The new method is based on the application of neural networks.

As an application of the PSA with neural networks this new procedure was then applied to the data of the Heidelberg–Moscow $\beta\beta$ experiment. For this purpose a new, completely independent analysis code was written. This data analysis has some advantages with respect to the old code and therefore reduces the background of the Heidelberg–Moscow $\beta\beta$ experiment in the energy region of the Q-value of double beta decay by another 10% with respect to the old evaluation. The reason for this further decrease of the background index is that so far the coincident events which occured in two or more detectors simultaneously have not been rejected. The procedure is described in detail in chapter 7.

As a result of this work a new lower limit on the half life of neutrinoless double beta decay can be derived:

$$T_{1/2}^{0\nu\beta\beta} \geq 2.1 \times 10^{25} \text{ yr} \quad 90\% C.L., \tag{12.1}$$

$$T_{1/2}^{0\nu\beta\beta} \geq 3.5 \times 10^{25} \text{ yr} \quad 68\% C.L., \tag{12.2}$$

which can be converted into an upper limit of the effective Majorana neutrino

mass (using the matrix elements from [Sta90]):

$$< m_\nu > \quad \leq \quad 0.34 \ eV \quad 90\% \ C.L., \tag{12.3}$$

$$< m_\nu > \quad \leq \quad 0.26 \ eV \quad 68\% \ C.L. \ . \tag{12.4}$$

The Heidelberg Dark Matter Search (HDMS) experiment is designed to look for WIMP dark matter using a special detector design to efficiently suppress multiple scattered events in the low energy region. The performance of the prototype detector which was successfully running for 15 months in the Gran Sasso underground laboratory is shortly summarized and an exclusion limit on the WIMP-nucleon cross section as a function of the WIMP mass was derived (see figure 8.4). Already the prototype of the HDMS experiment is comparable in sensitivity to the presently most sensitive experiments.

The final setup of the HDMS experiment was assembled in February 2000 at Perkin Elmer, Oak Ridge, Tennessee, USA and transported to the Gran Sasso underground laboratory in August 2000.

The performance of the detector in its final configuration is investigated and as a result of this work the first analysis of the background spectrum is obtained.

The last part of the thesis deals with the future development of the search for rare events using HPGe detector configurations.

For The GENIUS proposal which aims for a reduction of background by three to four orders of magnitudes with respect to the Heidelberg–Moscow $\beta\beta$ experiment new considerations on the cosmogenic production of ^{3}H are made. As a result it can be stated that detector production for the GENIUS experiment has to be done using great care concerning the cosmic ray induced production of isotopes. Especially tritium will limit the final reachable sensitivity of the GENIUS experiment if the detectors are not produced directly underground. Furthermore it is shown that GENIUS could be built in any underground laboratory with comparable natural radioactivity as at Gran Sasso and with a shielding overburden of more than 2000 mwe.

For the first step towards the realization of the GENIUS project several experimental setups are proposed.

The GENINO proposal which was introduced in the course of this setup is designed to reduce the size of the experiment by up to 50% with respect to the full scale GENIUS setup. The concept is based on the idea to replace the liquid nitrogen shield partly by a conventional low level lead shield. It is shown here using detailed simulations and considerations of the background that the sensitivity of this setup would be good enough to allow for a test of the DAMA evidence for WIMP dark matter [Ber00b] using the WIMP-nucleon recoil spectrum and the annual modulation effect simultaneously. However, it is clear that no reduction of cost could be achieved with the GENINO experiment with respect to the full scale GENIUS experiment.

As an alternative approach the BARGEIN setup is therefore suggested here which completely abandons the idea of using the liquid nitrogen as a shield against external radioactivity, but still makes use of the detector technique of 'naked' HPGe detectors operated directly in liquid nitrogen, as developed for the GENIUS experiment. The idea is to use a polystyrene dewar for the liquid nitrogen and detector storage in connection with a conventional shield against external radioactivity. As detectors for this setup it is suggested to use one of the natural germanium crystals stored underground since 1992 at the Gran Sasso

laboratory. This would have the advantage of a very low intrinsic radioactivity due to cosmogenically produced isotopes. It is shown in simulations that this BARGEIN setup could reach a background index comparable or even better than the Heidelberg–Moscow $\beta\beta$ experiment thus reaching a sensitivity which would allow to test the DAMA evidence region using the WIMP-nuclear recoil spectrum due to the better obtainable energy threshold. Hardly any material would be needed for this setup, thus having a very low cost factor for this experiment.

As an extension it is finally suggested to enlarge the BARGEIN setup in order to have space to house up to 40 kg of detector material in its detector chamber. This will allow for a direct test of the DAMA evidence through the annual modulation effect and the WIMP-nuclear recoil spectrum simultaneously. The installation of the Genius TF in the Gran Sasso underground laboratory will be started soon with the first data expected at the end of the year 2001 already.

As a conclusion it can be stated that present experiments using the conventional HPGe detector technique to look for rare events will reach their limit on sensitivity in the next decade.

Using the new data analysis and the new PSA method based on neural networks developed in the course of this thesis it succeeded to further decrease the background and thus improve the limits derived from the data of the Heidelberg–Moscow $\beta\beta$ experiment.

Two steps are due in the near future concerning the search for WIMP dark matter and the neutrinoless double beta decay. First the claimed positive evidence for WIMP dark matter from the DAMA experiment has to be tested, thus confirmed or rejected. As a second step a larger increase in improvement of sensitivity is due enabling the test of large parts of theoretical predictions concerning WIMP dark matter and to give stringent constraints on the neutrino mass spectrum. It was shown in this thesis how this could be done in the future.

To test the DAMA evidence, the HDMS experiment could contribute by testing the predicted WIMP-nuclear recoil spectrum making use of conventionally operated HPGe detectors. The Genius TF could finally test both, the signal and the signature in form of the annual modulation effect. This setup which has been proposed for the first time here will be an important step forward since it will be the first proof of the long term feasibility of the new detector concept. It will collect data which is relevant for modern physics. The preparations of installation of the Genius TF are presently beginning. The first data from this experiment is already expected for the end of the year 2001. It should be noted that GENIUS, the Genius TF and DAMA are the only experiments being sensitive to the WIMP nuclear recoil signal and the annual modulation signature simultaneously expected by the claimed positive DAMA WIMP evidence. The Genius TF will be the first step towards the realization of the GENIUS experiment thus preparing the second step, the large improvement of sensitivity to rare events, from which it is hoped to gain important information on the composition of our universe.

Bibliography

[Abd00] J.N. Abdurashitov et al., Yad. Fiz. **63**(2000)1019

[Abu00] CDMS Collaboration, R. Abusaidi et al. Nucl.Instrum.Meth. A **444**(2000)345, Phys.Rev.Lett. **84**(2000)5699 and astro-ph/0002471

[AGL89] M. Aglietta et al., Il Nuovo Cimento C **12**(1989)467

[Agl99] M. Aglietta et al., LVD Collaboration, hep-ex/9905047

[Alc98] C. Alcock et al., Astro. Phys. J. Letters **499**(1998)L9

[Ale97] A. Alessandrello et al., Phys. Lett. B **408**(1997)465

[All98] A. Alessadrello et al., Phys. Lett. B **433**, 156-162 (1998).

[Arn98] R. Arnold et al., Nucl. Phys. A**636**(1998)209

[Arn00a] R.Arnowitt, B. Dutta and Y. Santoso, hep-ph/0008336

[Arn00b] R.Arnowitt, B. Dutta and Y. Santoso, hep-ph/0008320

[Arp92] C. Arpesella, Nucl. Phys (Proc. Suppl.) A **28**(1992)420

[Art95] G. Artemiev et al., Proc. XXVII Conf. on High Energy Phys., Glasgow, 1994

[Ath99] C. Athanassopoulos et al., Phys. Rev. Lett. **81**(1998)1774

[Avi92] F.T. Avignone, et al., Nucl. Phys. B(Prc. Suppl.) **28**(1992)280

[Bau97] L. Baudis, J. Hellmig, H.V. Klapdor-Kleingrothaus, A. Müller, F. Petry, Y. Ramachers, Nucl. Inst. and Meth. A **385**(1997)265

[Bau98a] L. Baudis, J. Hellmig, H.V. Klapdor-Kleingrothaus, B. Majorovits, Y. Ramachers, H. Strecker, Internal Report, Proposal MPI H-V2-1998

[Bau98c] L. Baudis, G. Heusser, H.V. Klapdor-Kleingrothaus, B. Majorovits, Y. Ramachers, H. Strecker, Nucl. Inst. and Meth. A **426**(1999)425

[Bau99] L. Baudis, PhD thesis, University of Heidelberg, 1999

[Bau00] L. Baudis, A. Dietz, B. Majorovits, F. Schwamm, H. Strecker, H.V. Klapdor-Kleingrothaus, in press at Phys. Rev. D, astro-ph/0008339

[Bed94] V. Bednyakov, H.V. Klapdor-Kleingrothaus, S.G. Kovalenko, Phys. Rev. D **50**(1994)7128

[Bed97] V. Bednyakov, S.G. Kovalenko, H.V. Klapdor-KleingrothausY. Ra-machers, Z. Phys. A **357**(1997)339 and hep-ph/9606261

[Bed00a] V. Bednyakov, H.V. Klapdor-Kleingrothaus, Phys. Rev. D **62**(2000)043524 and hep-ph/9908427

[Bed00b] V. Bednyakov and H.V. Klapdor-Kleingrothaus, to be published

[Bel89] P.Belli et. al., Il Nuovo Cimento A **101**(1989)959

[Bel00] P. Belli, talk presented at DARK2000, 3rd International Conference on Dark Matter in Astro- and Particle Physics 2000, Heidelberg, to be published in proceedings, eds. H.V. Klapdor-Kleingrothaus and B. Majorovits, Springer, Heidelberg

[Ben98] D. Bennett, In Proceedings of the 3rd International Symposium on Sources and Detection of Dark Matter in the Universe (DM98), Feb. 1998, ed. D. Cline and astro-ph/9808121

[Ber93] T. Bernatowicz et al., Phys. Rev. C **47**(1993)806

[Ber95] J. Bernstein, *An introduction to Cosmology*, Prentice Hall, Englwood Cliffs, 1995

[Ber96] R. Bernabei et al., Phys. Lett. B **389**(1996)757

[Ber98] R. Bernabei et al., Nucl. Phys. B (Proc. Suppl) **70**(1998)79

[Ber00a] R. Bernabei et al., Phys. Rev. D **61**(2000)023512 and hep-ph/9903501

[Ber00b] R. Bernabei et al., Phys. Lett. B **480**(2000)23

[Boc94] J. Bockholt, PhD thesis, Heidelberg, 1994

[BOR91] BOREXINO-COLLABORATION, *Proposal for a real time detector for low energy solar neutrinos*, Dept. of Physics of the University of Milano (1991)

[BOR98] Borexino collaboration, G.Alimonti et al., Astro. Part. Phys. **8**(1998)141

[Bor97] S. Borgani et al. Astro. Phys. J. Letters **482**(1997)L121

[Böh97] H. Böhringer, In In H.V. Klapdor-Kleingrothaus, Y.Ramachers, editors, Dark Matter in Astro- and Particlephysics, World Scientific Publ., Singapore, 1997

[Bur94] C.P. Burgess, J.M. Cline, Phys. Rev. D **49**(1994)5925

[Bur97] A. Burkert, Astro. Phys. J. Letters **474**(1997)L99 and astro-ph/9610192

[Bur99] A. Buras and L. Silvestrini, Nucl. Phys. B **546**(1999)299

[Bur00] S. Burles, talk presented at DARK2000, 3rd International Conference on Dark Matter in Astro- and Particle Physics 2000, Heidelberg, to be published in proceedings, eds. H.V. Klapdor-Kleingrothaus and B. Majorovits, Springer, Heidelberg

[Cal86] D.O. Caldwell et al., Phys. Rev. Lett. D **33**(1986)2737

[Car00] B. Carr, talk presented at IDM2000, the 3rd internation conference on Identification of Dark Matter, IDM 2000, September,2000, York, England

[Cau96] E. Caurier et al., Phys. Rev. Lett. **77**(1996)1954

[Ceb99] S. Cebrian et al., hep-ph/9912394

[Cem95] Cemnini et al., Nucl. Inst. and Meth. A **356**(1995)526

[Chi80] Y. Chikashige, R.N. Mohapatra, R.D. Peccei, Phys. Rev. Lett **45**(1980)1926

[Cle98] B.T. Cleveland et al., Astro. Phys. J. **496**(1998)505

[Col92] J. Collar, PhD thesis, University of South Carolina, 1992

[CUP00] Homepage of the CUPP: http://cupp.oulu.fi/

[Cyb89] G. Cybenko, *Mathematics of Control*, Signals and Systems, 1989, 2(4), 303-314

[Dan99] F.A. Danevich et al., Nucl. Phys. B (Proc. Suppl.) **70**(1999)246

[Dec99] Y. Declais, private communication, 1999

[deM92] C. de Marzo (MACRO collaboration), Nucl. Inst. and Meth. A **314**(1992)380

[DeS97] A. De Silva et al., Phys. Rev. C **56**(1997)2451

[Die99] A. Dietz, diploma thesis, University of Heidelberg, 1999, unpublished

[Die00] A. Dietz, L. Baudis, G. Heusser, H.V. Klapdor-Kleingrothaus, S. Kolb, B. Majorovits, H. Päs, H. Strecker, V. Alexeev, A. Balysh, A. Bakalyarov, V.I. Lebedev, S. Zhukov, talk presented at DARK2000, 3rd International Conference on Dark Matter in Astro- and Particle Physics 2000, Heidelberg, to be published in proceedings, eds. H.V. Klapdor-Kleingrothaus and B. Majorovits, Springer, Heidelberg

[Eds00] J. Edsjo, talk presented at IDM2000, the 3rd internation conference on Identification of Dark Matter, IDM 2000, September,2000, York, England

[Eji95] H. Ejiri et al., J. Phys. Soc. Japan, **64**(1995)339

[Eji96] H. Ejiri et al., Nucl. Phys. A **611**(1996)85

[Eji99] H. Eijiri et al., nucl-ex/9911008

[Ell92] S.R. Elliott et al., Phys. Rev. C **46**, 1535 (1992).

[Ell00] J. Ellis, A. Ferst. K.A. Olive, hep-ph/0007113

[Eng88] J. Engel et al., Phys. Rev. C **37**(1988)731

[Fio98] E. Fiorini et al., Phys. Rep **307**(1998)309

[Fir96] R. Firestone et al., *Table of Isotopes*, Eighth edition, J. Wiley & Sons, Inc., 1996

[Fre70] K.C. Freeman, AP. **161**(1970)802

[Fre88] K. Freese, J. Frieman und A. Gould, Phys. Rev. D **37**(1988)3388

[Fre98] S. Fredriksson , In H.V. Klapdor-Kleingrothaus, L. Baudis, editors, DARK98, 2nd Conference on dark matter in astro- and particle physics 1998, IoP, Bristol, 1998

[Fuc00] B. Fuchs, talk presented at DARK2000, 3rd International Conference on Dark Matter in Astro- and Particle Physics 2000, Heidelberg, to be published in proceedings, eds. H.V. Klapdor-Kleingrothaus and B. Majorovits, Springer, Heidelberg

[Fuk98] Y. Fukuda et al., The SuperKamiokande Collaboration, Phys. Rev. Lett. **81**(1998)1562 and Preprint hep-ex/9807003

[Gai00] R. Gaitskell, talk presented at IDM2000, the 3rd internation conference on Identification of Dark Matter, IDM 2000, September,2000, York, England

[Gar98] P.M. Garnavich et al., Astrophys. J **509**(1998)74 and astro-ph/9806396

[Gat95] E.I. Gates, G. Gyuk, M. Turner, Astro. Phys. J. Lett. **449**(1995)L123

[GCAL95] *The GEANT-GCALOR interface users's guide*, C. Zeitnitz, T.A. Gabriel, http://www-risc.ornl.gov/codes/ccc/ccc6/ccc-610.html

[GEANT] *GEANT3.21 Detector Description and Simulation Tool*, Manual, CERN Program Library Long Writeup W5013

[Ger00] G. Gerbier talk presented at DARK2000, 3rd International Conference on Dark Matter in Astro- and Particle Physics 2000, Heidelberg, to be published in proceedings, eds. H.V. Klapdor-Kleingrothaus and B. Majorovits, Springer, Heidelberg

[GNO00] GNO collaboration, Phys. Lett. B. **490**(2000)16

[Goe35] M.Goeppert-Mayer, Phys. Rev. **48**(1935)512

[Gon96] P.Gondolo, hep-ph/9605290

[Gon99] M.C. Gonzalez-Garcia, P.C. de Holanda, C. Pena-Garay, J.W.F. Valle, hep-ph/9906469

[Gra00] D. Graff, talk presented at DARK2000, 3rd International Conference on Dark Matter in Astro- and Particle Physics 2000, Heidelberg, to be published in proceedings, eds. H.V. Klapdor-Kleingrothaus and B. Majorovits, Springer, Heidelberg

[Gue97] M. Guenther et al., Phys. Rev. D **55**(1997)54

[Gun99] Ch. Gund, private communication, Heidelberg, 1999

[Ham99] W. Hampel et al., Phys. Lett. B **447**(1999)127

[Han00] S. Hananyet al., astro-ph/0005123, in press at Astro. Phys. J. Letters

[Haw00] M. Hawkins, talk presented at DARK2000, 3rd International Confer-
ence on Dark Matter in Astro- and Particle Physics 2000, Heidelberg, to
be published in proceedings, eds. H.V. Klapdor-Kleingrothaus and B. Ma-
jorovits, Springer, Heidelberg

[Hei95] Heidelberg–Moscow Collaboration, A. Balysh, M. Beck, S.T. Belyaev,
J. Bockholt, A. Demehin, A. Gurov, J. Hellmig, G. Heusser, M. Hirsch M,
C. Hoffmann, H.V. Klapdor-Kleingrothaus, I. Kondratenko, D. Kotelnikov,
V.I. Lebedev, B. Maier, A. Mueller, H. Päs, F. Petry, E. Scheer, H. Strecker,
M. Voellinger, Phys. Lett. B356 (1995) 450

[Hei97] Heidelberg–Moscow Collaboration, L. Baudis, M. Guenther, J. Hellmig,
G. Heusser, M. Hirsch, H.V. Klapdor-Kleingrothaus, S Kolb, H. Päs,
Y. Ramachers, H. Strecker, M. Voellinger, A. Bakalyarov, A. Balysh,
S.T. Belyaev, V.I. Lebedev, S. Zhoukov, Physics Letters B **407**(1997)219-
224

[Hei98] Heidelberg-Moscow collaboration, L. Baudis, J. Hellmig, G. Heusser,
H.V. Klapdor-Kleingrothaus, S Kolb, B. Majorovits, H. Päs, Y. Ramach-
ers, H. Strecker, V. Alexeev, A. Bakalyarov, A. Balysh, S.T. Belyaev,
V.I. Lebedev, S. Zhoukov, Phys. Rev. D **59**(1999)022001 and Preprint hep-
ex/9811045

[Hei99] Heidelberg-Moscow Collaboration., L. Baudis, A. Dietz, G. Heusser,
H.V. Klapdor-Kleingrothaus, S Kolb, I. Krivosheina, B. Majorovits,
V.F. Melnikov, H. Päs, F. Schwamm, H. Strecker, V. Alexeev,
A. Bakalyarov, A. Balysh, S.T. Belyaev, V.I. Lebedev, S. Zhoukov, Phys.
Rev. Lett **83**(1999)41

[Hel96] J. Hellmig, PhD thesis, Univerity of Heidelberg, 1996

[Hel00] J. Hellmig, H.V. Klapdor-Kleingrothaus, in press at Nucl. Inst. Meth.
A

[Hel97] J. Hellmig and H.V. Klapdor-Kleingrothaus, Z.Phys. A **359**(1997)361

[Hes59] W.N. Hess, H.W. Patterson and R. Wallace, Phys. Rev. **116**(1959)449

[Heu95] G. Heusser, Ann. Rev. Nucl. Part. Sci. **45**(1995)543

[Heu00] G. Heusser et al., Applied Radiation and Isotopes, **52**(2000)691

[Hir95] M. Hirsch, H.V. Klapdor-Kleingrothaus, S.G. Kovalenko, Phys. Rev.
Lett. **75**(1995)17

[Hir96] M. Hirsch, H.V. Klapdor-Kleingrothaus, S.G. Kovalenko, H. Päs, Phys.
Lett. B **372**(1996)8

[Hor89] K. Hornik, M. Stinchcombe, H. White,*Neural Networks*, 1989, 2(5),359-
366

[Hu98] W. Hu, Astro. Phys. J. **506**(1998)485

[Hyk91] J. G. Hykawy et al., Phys. Rev. Lett. **67**(1991)1708

[Jed00] K. Jedamzik,talk presented at DARK2000, 3rd International Confer-
ence on Dark Matter in Astro- and Particle Physics 2000, Heidelberg, to
be published in proceedings, eds. H.V. Klapdor-Kleingrothaus and B. Ma-
jorovits, Springer, Heidelberg

[Jen98] A. Jenkins et al., Astro. Phys. J. **499**(1998)20

[Jun96] G. Jungmann, M. Kamionkowski, K. Griest, Phys. Rep. **267**(1996)195

[Kap22] J. C. Kapteyn, Astro. Phys. J. **55**(1922)302

[Kai00] N. Kaiser, talk presented at IDM2000, the 3rd internation conference on
Identification of Dark Matter, IDM 2000, September,2000, York, England

[Kay89] B. Kayser, *The physics of massive neutrinos*, World Scientific, Singa-
pore, 1989

[Kaw93] A. Kawashima, K. Takahashi, A. Masuda, Phys. Rev. C **47**(1993)2452

[Ke91] Y. Ke et al., Phys. Lett. B **265**(1991)53

[Kla86] H.V. Klapdor-Kleingrothaus, K. Grotz, Astrophys. J. **304**(1986)L39

[Kla87] H.V. Klapdor-Kleingrothaus, Proposal, Internal Report, MPI-H ,1987

[Kla95] H.V. Klapdor-Kleingrothaus, A. Staudt, *Teilchenphysik ohne Beschle-
uniger*, Teubner Studienbücher, Stuttgart 1995

[Kla97] H.V. Klapdor-Kleingrothaus, In proceedings of NEUTRINO'96,
Helsinki, June 1996, World Scientific, Singapore, 1997

[Kla98a] H.V. Klapdor-Kleingrothaus in Proceedings of the First International
Conference on Particle Physics Beyond the Standard Model, Castle Ring-
berg, Germany, 8-14 June 1997, edited by H.V. Klapdor-Kleingrothaus and
H.Päs, IOP Bristol, 1998

[Kla98b] H.V. Klapdor-Kleingrothaus, J. Hellmig und M. Hirsch, J. Phys. G
24(1998)483

[Kla98d] H.V. Klapdor-Kleingrothaus, Y. Ramachers, Euro. Phys. J. A
3(1998)85

[Kla99a] H.V. Klapdor-Kleingrothaus, L. Baudis, G. Heusser, B. Majorovits,
H. Päs, Proposal, MPI-H-V26-1999, August 1999, hep-ph/9910205

[Kla99b] H.V. Klapdor-Kleingrothaus, K. Zuber, *Particle astrophysics*, Institue
of Physics Publ., Bristol, 1997 , rev. edition 1999

[Kla99c] H.V. Klapdor-Kleingrothaus, H. Päs, U. Sarkar, Euro. Phys. J. A
5(1999)3, hep-ph/9809396

[Kla00a] H.V. Klapdor-Kleingrothaus, L. Baudis, A. Dietz, G. Heusser, B. Ma-
jorovits , Proposal, MPI-H-V2-2000, February 2000

[Kla00b] H.V. Klapdor-Kleingrothaus, in Springer Tracts in Modern Physics **163**(2000)69-104, Springer

[Kla00c] H.V. Klapdor-Kleingrothaus, H. Päs, Y.A. Smirnov, hep-ph/0003219

[Kla00d] H.V. Klapdor-Kleingrothaus, L. Baudis, A. Dietz, G. Heusser, I. Krivosheina, B. Majorovits, H. Strecker , H. Tu, et al., Internal Report, Proposal

[Kla00e] H.V. Klapdor-Kleingrothaus, *60 Years of Double Beta Decay - From Nuclear Physics to Beyond Standard Model Physics*, World Scientific, Singapore, 2000

[Kno89] G.F. Knoll,*Radiation Detection and Measurement*, Wiley, 2nd Edition, 1989

[Kol90] E. Kolb, M. Turner, *the early universe*, Addison Wesley, Redwood City, 1990

[Krö96] B. Kröse and P. van der Smagt, University of Amsterdam, *An Introduction to Neural Networks*, 1996, from http://www.robotic.dlr.de/Smagt/books/

[Kud98] N. Kudomi et al., Nucl. Phys. A **629**(1998)527c

[Lan00] A.E. Lange et al., astro-ph/0005004, submitted to Phys. Rev. D

[Lal67] D. Lal, B. Peter, *Cosmic Ray Produced Radioactivity on the Earth*, Springer, Berlin-Heidelberg, 1967

[Lau99] M. Laubenstein, private communication, 1999

[Las00] T. Lasserre, talk presented at DARK2000, 3rd International Conference on Dark Matter in Astro- and Particle Physics 2000, Heidelberg, to be published in proceedings, eds. H.V. Klapdor-Kleingrothaus and B. Majorovits, Springer, Heidelberg

[Leh00] M. Lehner, talk presented at DARK2000, 3rd International Conference on Dark Matter in Astro- and Particle Physics 2000, Heidelberg, to be published in proceedings, eds. H.V. Klapdor-Kleingrothaus and B. Majorovits, Springer, Heidelberg

[Lew70] V.E. Lewis Nucl. Phys. A **151**(1970)120

[Lew96] J.D. Lewin, P.F. Smith, Astropart. Phys. **6**(1996)87

[Loe99] M. Loewenstein and R.E. White, Astro. Phys. J. **511**(1999)50

[Lue98] R. Luescher et al., Nucl. Phys. B (Proc. Suppl.) **66**(1998)195

[Mai95] B. Maier, PhD thesis, University of Heidelberg, 1995

[Maj98] B. Majorovits, diploma thesis, University of Heidelberg, 1998, unpublished

[Maj99] B. Majorovits and H.V. Klapdor-Kleingrothaus, Euro. Phys. Journal A **6**(1999)4,463

[Maj00a] B. Majorovits, L. Baudis, G. Heusser, H. Strecker, H.V. Klapdor-Kleingrothaus, Nucl. Inst. and Meth. A **455**(2000)369

[Maj00b] B. Majorovits, talk presented at 4th International Symposium on Sources and Detection of Dark Matter in the Universe (DM 2000), Marina del Ray, California, 20-23 February 2000, to be published in Proceedings, eds. D. Cline and J. George, Springer, Heidelberg

[Maj00c] B. Majorovits, talk presented at DARK2000, 3rd International Conference on Dark Matter in Astro- and Particle Physics 2000, Heidelberg, to be published in proceedings, eds. H.V. Klapdor-Kleingrothaus and B. Majorovits, Springer, Heidelberg

[Maj00d] B. Majorovits, talk presented at IDM2000, the 3rd internation conference on Identification of Dark Matter, IDM 2000, September,2000, York, England

[Man00] V. Mandic, et al., hep-ph/0008022

[MLa88] V. McLane, C.L. Dunford and P.F. Rose, *Neutron cross sections*, Volume 2, Academic Press Inc., 1988

[Mil98] M. Milgrom, In H.V. Klapdor-Kleingrothaus, L. Baudis, editors, DARK98, 2nd Conference on dark matter in astro- and particle physics 1998, IoP, Bristol, 1998

[Min00] H. Minakata and H. Nunokawa, hep-ph/0010240

[Muk76] T. Mukoyama, Nucl. Inst. Meth. **134**(1976)125

[Mut89] K. Muto, H.V. Klapdor-Kleingrothausund E. Bender, Z. Phys. A **334**(1989)187

[Nat94] P. Nath, R. Arnowitt, Phys.Rev.Lett. 74(1995)4592

[Nat97] P. Nath, R. Arnowitt, hep-ph/9710477

[Nat98] P. Nath, R. Arnowitt, hep-ph/9801454

[Nat00] P. Nath, talk presented at IDM2000, the 3rd internation conference on Identification of Dark Matter, IDM 2000, September,2000, York, England

[Päs99a] H. Päs, PhD thesis, University of Heidelberg, 1999

[Päs99b] H. Päs, M. Hirsch, H.V. Klapdor-Kleingrothaus, Phys. Lett. B **459**(1999)450

[Pac86] B. Paczinsky, Astro. Phys. J. **304**(1986)1

[Pan99] O. Panella et al., hep-ph/9903253v2

[Pen65] A. Penzias, R. Wilson, Astro. Phys. J. **142**(1965)L419

[Pec89] R.D. Peccei in *CP violation*, editor C. Jarlskog, Woeld Scentific Publ., 1989, pp. 503-551

[PDG96] Partile Data Group (PDG 96), R.M. Barnett et al., Phys. Rev. D **54**(1996)1

[Per95] M. Persic, P. Salucci, Rotation curves of 967 galaxies, Ap. J. Suppl. **99**(1995)501

[Per98] S. Perlmutter et. al, Astro. Phys. J. **483** (1997)565 and astro-ph/9812133

[Pet95] F. Petry, PhD thesis, University of Heidelberg, 1995

[Pfe97] D. Pfenniger, In H.V. Klapdor-Kleingrothaus, Y.Ramachers, editors, Dark Matter in Astro- and Particlephysics, World Scientific Publ., Singapore, 1997

[Pon98] O.A. Ponkratenko, V.I. Tretyak, Y.G. Zdesenko, In H.V. Klapdor-Kleingrothaus, L. Baudis, editors, DARK98, 2nd Conference on dark matter in astro- and particle physics 1998, IoP, Bristol, 1998

[Pri00] J. Primack, talk presented at 4th International Symposium on Sources and Detection of Dark Matter in the Universe (DM 2000), Marina del Ray, California, 20-23 February 2000, to be published in Proceedings, eds. D. Cline and J. George, Springer, Heidelberg and astro-ph/0007187

[Ram98a] Y.A. Ramachers, PhD thesis, University of Heidelberg, 1998

[Ram98b] Y. Ramachers, M. Hirsch, H.V. Klapdor-Kleingrothaus, E. Phys. J A **1**(1998)93

[Reu91] D. Reusser et al., Phys. Lett. B **255**(1991)143

[Rob35] H.P. Robertson, Ap. J. **82**(1935)248

[Rot84] J. Roth et al., IEEE Trans. Nucl. Sci., NS-31(1984)367

[San00] P. Sangsingkeow, Perkin Elmer (formerly EG&G Ortec), private communication, 2000

[Sch99] F. Schwamm, diploma thesis, University of Heidelberg, 1999, unpublished

[Sch00] R. Schnee, talk presented at DARK2000, 3rd International Conference on Dark Matter in Astro- and Particle Physics 2000, Heidelberg, to be published in proceedings, eds. H.V. Klapdor-Kleingrothaus and B. Majorovits, Springer, Heidelberg

[Sei00] W. Seidel, talk presented at DARK2000, 3rd International Conference on Dark Matter in Astro- and Particle Physics 2000, Heidelberg, to be published in proceedings, eds. H.V. Klapdor-Kleingrothaus and B. Majorovits, Springer, Heidelberg

[Sik97] P. Sikivie, In H.V. Klapdor-Kleingrothaus, Y.Ramachers, editors, Dark Matter in Astro- and Particlephysics, World Scientific Publ., Singapore, 1997

[Sim97] F. Simkovic et al., Phys. Lett. B **393**, 267-273 (1997)

[SNO97] SNO collaboration, Proceedings of the 4th International Solar Neutrino Conference, Heidelberg, 8-11 April 1997, editor W. Hampel, 1997, p210

[Sob00] H. Sobel, talk presented at Neutrino 2000, XIX International Conference on Neutrino Physics and Astrophysics, Sudbury, Canada, June 16-21, 2000

[Sta90] A. Staudt, K. Muot, H.V. Klapdor-Kleingrothaus, Europhys. Lett. **13**(1990)31

[Suz00] Y. Suzuki, talk presented at Neutrino 2000, XIX International Conference on Neutrino Physics and Astrophysics, Sudbury, Canada, June 16-21, 2000

[Teg00] M. Tegmark, M. Zaldarriaga and A. Hamilton, hep-ph/0008167v2

[Tom91] T. Tomoda, Rep. Prog. Phys. **54**, 53 (1991).

[Too65] A. Toomre, Astro. Phys. J. **139**(1964)1217

[Tov00] D. Tovey et al., Phys. Lett B **488**(2000)17 and hep-ph/0005041

[Tur93] M.S. Turner, astro-ph/9310019

[Tur00] M.S. Turner, Physica Scripta **T85**(2000)210 and astro-ph/9901109

[Tys95] J.A. Tyson und P. Fischer, Measurement of the mass profile of ABELL 1689, Ap. J. Lett. **446**(1995)L55

[Ure97] J.L. Uretsky, Nucl. Inst. and Meth. A **399**(1997)285

[vHen99] R. von Hentig, private communication, 1999

[Wal36] A.G. Walker, Proc. Lond. Math. Soc. **42**(1936)90

[Wei35] C.F. von Weizsäcker, Z. Phys. **96**(1935)431

[WIP00] Homepage of the WIPP: http://www.wipp.carlsbad.nm.us/leptontown, 2000

[Wu91] X.R. Wu, A.Staudt, H.V. Klapdor-Kleingrothaus, C. Ching und T. Ho, Phys. Lett. B **272**(1991)169

[Zak00] A. Zakharov, talk presented at DARK2000, 3rd International Conference on Dark Matter in Astro- and Particle Physics 2000, Heidelberg, to be published in proceedings, eds. H.V. Klapdor-Kleingrothaus and B. Majorovits, Springer, Heidelberg

[Zwi33] F. Zwicky, Helv. Phys. Acta **6**(1933)110

Danksagung

An dieser Stelle möchte ich all jenen danken, die zur Enstehung dieser Arbeit beigetragen haben:

Herrn Prof. Dr. H.V. Klapdor-Kleingrothaus für die interessante Themenstellung dieser Arbeit, die sehr gute Betreuung und die exzellente Förderung.

Dem Direktorium des Max-Planck-Instituts für Kernphysik, insbesondere Herrn Prof. Dr. D. Schwalm für die erstklassigen Arbeitsbedingungen.

Herrn Prof. Dr. D. Schwalm für das Interesse an dieser Arbeit und die Übernahme der Zweitkorrektur.

Dem Graduiertenkolleg für experimentelle Methoden in der Kern- und Teilchenphysik für die finanzielle Unterstüzung.

Herrn H. Strecker für die sehr gute Zusammenarbeit und die unverzichtbare Hilfe bezüglich technischer Angelegenheiten.

Herrn Dr. G. Heusser für zahlreiche nützliche Hinweise und Informationen.

Frau Dr. L. Baudis und Herrn Dipl. Phys. A. Dietz für die gute Zusammenarbeit.

Den Herren Dr. H. Päs und Dr. St. Kolb für zahlreiche hilfreiche Diskussionen, Debatten und Aufmunterungen.

Herrn Dr. Y. Ramachers für viele anregende Diskussionen.

Den aktuellen und ehemaligen Gruppenmitgliedern der Arbeitsgruppe von Prof. Dr. H.V. Klapdor-Kleingrothaus , Frau Dr. L. Baudis, Herrn Dipl. Phys. A. Dietz, Herrn Dr. St. Kolb, Herrn Dr. J. Nabi, Herrn Dr. H. Päs, Herrn Dipl. Phys. F. Schwamm, Frau H. Tu für das angenehme Arbeitsklima.

Herrn Dr. A. Bakalyarov für anregende Diskussionen.

Herrn H. Zapf für die Hilfe beim Aufbau des HDMS Experiments im Gran Sasso.

Den Herren Dr. S. Zhukov und Dipl. Phys V. Alexeev für die gute Zusammenarbeit am Gran Sasso Untergrunlabor.

Den Kollegen und Freunden am Laboratori Nazionali del Gran Sasso für das angenehme Arbeitsklima und viele Hilfestellungen bezüglich Angelegenheiten des täglichen Lebens, insbesondere den Herren Dr. M. Junker, Dr. Gy. Korga, Dr. L. Papp und Dr. Y. Ramachers.

Den Herren Dr. H. Päs und Dipl. Phys. E. Majorovits für die kritische Durchsicht des Manuskripts.

Meiner Familie, sowie Helena für die moralische Unterstützung.